DESIGN OF AN ISOLATED BIDIRECTIONAL RESONANT DC-DC CONVERTER WITH WIDE INPUT VOLTAGE RANGE FOR MEDIUM POWER APPLICATIONS

ASIF MUSTAFA

FACULTY OF ENGINEERING
UNIVERSITY OF MALAYA
KUALA LUMPUR

2021

DESIGN OF AN ISOLATED BIDIRECTIONAL RESONANT DC-DC CONVERTER WITH WIDE INPUT VOLTAGE RANGE FOR MEDIUM POWER APPLICATIONS

ASIF MUSTAFA

THESIS SUBMITTED IN PARTIAL FULFILMENT OF THE REQUIREMENTS FOR THE DEGREE OF MASTER OF ENGINEERING SCIENCE

FACULTY OF ENGINEERING
UNIVERSITY OF MALAYA
KUALA LUMPUR

2021

UNIVERSITY OF MALAYA

ORIGINAL LITERARY WORK DECLARATION

Name of Candidate: Asif Mustafa

Matric No: 17036359/1

Name of Degree: Master of Engineering Science

Title of Thesis:

DESIGN OF AN ISOLATED BIDIRECTIONAL RESONANT DC-DC CONVERTER WITH WIDE INPUT VOLTAGE FOR MEDIUM POWER APPLICATIONS

Field of Study: Power Electronics

I do solemnly and sincerely declare that:

(1) I am the sole author/writer of this Work;
(2) This Work is original;
(3) Any use of any work in which copyright exists was done by way of fair dealing and for permitted purposes, and any excerpt or extract from, or reference to or reproduction of any copyright work has been disclosed expressly and sufficiently, and the title of the Work and its authorship have been acknowledged in this Work;
(4) I do not have any actual knowledge nor do I ought reasonably to know that the making of this Work constitutes an infringement of any copyright work;
(5) I hereby assign all and every right in the copyright to this Work to the University of Malaya (UM), who henceforth shall be the owner of the copyright in this Work and that any reproduction or use in any form or by any means whatsoever is prohibited without the written consent of UM having been first had and obtained;
(6) I am fully aware that if, in the course of making this Work, I have infringed any copyright, whether intentionally or otherwise, I may be subject to legal action or any other action as may be determined by UM.

Asif

Candidate's Signature Date: 12 April, 2021

Subscribed and solemnly declared before,

Witness's Signature Date:

Name:

Designation

ABSTRACT

Isolated Bidirectional DC-DC converters (IBDCs) are mainly used to provide reliable and good quality power in various electrical applications such as uninterrupted power supply (UPS), DC micro-grid with energy storage systems (ESSs), electric vehicles, vehicle-to-grid (V2G), grid-to-vehicle (G2V) and many more. Among several IBDCs, the single-phase resonant converter is mostly preferred owing to its minimized switching losses, high reliability, high power density, reduced electromagnetic interference, and ability to operate at high frequency. Nevertheless, it has the limitations of circulating power flow and limited soft-switching range for wide input voltage and load range variations. This research provides a novel topology for dual-phase LLC resonant converter with an improved variable frequency based zero circulating current phase shift modulation (VFPSM-ZCC). The topology is based on H6 inverter topology able to generate two square voltage waveforms and provide a dual-phase for two symmetrical resonant tanks and its high-frequency transformers, which are connected in series. The arrangement leads to a reduction of voltage stress across upper and lower switches to half of the input voltage that can be useful at high voltage input conditions. On the secondary side of the high-frequency transformer, an identical six-switch arrangement as an active rectifier is employed that becomes the critical component in energy storage systems (i.e., batteries, super-capacitors) for the purpose of bidirectional power flow. The converter is capable of achieving ZVS for primary as well as secondary switches for a wide variation of input voltage and output load. The proposed modulation scheme is a 3-variable control that enables the converter to operate with increased voltage gain range under all input voltage and loading conditions. Variable frequency control leads to the soft-switching operation of the switches connected to the primary side for all load ranges. The phase shift control is used as power transfer control along with maintaining a constant output voltage under changing input voltage. Moreover, the duty cycle calculation based on load

conditions helps in eliminating the reverse power flow (RPF) due to circulating current, especially under light-load conditions, thereby increasing the conversion efficiency in comparison to the conventional dual active bridge converter. The inherent ability of frequency selection based on the loading conditions also minimizes the RMS resonant current that reduces the conduction losses while operation, especially under light-load conditions. To verify the performance of the proposed converter and employed modulation scheme, a 1.5kW prototype with 210V-400V input and 80V output is built, and the experimental results have been presented. The measured efficiency of the built PCB prototype of the converter at full load is 96.7% and 94.2% under maximum and minimum input voltage conditions, respectively.

ABSTRAK

Penukar DC-DC dwiarah berasingan (IBDCs) digunakan terutamanya untuk menyediakan kuasa yang boleh dipercayai dan berkualiti tinggi dalam pelbagai aplikasi elektrik seperti bekalan kuasa tanpa gangguan (UPS), grid mikro DC dengan sistem penyimpanan tenaga (ESSs), kenderaan elektrik, kenderaan-ke-grid (V2G), grid-ke-kenderaan (G2V) dan sebagainya. Di antara beberapa IBDC, penukar resonans fasa tunggal biasanya lebih dipilih untuk meminimumkan kerugian penukaran, kebolehpercayaan yang tinggi, ketumpatan kuasa yang tinggi, gangguan elektromagnetik yang berkurang dan keupayaan untuk beroperasi pada frekuensi tinggi. Walau bagaimanapun, ia mempunyai batasan aliran kuasa yang beredar dan rangkaian penukaran lembut yang terhad untuk voltan masukan yang luas dan variasi pelbagai beban. Penyelidikan ini menyediakan topologi untuk dual fasa penukar resonan LLC dengan frekuensi pembolehubah yang lebih baik berdasarkan sifar aliran modulasi peralihan fasa semasa (VFPSM-ZCC). Topologi ini berdasarkan pada topologi inverter H6 yang dapat menghasilkan output ganda dan menyediakan dua fasa untuk dua tangki salun simetri dan transformer frekuensi tinggi, yang disambungkan secara siri. Susunan ini membawa kepada pengurangan tekanan voltan merentas suis atas dan bawah hingga separuh daripada voltan masukan yang boleh berguna pada keadaan input voltan tinggi. Di sisi kedua pengubah frekuensi tinggi, susunan enam suis yang sama sebagai penerus aktif digunakan sebagai komponen utama dalam sistem penyimpanan tenaga (iaitu bateri, kapasitor super) untuk tujuan aliran kuasa dwiarah. Penukar mampu mencapai ZVS untuk suis utama dan sekunder untuk variasi voltan masukan dan beban output. Skema modulasi yang dicadangkan adalah kawalan 3-ubah yang membolehkan penukar untuk beroperasi dengan peningkatan voltan dalam keadaan semua voltan masukan dan semua keadaan pemuatan. Kawalan kekerapan berubah-ubah membawa kepada operasi penukaran lembut suis yang disambungkan ke bahagian utama untuk semua julat beban. Kawalan

peralihan fasa digunakan sebagai kawalan pemindahan kuasa bersama-sama dengan mengekalkan voltan keluaran tetap dalam menukar voltan masukan. Selain itu, pengiraan kitaran duti berdasarkan keadaan beban membantu dalam menghapuskan aliran kuasa terbalik (RPF) yang disebabkan oleh arus yang beredar terutamanya di bawah keadaan beban ringan, dengan itu, meningkatkan kecekapan penukaran berbanding dengan konvensional penukar jambatan aktif dua. Keupayaan pemilihan kekerapan yang wujud berdasarkan syarat pemuatan juga meminimumkan aliran resonan RMS yang mengurangkan kerugian pengaliran semasa operasi terutama di bawah keadaan beban ringan. Untuk mengesahkan prestasi penukar yang dicadangkan dan skema modulasi yang digunakan, prototaip 1.5kW dengan input 210V-400V dan output 80V dibina dan keputusan eksperimen telah dibentangkan. Kecekapan diukur prototaip PCB terbina pada penukar pada beban penuh adalah 96.7% dan 94.2% di bawah syarat voltan masukan maksimum dan minimum.

ACKNOWLEDGEMENT

First, I am thankful to Almighty Allah for giving me the strength, knowledge, ability, and opportunity to complete this challenging task.

I would like to express my deep gratitude to Prof (Dr.) Saad Mekhilef. His great help made my study at University of Malaya possible. He has given me invaluable guidance, inspiration, and suggestions in my quest for knowledge. Without his able supervision, this thesis would not have been possible, and I am eternally grateful to him for his assistance.

I would like to express my great appreciation to Marif Daula Siddiqui, who guided me on this journey as my elder brother and fellow researcher. The numerous in-depth technical discussions resulted in a better researcher in me. I would also like to thank my fellow members from PEARL Lab and friends, especially Prashant Shrivastava, Naveed Akhtar, Tuanku Badzlin, Dr. Nasseur, and Immad Shams, for their assistance and support throughout my candidature.

My deepest gratitude belongs to my parents and family for their prayers, love, sacrifice, and unconditional support for my study.

TABLE OF CONTENTS

LIST OF FIGURES

LIST OF TABLES

LIST OF SYMBOLS AND ABBREVIATIONS

V_{in}	:	Input Voltage
C_r	:	Resonant Capacitor
L_r	:	Resonant Inductor
L_m	:	Magnetizing Inductance
k	:	Series-Parallel Inductance Ratio
R_o	:	Load Resistance
Q	:	Quality Factor
C_o	:	Filter Capacitor
f_r	:	Series Resonant Frequency
f_s	:	Switching Frequency
f_o	:	Open Circuit Resonant Frequency
R_{ds}	:	MOSFET Drain to Source Resistance
n	:	Transformer Turns Ratio
I_s	:	Resonant Current
I_{oh}	:	Transformer Current
V_{cr}	:	Resonance Capacitor Voltage
I_{Lm}	:	Magnetizing Current
V_{oh}	:	Transformer Voltage
I_o	:	Output Current
I_{in}	:	Input Current
P_{in}	:	Input Power
P_o	:	Output Power
F	:	Normalized Switching Frequency
ϕ	:	Controlled Phase-Shift
M	:	Converter Gain

α	:	Input Impedance Angle
β	:	Lagging Phase Angle
R_{AC}	:	Equivalent AC Resistance
HB	:	Half Bridge
FB	:	Full Bridge
BDC	:	Bi-directional Converter
DAB	:	Dual Active Bridge
RC	:	Resonant Converter
SRC	:	Series Resonant Converter
PRC	:	Parallel Resonant Converter
SPRC	:	Series-Parallel Resonant Converter
PWM	:	Pulse Width Modulation
PFM	:	Pulse Frequency Modulation
SPM	:	Single Phase-shift Modulation
DPS	:	Dual Phase Shift
EPS	:	Extended Phase Shift
TPS	:	Triple Phase Shift
ZCC	:	Zero Circulating Current
EMI	:	Electromagnetic Interference
ZVS	:	Zero Voltage Switching
ZCS	:	Zero Current Switching
ZVZCS	:	Zero Voltage Zero Current Switching
RMS	:	Root of Mean Square
BDCs	:	Bi-directional DC/DC converters
ESR	:	Equivalent Series Resistance

CHAPTER 1: INTRODUCTION

1.1 Background

The industrial progress, expanded transportation network, and current lifestyle of humankind flourish on the electricity consumption, thereby defining it as a specific commodity for humanity. A significant percentage of total electricity demands are fulfilled by conventional fossil fuel-based electricity generation systems that are incessantly exhausting. The widespread utilization of traditional energy sources has led to an ever-increasing carbon emission, which is responsible for environmental degradation and climate change (Wilson & Burgh, 2007). The global leaderships have taken initiatives like the Kyoto Protocol, Energy Strategy for Europe to reduce their carbon footprints (Sands, 1992). Besides, more than 196 countries signed and pledged the Paris Accord under the initiative United Nations Framework Convention for Climate Change (UNFCCC) to confront the concern of greenhouse gas emissions (Harrould-Kolieb, 2019). Such initiatives imply an alteration of the electricity generation system from conventional to renewable and sustainable energy-based electricity generation systems (Bose, 2013). With an increased concern of global warming and possible energy crisis, the vast availability of solar, wind, and tidal energy drive the concept of such hybrid electricity generation systems. The solar PV based electricity generation systems have been on the rise, with their installed capacity increasing yearly. As per the Renewables, Global Status Report, 2020 REN21, the installed PV capacity had risen slightly in 2019; however, it surpassed the 100 GW level. Figure 1.1 depicts the annual increase in Solar PV Global Capacity. The renewable energy sources are combined in a DC micro-grid for distributed generations. However, the intermittent nature of energy from these sources results in a wide variation of power generation (Huang et al., 2011; Kakigano et al., 2007). To mitigate such variations and have constant and stabilized power output, energy storage systems (ESSs) are employed (Guarnieri et al., 2010).

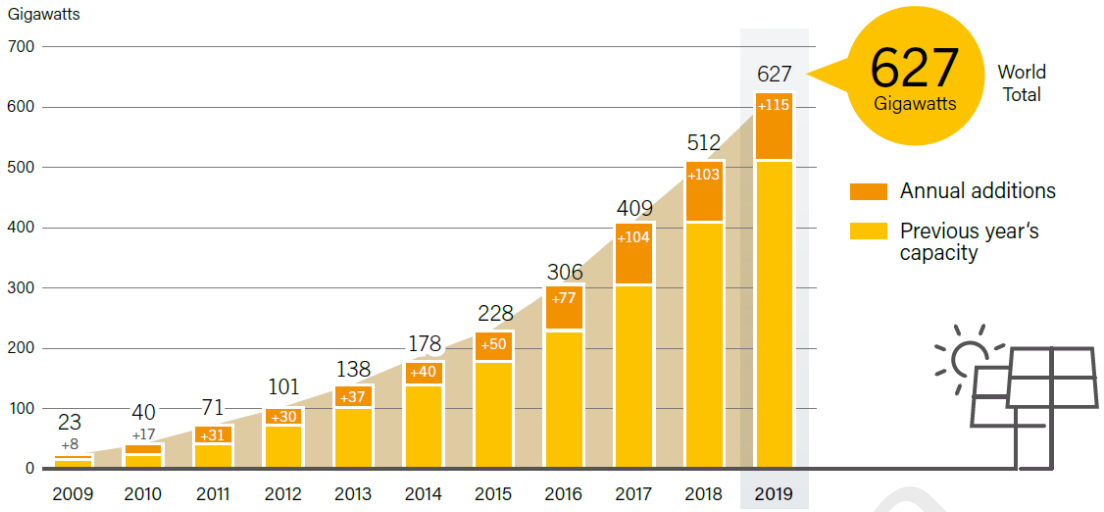

Figure 1.1 Solar PV Global Capacity and Annual Additions, 2009-2019 (Renewables, Global Status Report, 2020 REN21)

Electric Vehicles (EVs) can be incorporated along with the renewable energy sources into the grid for the Vehicle-to-Grid (V2G) system (Fang et al., 2012; Hu & Liaw, 2016; Monteiro et al., 2016). The ESSs, such as supercapacitors or batteries, have a prerequisite to avoid power fluctuation and improve the system's stability (K. Jin et al., 2009). Figure 1.2 depicts a typical micro-grid representation with ESSs. The intermittent power generated from renewable energy sources is fed into a common HVDC bus through AC/DC or DC/DC converter as per the requirements. The system also comprises of Solid State Transformers (SSTs) that are used to integrate ESSs to the AC/DC bus. The power balance and the voltage regulation of the AC/DC bus are majorly done by the SSTs (C. Jin et al., 2014; Y. Li et al., 2018). It enables the power conversion through bidirectional power converters consisting of high-frequency MOSFETs and magnetic components. Moreover, SSTs can also provide dynamic reactive power compensation and harmonic control. The power converters constitute an essential component of ESSs based micro-grid. It has the capability to generate constant output with variable input. A bidirectional DC-DC converter (BDC) acts as a power bidirectionality interface for DC-bus and various electric

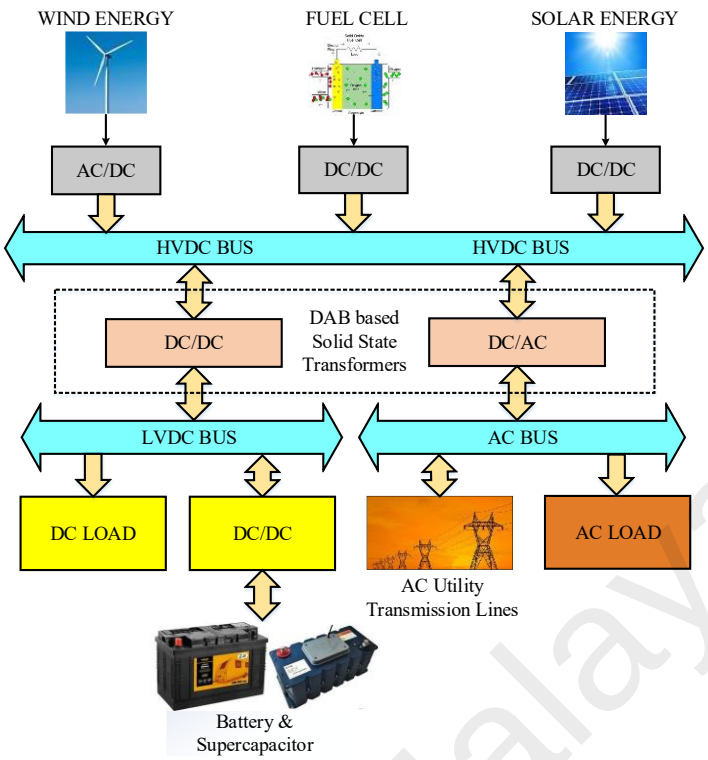

Figure 1.2 A typical micro-grid representation with Energy Storage Systems

systems such as electric vehicles (EV) or Hybrid Electric vehicles (HEV), batteries, renewable energy sources, and DC distribution networks (Madawala & Thrimawithana, 2011; J. Zhang et al., 2007; Z. Zhang et al., 2009). The current research of bidirectional power converters focuses on the optimization of various topologies employing advanced switching devices such as SiC/GaN MOSFETs as switches and improved modulation techniques.

1.2 Problem Statement

Dual active bridge (DAB) is drawing much interest as a bi-directionality interface in energy storage systems pertaining to its appealing features such as excellent power transfer capability, galvanic isolation and protection, reliability, high power density, and high-efficiency (Engel et al., 2013; Florian Krismer & Kolar, 2012; Nymand & Andersen, 2010; Sha et al., 2016; B. Zhao et al., 2015). However, this feature suffers a setback when the turn ratio of the transformer is not 1:1 (Xiao & Xie, 2008). At low-load conditions,

the converter conversion efficiency deteriorates. The massive difference between input and output voltage causes increased peak current resulting in high conduction and switching losses (Kheraluwala et al., 1992). For the sake of extended gain range and minimized reverse power flow (RPF), many control schemes have been proposed (Karthikeyan & Gupta, 2018; Shakib & Mekhilef, 2017; B. Zhao, Song, & Liu, 2013a). Nevertheless, these modulation strategies cannot eliminate all the drawbacks at once.

1.3 Objectives of Study

The overall goal of this study is to develop a novel topology of isolated bi-directional LLC resonant converter for an increased voltage gain range, ZVS range, and zero reverse power flow. The focus also lies in the efficient operation throughout the voltage gain range and light load efficiency improvement. The specific objectives of this study are as follows:

1. To propose a novel isolated bi-directional dual-phase LLC resonant DC-DC converter with a new control scheme that maintains ZVS to all switches for wide voltage gain and load conditions.
2. To implement the proposed topology and modulation scheme of the isolated bidirectional dual-phase LLC resonant DC-DC converter.
3. To evaluate the performance of the proposed converter for wide input voltage and load conditions.

1.4 Research Methodology

To realize the aforementioned objectives of this research study, a literature assessment of the research topic is performed to understand and analyze the state-of-art-works accomplished on the isolated bidirectional resonant DC-DC converter. In order to develop the proposed resonant converter, mathematical modelling and analysis are implemented to evaluate design parameters for the realization of the proposed system. Each part of the

proposed converter is evaluated using simulation software Matlab/Simulink. Likewise, the modulation schemes for the converter are realized mathematically and using simulations tools. The developed topology of the resonant converter with optimal design parameters is implemented in hardware to get the final prototype of the proposed converter. To validate the performance of the proposed converter, different tests are done, and experimental results are presented. Furthermore, the comparison of the proposed converter is performed with the other research done in the field of resonant converters. The flowchart of the research methodology is presented as follows;

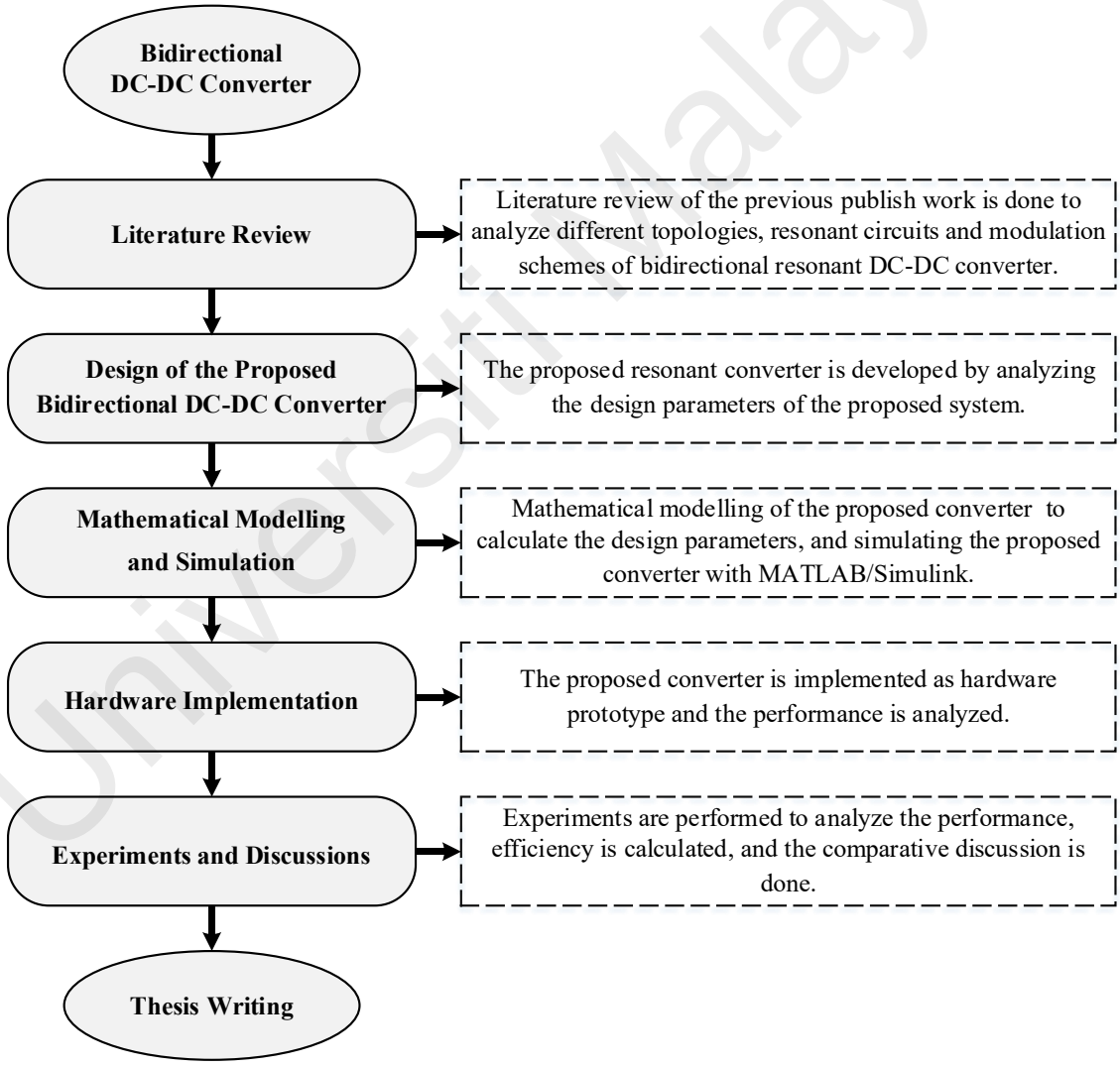

Figure 1.3 Flowchart of research methodology

1.5 Thesis Outline

This study proposes a novel topology and an improved control scheme for an isolated dual-phase bi-directional LLC resonant DC-DC converter with zero circulating current that is suitable for wide input voltage and load applications. It organized as follows:

Chapter 2 presents a detailed literature survey of the bi-directional DC-DC converters. Different resonant converters have been discussed on the basis of resonant component counts, and the DC characteristics of different resonant tanks are explained. Moreover, the modulation schemes for the BDCs that have been reported in the previous literature are presented. The thesis also discusses the various resonant converter analysis methods. Finally, a comparison of different topologies is described based on the soft-switching ranges, the circulating current suppression, and characteristics due to the variation of resonant tank parameters and modulation strategies.

Chapter 3 presents the detailed operation of the proposed topology. It represents the steady-state analysis and graphical representations of key characteristics in terms of control variables. It also discusses the voltage and current stresses on the power semiconductor switches, the ZVS range, and reverse power flow limitation in the proposed converter.

Chapter 4 explains the detailed design procedure and improved secondary side phase shift plus duty cycle control scheme for the proposed dual-phase LLC resonant converter. It presents the design procedures of the resonant tank components, especially the high-frequency transformer design. It also discusses the proposed modulation scheme in detail, along with theoretical power loss analysis in the proposed converter.

Chapter 5 represents the simulation and experiment results of the proposed converter for the wide load and input variations. The organization of this chapter is such as that; firstly, each part of simulation and experiment results is explained separately. After that,

a comparison is drawn among theoretical, simulation, and experimental results to validate the steady-state analysis. Then the estimated loss breakdown and measured efficiencies for the entire operating range are explained. Finally, various comparisons of the designed converter are drawn with the state-of-the-artwork based on parameter values, components usage, and cost.

Chapter 6 summarizes and concludes the primary outcomes of the thesis, along with a brief mentioning of the scope of future research work.

CHAPTER 2: LITERATURE REVIEW

2.1 Introduction

This chapter analyzes a range of bidirectional DC-DC converter (BDCs) topologies to define the suitable topologies for the required applications. First, an overall generic overview of bidirectional DC-DC converter topologies is presented, which are further classified based on galvanic isolation, the types of resonant tanks, and the switched networks. The benefits and the drawbacks of the converter topologies are also discussed. The various control strategies and their modifications, as mentioned in the literature, are classified and critically reviewed. Lastly, a comparison of the selected topologies based on their characteristics and efficiencies has been made for the wide input voltage range and wide load range applications.

2.1.1 Overview of Bidirectional DC-DC Converters

The classification of the bidirectional DC-DC converters can be broadly done into two groups, namely; non-isolated and isolated bidirectional DC-DC converters. The power transfer in the non-isolated converter takes place without magnetic isolation (Das et al., 2010). Although they suffer from the lack of galvanic isolation advantages namely increased step-up/step-down voltage gain, the non-isolated converters have a simpler configuration and are light-weight shielded from any magnetic interference due to the galvanic isolation. Hence, for particular applications, these characteristics act as defining criteria considering weight and size limitations. On the other hand, the isolated converters involve the conversion of DC voltage into AC voltage, which further passes through high-frequency transformers and is finally rectified into DC voltage through suitable rectifiers. The voltage gain range of the isolated converter is usually higher than the non-isolated converters. Figure 2.1 depicts a topological structure based taxonomy of bidirectional DC-DC converters.

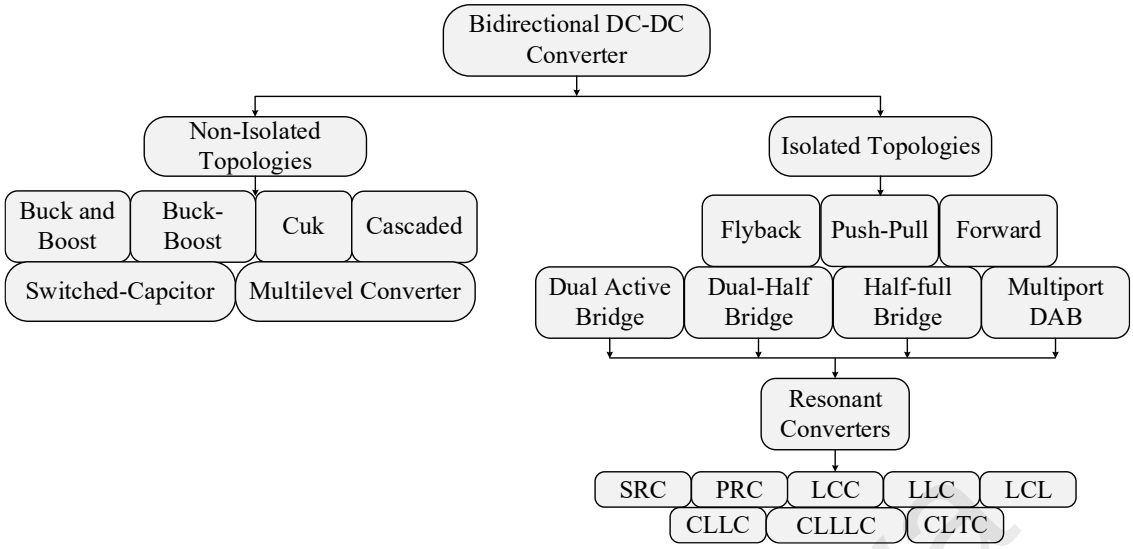

Figure 2.1 Classification of the bidirectional DC-DC converters

2.1.1.1 Non-Isolated Bidirectional DC-DC Converters

A non-isolated bidirectional converter mainly consists of modifying the unidirectional converter topology by incorporating a controlled switch (MOSFET/IGBT) to a diode and an antiparallel diode to the controlled switch. On the note, non-isolated converters are introduced based on the simple DC-DC converters such as buck, boost, buck-boost, Ćuk, etc. A number of topologies are proposed that are based on the techniques of voltage lifting such as interleaving, multilevel, switched capacitor, etc. The resonant version of a non-isolated converter generally involves a resonant tank between the two switching networks (Rathore et al., 2016), as shown in Figure 2.2.

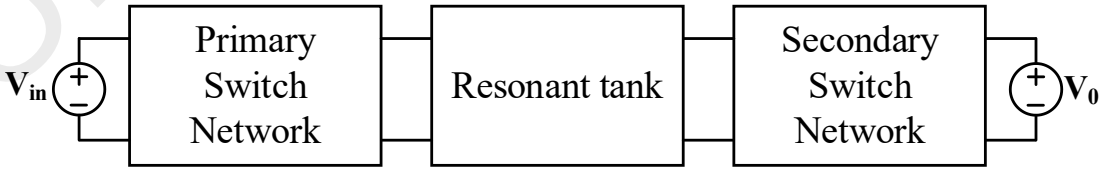

Figure 2.2 A general layout of Non-isolated bidirectional resonant converter

Based on the basic buck and boost converter, the fundamental bidirectional converter was introduced in 1984 (Matsuo & Kurokawa, 1984). This bidirectional topology is actually realized from the unidirectional buck and boost converter, as depicted in Figure 2.3. The

derived bidirectional converter is realized when the unidirectional switches of the traditional buck and boost converter are replaced by the bidirectional power switches. The converter works as a boost converter in the forward direction and as a buck converter in the reverse direction.

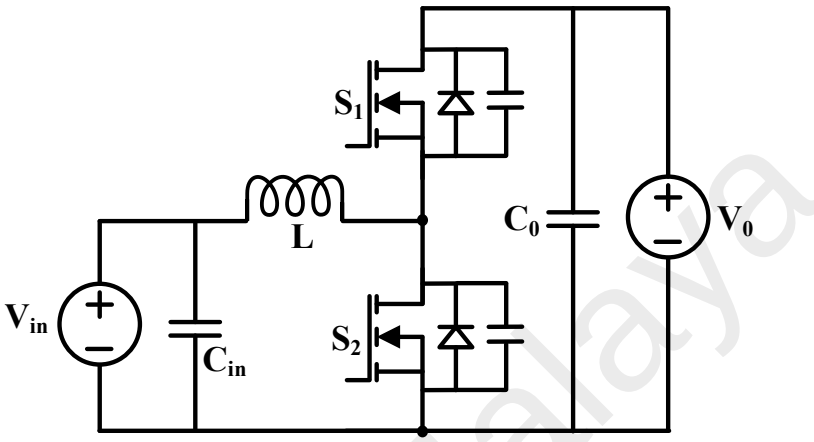

Figure 2.3 Buck and Boost derived bidirectional converter (Matsuo & Kurokawa, 1984)

The buck-boost converter can be derived from the same process used to modify a unidirectional into a bidirectional converter (Caricchi et al., 1994), as in Figure 2.4.

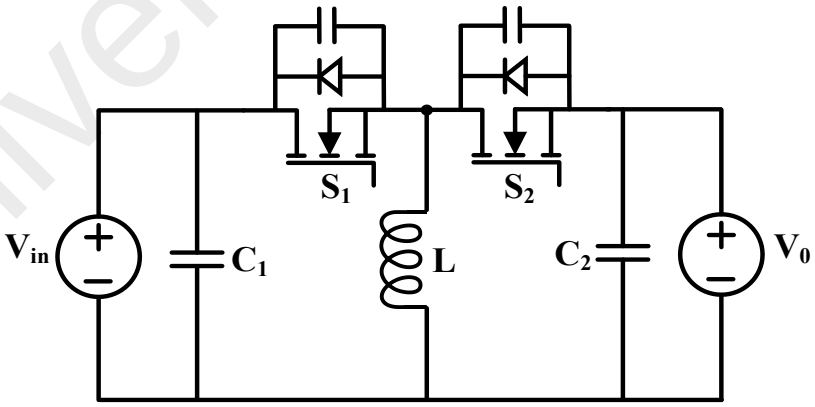

Figure 2.4 Buck-Boost derived bidirectional converter (Caricchi et al., 1994)

In addition to the basic buck-boost converter feature, namely the ability to buck or boost the voltage level, the bidirectional buck-boost converter benefits from the ability to provide a negative output voltage in both directions of the power flow.

The Ćuk converter (Middlebrook et al., 1978), known for its characteristics such as input and output current continuity, can be transformed into a bidirectional topology as shown in Figure 2.5 by using two bidirectional power switches in the place of the unidirectional power switch and the diode of the original circuit. In order to eliminate inductor/output current ripples, a coupled inductor variant of the conventional Ćuk converter was initially presented (Ćuk, 1983). This technique was also employed for the bidirectional Ćuk converter, which provided the basis for further work on the control of the coupled-inductor bidirectional Ćuk converter (Majo et al., 1992).

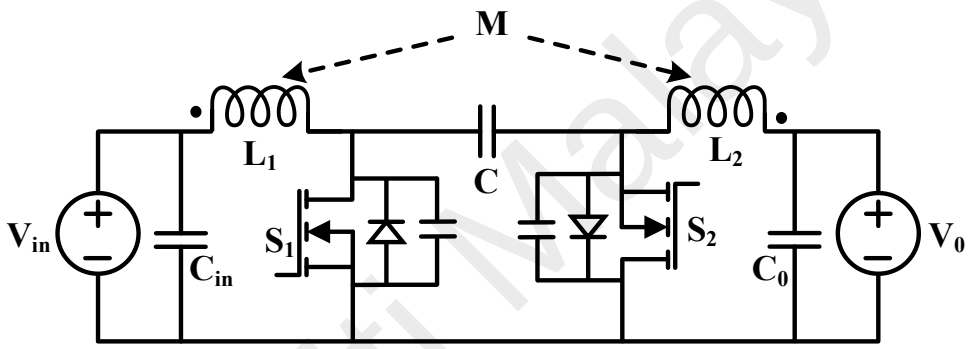

Figure 2.5 Ćuk derived bidirectional converter (Middlebrook et al., 1978)

To increase the voltage boost capacity and reduce the current stress of the converter, two or more converters can be connected in a cascaded manner. Figure 2.6 shows the basic cascaded, non-isolated, bi-directional DC-DC converter that was used initially for EV applications (Caricchi, Crescimbini, Capponi, & Solero, 1998). This converter is the result of cascading two bi-directional buck-boost converters. Although more elements are used compared to the basic bi-directional buck-boost converter, this configuration benefits from a higher voltage gain ratio with the same switch duty cycle. In addition, the inductor current ripples and stress, the current stress of switches, diodes, and capacitors have been decreased, enabling the converter to operate at higher power levels (Lee & Yun, 2019).

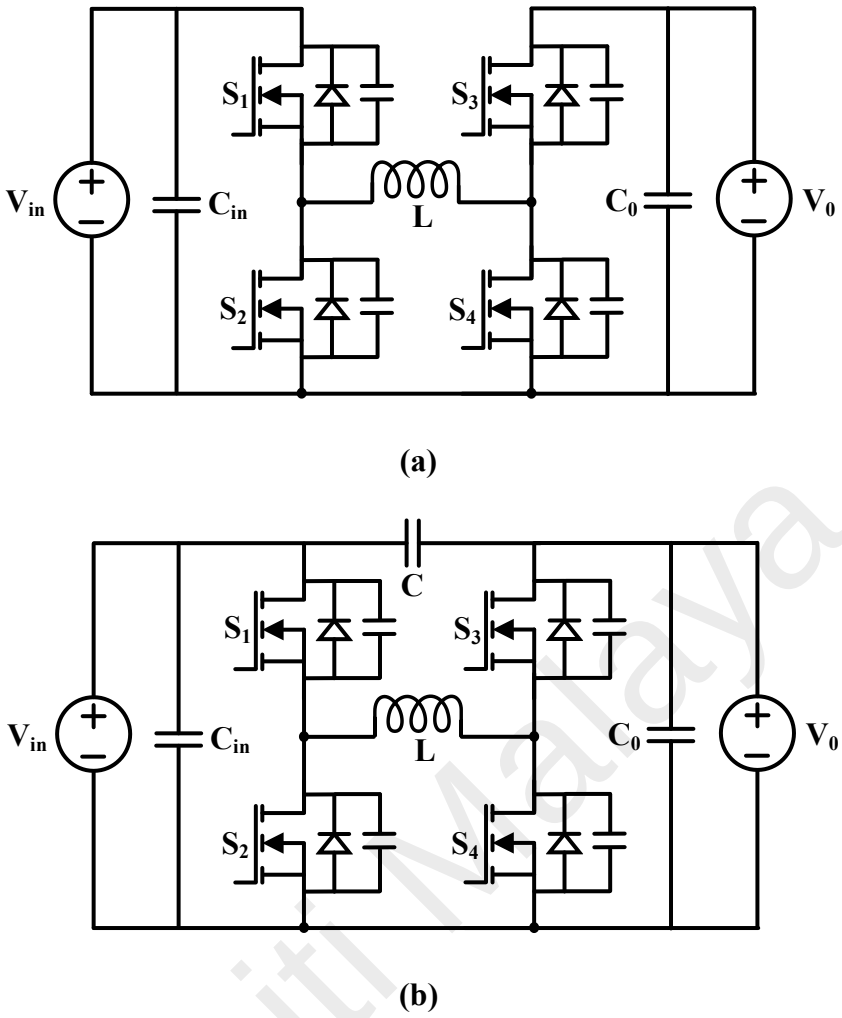

Figure 2.6 Cascaded bidirectional converter (a) (Caricchi, Crescimbini, Capponi, et al., 1998), (b) (Lee & Yun, 2019)

The switched-capacitor (SC) cell can be used to improve the efficiency of the converter by enhancing the voltage boost capability. Figure 2.7 demonstrates a bidirectional converter that increases the voltage conversion ratio using an SC cell. The converter cells are realized by evolving into a bidirectional configuration from a unidirectional SC cell (Chung et al., 2003). For SC-based topologies, there is no inductor, and therefore the magnetic use and the heavyweight imposed by the inductor are avoided. Although the converter does not use any inductor, a continuous input current can be generated by the converter by paralleling two identical cell strings and operating them in the anti-phase, which can be expanded by adding cells.

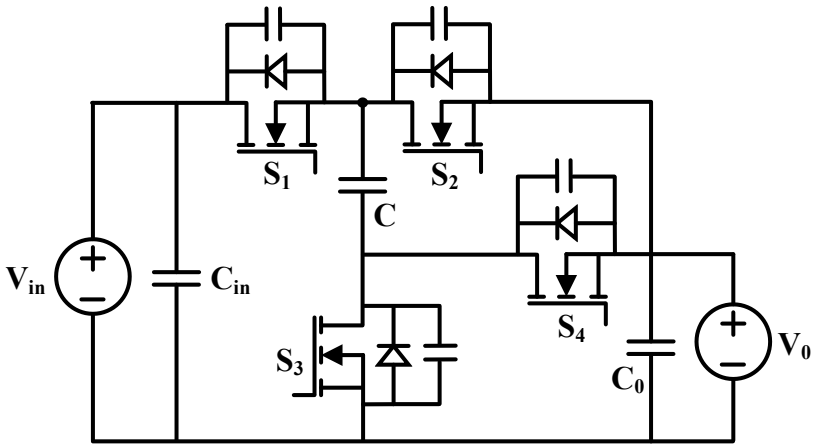

Figure 2.7 Switched-Capacitor (SC) bidirectional converter (Chung et al., 2003)

A multilevel bidirectional DC-DC converter, as proposed in (Peng, Zhang, & Qian, 2002), is shown in Figure 2.8. In this topology, for a high voltage gain, a switching module is used as a repeat pattern in each step.

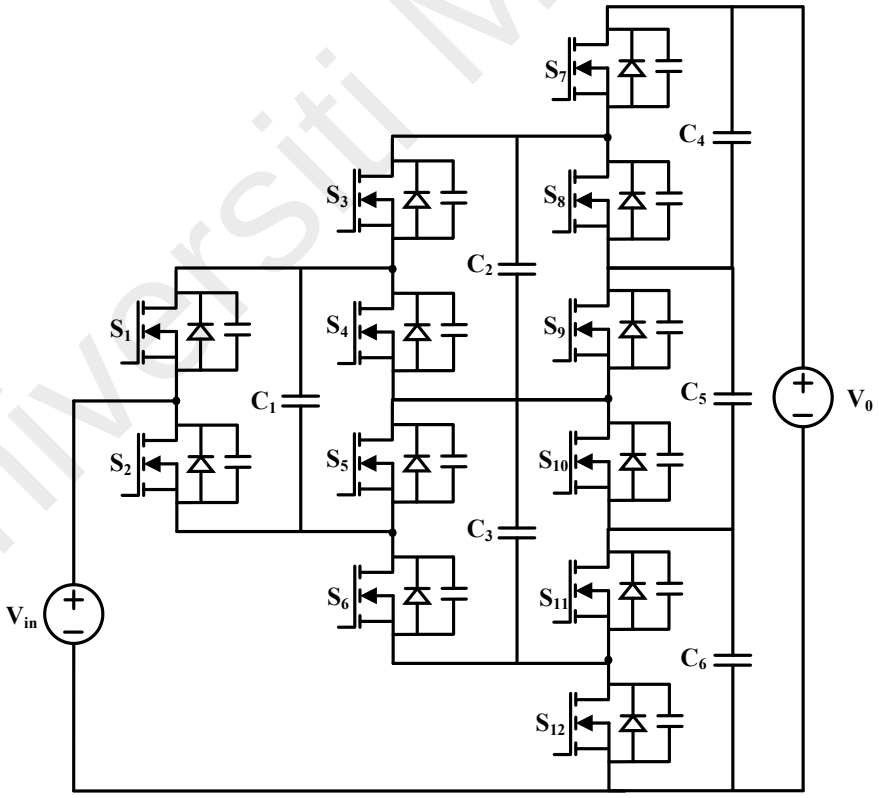

Figure 2.8 Multilevel bidirectional converter (Peng, Zhang, & Qian, 2002)

Initially, the converter was used for automotive dual voltage systems. As there is no inductor, the converter's weight and size are significantly lower than those using magnetic materials.

Although the non-isolated bidirectional converters have evident merits of reduced cost, decreased magnetic weight, larger conversion ratio, high efficiency and power density (C. C. Lin et al., 2013). However, above these all, the converter systems would fail to operate if there is any short circuit in any part of the switching network of the converter. Henceforth, the need for galvanic isolated to provide protection and enhance the reliability of the system has driven the isolated converter's engagement in a range of applications. Because of this, the isolated converters are drawing much more attention from the current researchers as compared to the non-isolated converters.

2.1.1.2 Isolated Bidirectional DC-DC Converters

Galvanic isolation is one of the encouraging ways of achieving an increased voltage gain ability with addition of an added degree of freedom to the converter's output, namely the winding turn ratio, and making it ideal for applications requiring wide ranges of input voltage and load regulation (Gorji et al., 2017). In addition to provide an enhanced voltage gain ratio, isolation will give additional advantages such as the option of multi-input or multi-output topologies and giving protection between the input and output side for sensitive loads that are susceptible to faults, and hence safety is a noteworthy concern in them. The high-frequency transformer facilitates isolation by impedance matching between the input and output side, thus protecting the entire converter system from the short circuit conditions (Ruseler & Barbi, 2013).

A numerous ways exist to enhance the voltage boost ability of the buck-boost converters with non-isolation. Nonetheless, the flyback converter is realized when a transformer replaces the buck-boost converter's inductor in case of the magnetic isolation

requirement and as shown in Figure 2.9. The converter's gain in forward power flow is obtained by applying the volt-second and charge-second balance, which is the same as the flyback converter's voltage gain ratio as expected. It should be noted that consideration needs to be given to the transformer design procedure, and a voltage clamp snubber is needed to suppress the flyback transformer's leakage current. This topology has been further varied in the literature to improve its voltage gain (Delshad & Farzanehfard, 2010).

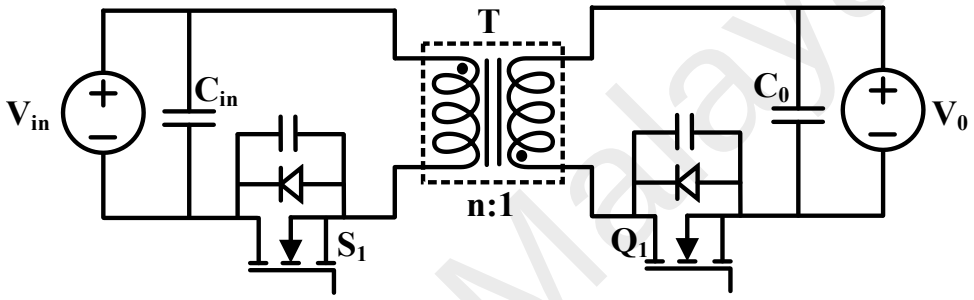

Figure 2.9 Flyback bidirectional converter (Delshad & Farzanehfard, 2010)

The bidirectional push-pull converter (Figure 2.10) was suggested to allow the power flow in both directions based on the unidirectional push-pull converter. The converters use a multi-winding transformer to convert the power, just like the unidirectional push-pull converters. A three-phase bidirectional push-pull converter was also proposed to operate this topology in high-power applications (Kwon et al., 2016).

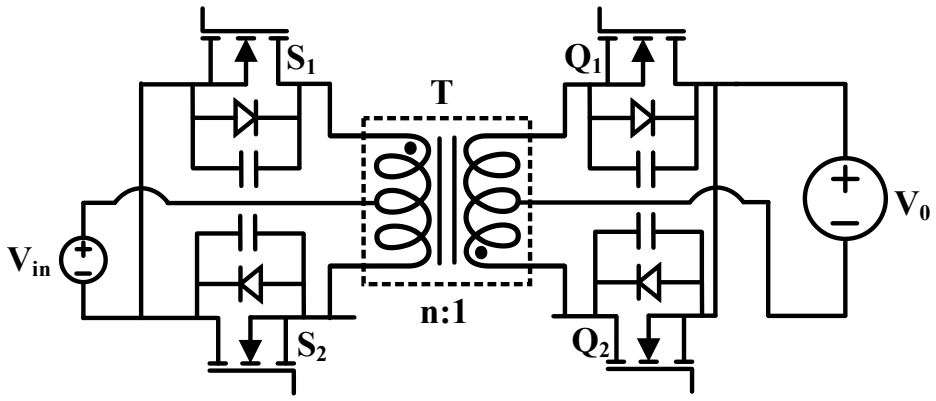

Figure 2.10 Push-pull bidirectional converter (Kwon et al., 2016)

On account of the unidirectional forward converter, the bidirectional forward converter was suggested in (Lin, Chen, Lee, & Chiang, 2008), as shown in Figure 2.11. To achieve zero voltage switching in the converter, a clamped circuit can be used. Further investigation on the bidirectional forward DC-DC converter was carried out in (Khodabakhshian et al., 2016), where the leakage inductance of the transformer is used as the resonant inductor to propose the converter's resonant version. The above-mentioned isolated topologies have been configured in the literature based on the desired application and features such as Forward-Flyback (F. Zhang & Yan, 2009), Push-pull Forward (Z. Zhang et al., 2012), and Flyback-Push-pull (De Souza & Barbi, 2011). The transformer's primary side is derived from one of the aforementioned isolated topologies in these converters, and the secondary side is derived from another, either current-fed or voltage-fed.

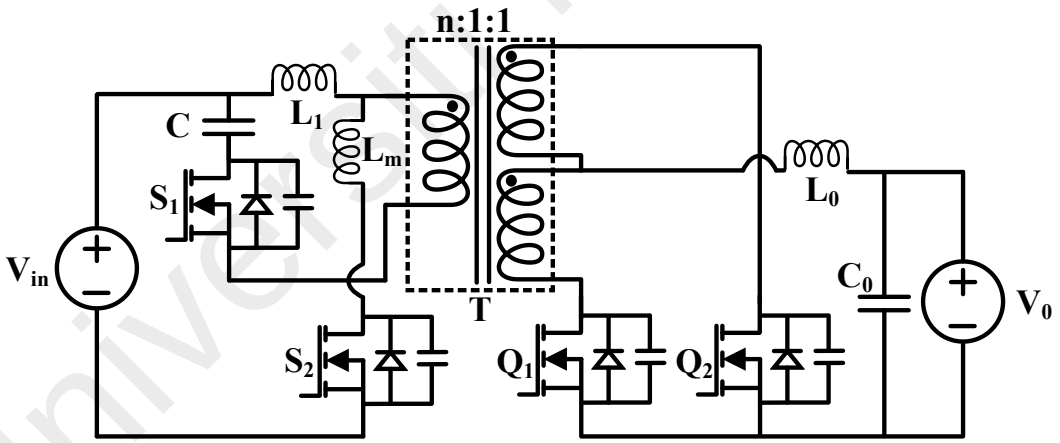

Figure 2.11 Forward bidirectional converter (Lin, Chen, Lee, & Chiang, 2008)

One of the most common strategies is to use back-to-back bidirectional topologies that are separated by a high-frequency transformer generally termed as Dual Active Bridge (DAB). The primary and secondary of the converter can either be voltage-driven or current-driven, half-bridge or full-bridge. Figure 2.12 demonstrates a typical configuration of the DAB converter (De Doncker et al., 1991), using two full-bridge topologies on both sides of the transformer. The power transmission capacity is

proportional to the number of switches in the bidirectional converters (F Krismer & Kolar, 2010). Therefore, having eight power switches in this topology together with galvanic isolation and a high-voltage gain ratio making it ideal for high-power applications like automotive systems (B. Zhao et al., 2014). The current is divided between two legs of the full-bridge converter, reducing the current stress on the power switches relative to the half-bridge topology.

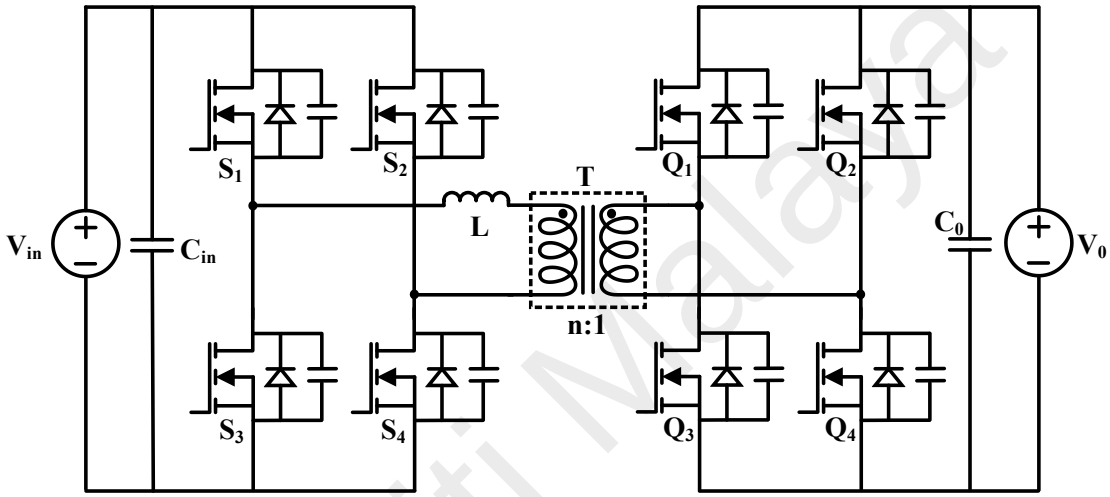

Figure 2.12 A typical Dual Active Bridge based bidirectional converter (De Doncker et al., 1991)

For low-loss silicon carbide (SiC) or gallium nitride (GaN) power switches, the question about the loss of the high number of switches can be overcome. The energy transfer in the converter is regulated by changing the phase shift between the primary / secondary windings of the transformer's AC voltage waveforms. An effective control scheme will lead to optimization of performance, which strengthened the analysis of the converter's control schemes. Since DAB topologies are one of the most common bidirectional isolated topologies, extensive reviews on topologies derived from DAB have been conducted in (B. Zhao et al., 2014).

For low power applications, the half-bridge topology may be useful as compared to DAB, and the number of power switches can be reduced from eight to four. Figure 2.13

shows an isolated bidirectional converter that uses half-bridge topologies fed by the voltage on both sides of the transformer (He & Khaligh, 2017; X. Xu et al., 2007).

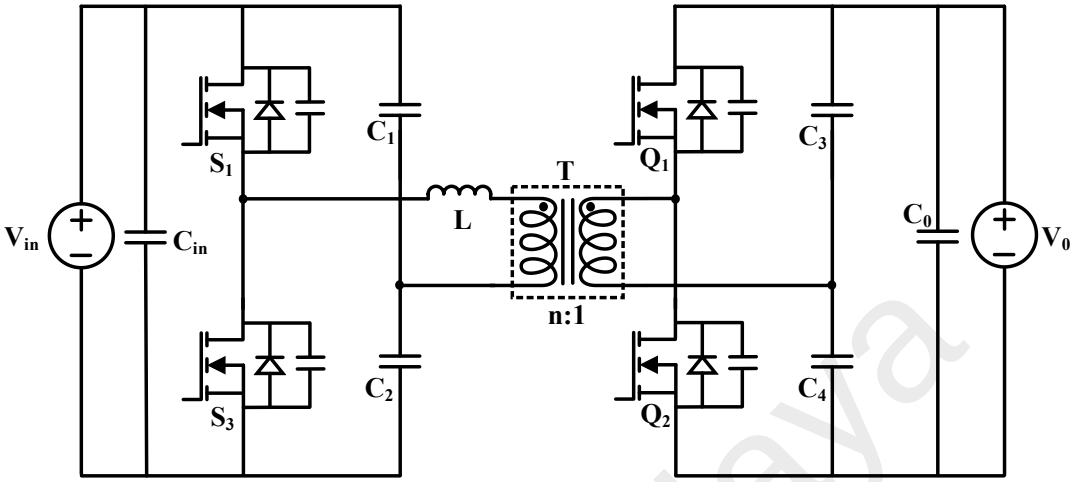

Figure 2.13 Dual half-bridge based bidirectional converter (He & Khaligh, 2017; X. Xu et al., 2007)

The semiconductor switches are operated in a complementary mode, using the short dead time to avoid short circuit and also to charge and discharge the switch junction capacitors to provide soft switching. The switches in a half-bridge are operated in such a manner that a square voltage pulse and an equally divided input voltage into DC-link capacitors can be generated. If there is a voltage imbalance between split capacitors, a separate control is required. Nevertheless, it has reduced switch counts, and the main drawback is the cost and size of the DC-link capacitors. As initially proposed in (Fang Z Peng et al., 2004), the dual half-bridge converter uses a current-fed half-bridge topology on the primary side and a half-bridge voltage-fed topology on the transformer secondary side. As anticipated, the dual-half bridge converter has another version that employs a voltage fed topology in the primary side and a current fed topology on the transformer's secondary side (Li, Peng, & Lawler, 2003). As required in specific applications, the current-fed converter provides a continuous current waveform. Further studies on dual-half bridge converters, such as interleaved dual half-bridge topology, have been proposed

to increase voltage boosting capacity and decrease transformer turn ratio and current stress (S. Park & Song, 2011).

Considering DAB, an isolated bidirectional DC-DC converter (Morrison & Egan, 2000) was proposed for a UPS design using a voltage-fed half-bridge inverter on the primary side and a voltage-fed full-bridge rectifier on the secondary side of the transformer as shown in Figure 2.14 (Morrison & Egan, 2000).

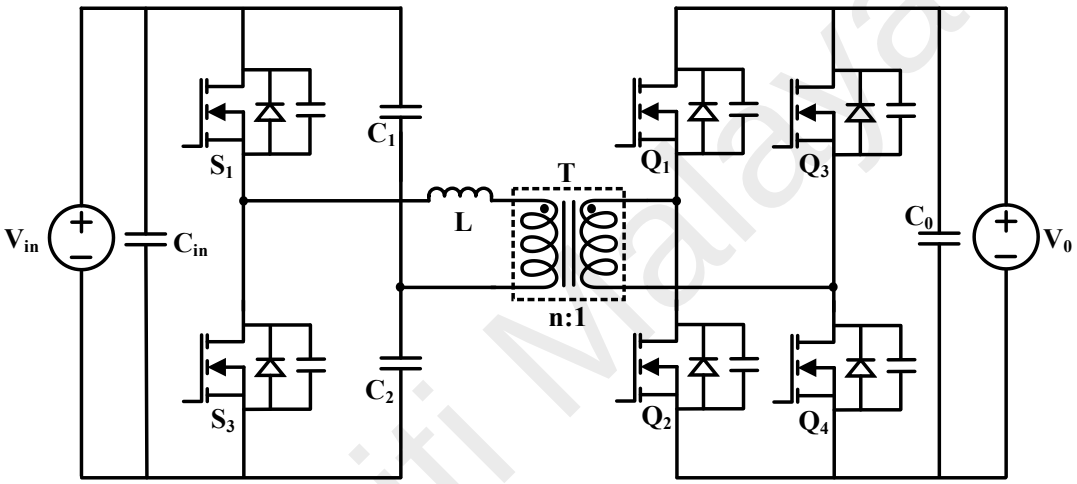

Figure 2.14 Half-full bridge based bidirectional converter (Morrison & Egan, 2000)

It allows for simpler control requirements than DAB owing to reduce switch counts. In particular, it is adequate for the integration of a two-switch buck-boost converter on the half-bridge side to obtain a full UPS configuration. For this configuration, there are other variants, such as full-bridge primary and half-bridge secondary bidirectional DC-DC converter, which has been combined with impedance networks to improve the performance of the converter (Chub et al., 2020).

For the integration of multiple input voltage sources in renewable energy systems and hybrid electric vehicles, multi-input converters are employed (C. Zhao et al., 2008). In (Tao et al., 2006), an isolated bidirectional multi-input single-output DC-DC converter

using multiple DABs with a multi-winding transformer was proposed along with decoupled power flow management, as shown in Figure 2.15.

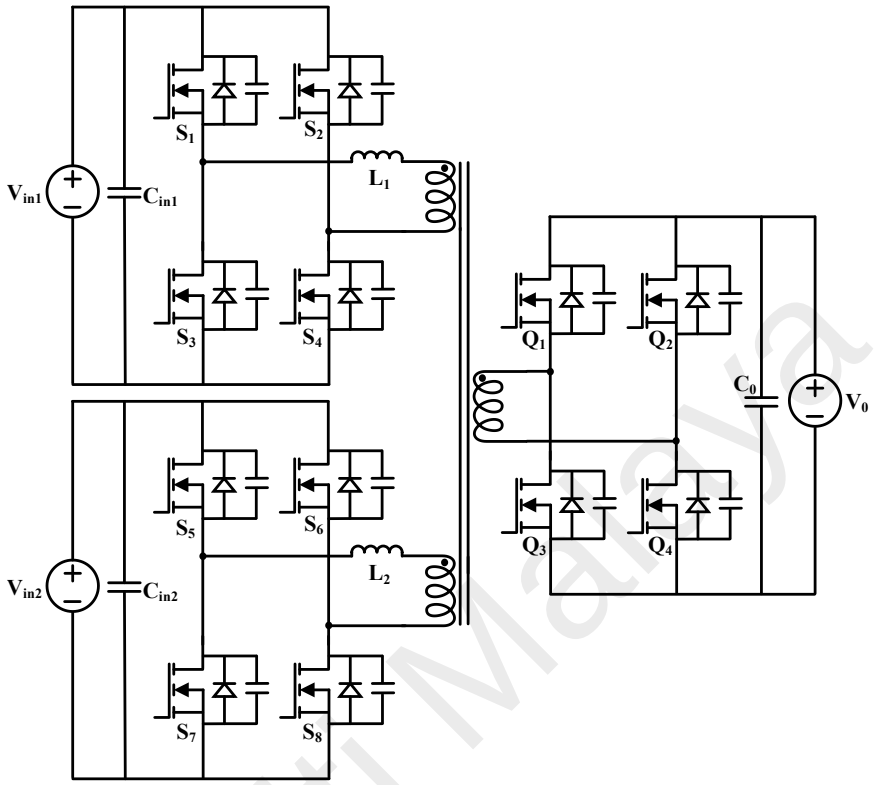

Figure 2.15 Multi-port DAB based bidirectional converter (Tao et al., 2006)

A comparison of the bidirectional converters based on topologies, theoretical voltage gain, switch count, and the parasitic component count has been summarized in Table 2.2. In terms of magnetic capacity, losses, and high-frequency performance, the resonant variant of isolated bi-directional converters is advantageous over isolated PWM-based DC-DC converters. Since the resonant converter enables the operation at high frequency instead of the typical PWM converter, the transformer size can be reduced by using the higher operating frequency. The parasitic elements of the high-frequency transformer contribute to the resonant tank components. The following section discusses a range of resonant converters employing a variety of resonant tanks (two/three/multi-components) with either voltage-fed or current-fed half bridge or full bridge topologies.

Table 2.1 Comparison of bidirectional converters based on topology configuration

Topology	$\frac{V_0}{V_{in}}$	Switch Count	Inductor Count	Capacitor Count	Transformer Windings
Buck-Boost (Caricchi et al., 1994)	$\frac{D}{1-D}$	2	2	2	Not required
Cascaded (Lee & Yun, 2019)	$\frac{1}{1-D}$	4	1	2	Not required
Switched Capacitor (Chung et al., 2003)	2	4	0	3	Not required
Flyback (Delshad & Farzanehfard, 2010)	$\frac{nD}{1-D}$	2	0	2	2
Push-pull (Kwon et al., 2016)	nD	4	1	1	4
Forward (Lin, et al., 2008)	nD	3	1	1	3
DAB (De Doncker et al., 1991)	Varies according to control	8	0	2	2
Dual HB (He & Khaligh, 2017)	Varies according to control	4	0	6	2
Half-FB (Morrison & Egan, 2000)	Varies according to control	6	0	4	2
Multi-port DAB (Tao et al., 2006)	Varies according to control	4*N=12	0	N=3	N=3

2.1.2 Resonant Converters

The conventional PWM converters involve the operation depending on the transfer of the entire load current during turn ON and turn OFF switching cycles. This produces high

switching and power losses that drastically reduces the conversion efficiency. The output voltage of such converters is varied by adjusting the duty cycle of the switching devices. Switching and power fluctuations may not have a large impact on the converter's performance at lower switching frequencies. However, at the increased switching frequency, PWM converters limit their effectiveness due to unregulated switching losses, which could have a significant impact on the performance of the electric system. Another major disadvantage associated with PWM converters is the large EMI because of high *dv/dt* and *di/dt* switching states arising from lossy snubber circuits (Outeiro et al., 2016). To avoid the aforementioned drawbacks, a soft-switching strategy could be a feasible solution to avoid such high switching losses under higher switching frequency operation. This can be realized by zero current and/or zero voltage switching in which the switch voltage and current goes through zero instants during the dead-time switching transitions. It significantly reduces the switching losses, thereby increasing the conversion efficiency of the converter. Hence, the higher operating frequency reduces the size of the magnetic components increasing the power density of the resonant converters. Having the capability of wide voltage regulation, the resonant converters decrease the DC-link capacitor sizing required in the DC-DC converter systems. Nevertheless, the resonant converters have a plethora of advantages; it suffers from a certain amount of drawbacks. The large difference of resonant voltages increases the circulating current in the converter, thereby causing increased conduction losses. The resonant components are high voltage and current stressed because of quite high values of resonant voltages and currents. These drawbacks limit the converter's performance in terms of reduced efficiency and increased component costs.

Figure 2.16 shows the general configuration of the DAB-derived resonant converter, where: a) either a voltage-fed or a current-fed full-bridge converts the DC-AC in the first stage, depending on the desired application; b) in the second stage, a high-frequency

transformer raises the voltage of the ac and provides galvanic insulation. Together with the transformer, a resonant tank is used to achieve ZVS / ZCS and thus increase efficiency (Chen et al., 2010; Jung et al., 2013; Xiaodong Li & Bhat, 2010); c) in the third stage, depending on the required application, either an AC-DC rectification is carried out by a voltage-fed or a full-bridge current fed.

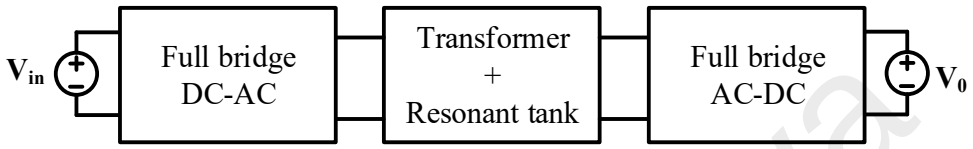

Figure 2.16 A general layout of DAB based resonant converters

A wide range of resonant converter has been presented in the literature based on the variants of resonant tanks. This variation in resonant tanks mainly depends upon the number of the resonant component present in the resonant tanks. The most general DAB based resonant converters are Series Resonant Converters (SRC) and Parallel Resonant Converters (PRC), having two resonant components (Steigerwald, 1992). Moreover, a three-component resonant converter is an LLC resonant converter (X. Li, 2014). It has some inherent soft switching ability, high voltage regulation, and wide load range applications. The following subsections present thorough literature based on different resonant tanks and their characteristics, which are majorly employed in bidirectional DC-DC power conversion systems.

2.1.2.1 Two-component Resonant Converters

The two-component resonant converters have exactly two resonant components, which are mainly connected in either series or parallel manner. It can be broadly classified as:

(a) ***Series Resonant Converters (SRC)***

Based on the general layout of resonant converters, as shown in Figure 2.16, the Series Resonant Converter (SRC) consists of a series-connected LC resonant tank, as depicted in Figure 2.17(a). The resonant tank incorporates a series connection of resonant capacitor C_r, resonant inductor L_r, and the output load. The symmetrical behaviour of the series LC resonant tank helps in achieving the symmetrical operation for forward as well as backward operation in bidirectional DC-DC converters (X. Li & Bhat, 2010). The input impedance of the resonant tank is dependent on the operating switching frequency, and thus, the output voltage of the resonant tank can be controlled by varying the switching frequency.

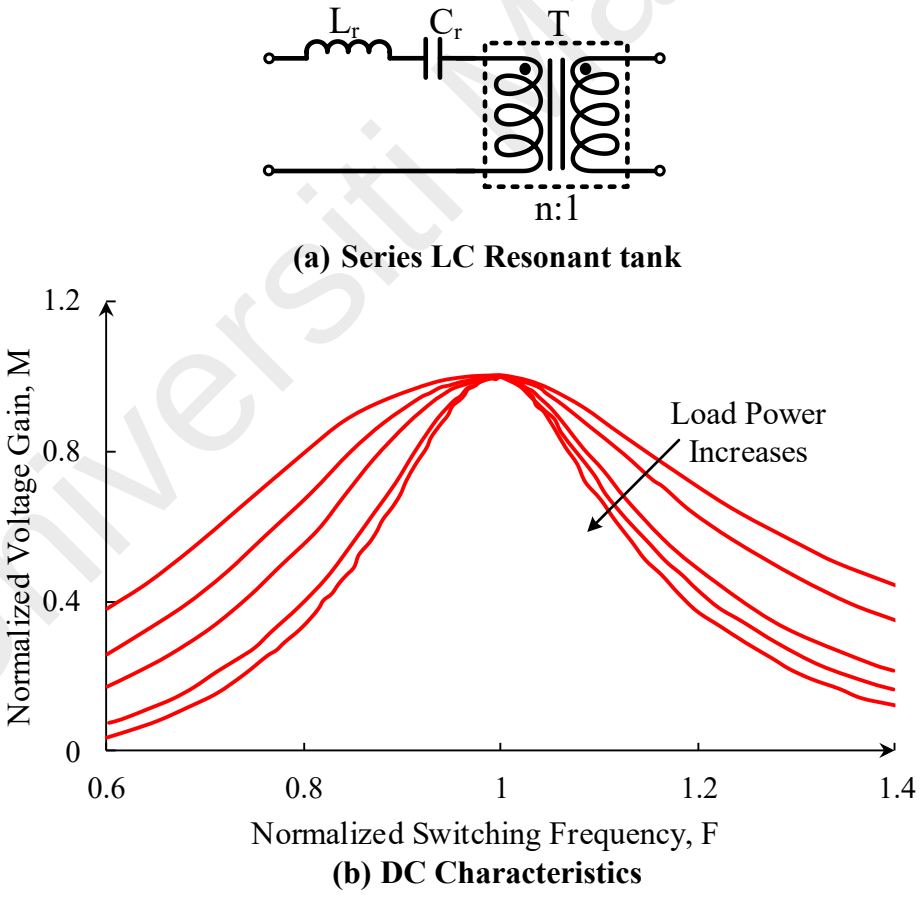

(a) Series LC Resonant tank

(b) DC Characteristics

Figure 2.17 Series Resonant Converter

The DC characteristics of the series LC resonant tank has been shown in Figure 2.17(b). As the input impedance at the resonant frequency f_r ($f_r = 1/2\pi\sqrt{L_r C_r}$) is

minimum and zero, the normalized voltage gain ($M = nV_0/V_{in}$) reaches unity and attains the maximum gain value. As the switching frequency is larger than the resonant frequency, the input impedance becomes inductive, and the input current lags the input voltage across the resonant tank. This lagging inductive resonant current achieves ZVS. It is necessary for converters employing MOSFETs as it reduces the switching losses and EM interferences. For the switching frequency lesser than the resonant frequency, the operating region is termed capacitive region as the input current leads the input voltage. This helps in realizing the ZCS through IGBTs as it reduces large switching losses. As observed from the DC characteristics of the series LC resonant tank, for light load conditions, the voltage gain curves are more gradual. Hence, to regulate the output voltage over a wide load range, a wide switching frequency variation is required (Steigerwald, 1988). For only frequency control, the voltage gain of the converter is limited to unity, restraining the wide gain range requirement. Henceforth, the SRCs are not suitable for wide input/output voltage and load range applications.

(b) ***Parallel Resonant Converters (PRC)***

On the same note of SRC, the resonant tank of the parallel resonant converter consists of two components, namely resonant inductor L_r and resonant capacitor C_r connected in parallel with the output load. The resonant tank schematic is shown in Figure 2.18(a). For the bidirectionality, a symmetric resonant tank can be employed with a similar structure on the secondary side of the transformer, with both resonant capacitors in parallel with the output load. The DC characteristics of the parallel resonant tank over the normalized switching frequency for a range of load conditions are shown in Figure 2.18(b). As observed from the DC characteristics, the maximum gain from the resonant tank depends upon the output load. Also, the maximum gain is not limited to unity as compared to SRC. The gain values can be larger or smaller than unity allowing the PRC to operate in wide input/output voltage range applications. Similar to SRC, to achieve ZVS, the PRC has to

be operated in an inductive slope region, which would be above the maximum gain frequency region. Another significant feature, in contrary to SRCs, is that the slope of DC gain characteristics is steeper under light load conditions. For PRC, the needed frequency

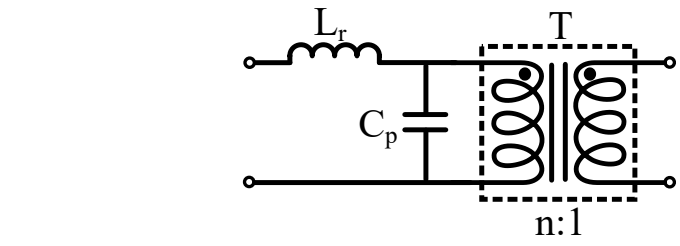

(a) Parallel LC Resonant tank

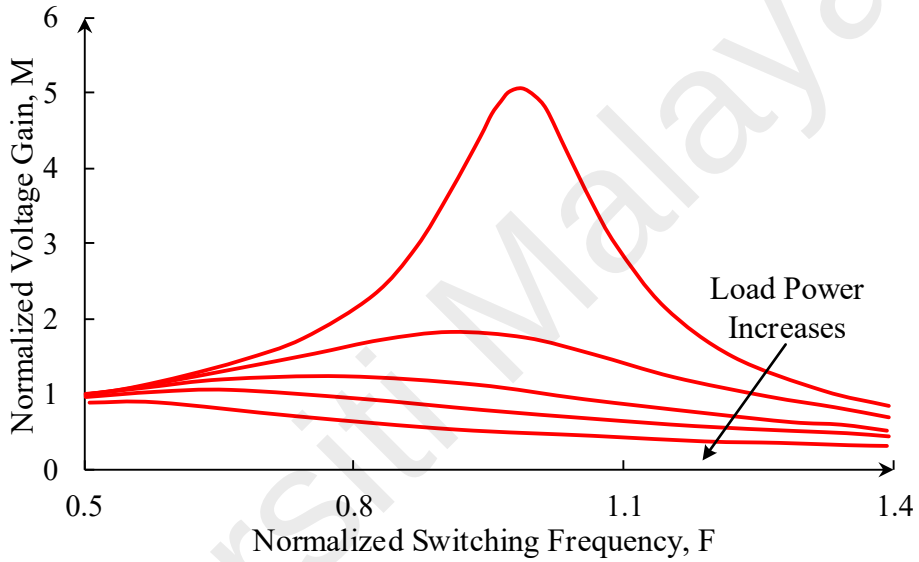

(b) DC Characteristics

Figure 2.18 Parallel Resonant Converter

variation to control the voltage is narrower than for SRC, provided the input and load range remain the same. Similar to SRC, the major drawback of PRC is the circulating current that causes high conductivity loss and low performance for light load condition as the input impedance is inductive to achieve the ZVS condition, which is regulated by the inductive component and less influenced by the load resistance resulting in a significantly larger resonant current. Moreover, the unblocked DC component of the inverter voltage accelerates the saturation of the transformer winding.

2.1.2.2 Three-component Resonant Converters

(a) ***Series-Parallel Resonant Converters (SPRC/LCC)***

The resonant tank of a series-parallel resonant converter consists of the combination series resonant tank and the parallel resonant tank (A K S Bhat, 1993). SPRC, also termed as LCC, consist of two resonant components L_r and C_r in series and C_p as a third resonant component in parallel with the inverter output as depicted in Figure 2.19(a). It combines the advantages of SRC and PRC for operation (R. Yang et al., 2014). The tank has dual resonant frequencies, mainly, open circuit (OC) resonant frequency f_{0C} and the short-circuit (SC) resonant frequency f_{SC}. The features of the LCC resonant tank are based on the chosen value of the components. It operates as SRC in the reverse mode of operation, i.e.

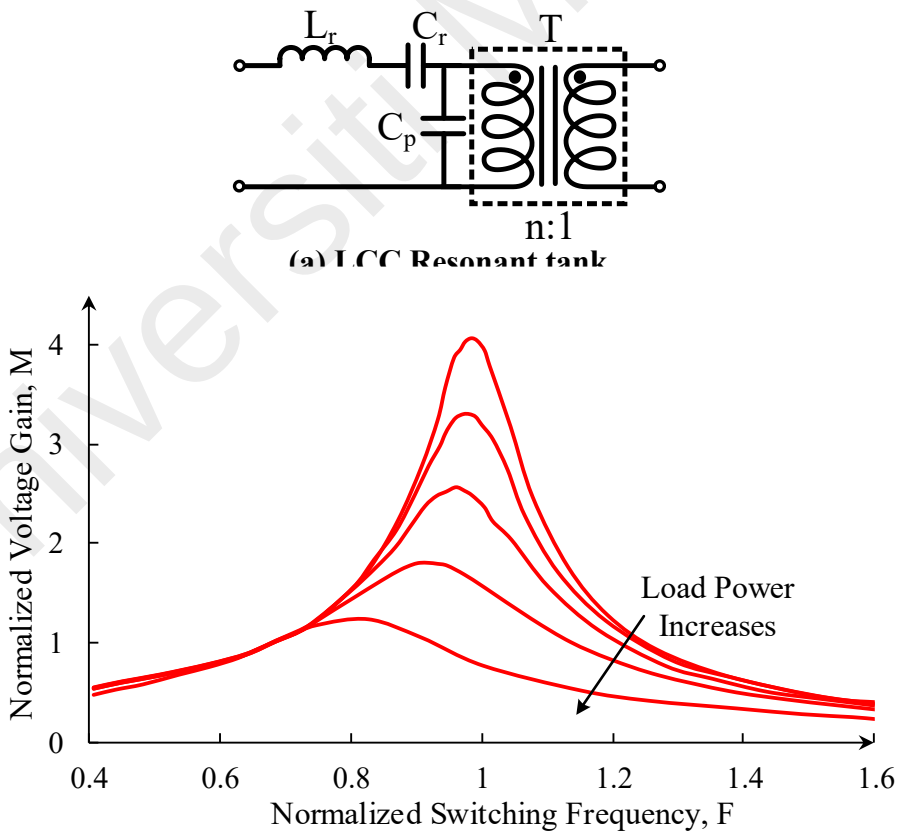

(a) LCC Resonant tank

(b) DC Characteristics

Figure 2.19 Series-Parallel Resonant Converter

power transfer from the transformer secondary to its primary side (Khalil-Abaker et al., 2016). It is also more analogous to the SRC for smaller values of C_p. This reduces the robustness of the converter in light load conditions like SPC with a small C_p value. Otherwise, for higher C_p values, it operates like a PRC. Therefore, the circulating power flow in the resonant tank is independent of the load that decreases the efficiency under light load conditions. Hence, the C_p value must be chosen such that the no-load output voltage can be controlled, making the circulating current independent of the load condition. In (Steigerwald, 1988); however, it is noticed that making C_s equal to C_p is a good alternative to resolve the SRC and PRC deficiency. Figure 2.19(b) represents the DC characteristics of the LCC resonant tank with respect to normalized switching frequency for C_s=C_p. As observed, the SC resonant frequency is lesser than the OC resonant frequency, and the voltage gains do not coincide at SC resonant frequency. As stated previously, MOSFET switches can only achieve ZVS in the inductive region of the DC characteristics.

(b) ***LLC Resonant Converters (LLC-RC)***

As shown in Figure 2.20(a), the LLC resonant converter is a three-resonant component converter. Contrary to LCC, a parallel inductor, L_m (magnetizing inductance) across the primary side of the transformer, is considered in the LLC resonant tank. Though this magnetizing inductance is present in every transformer irrespective of the resonant tank, its value in SRC is much larger than the resonant inductor and does not participate in resonance. On the other hand, in LLC, the magnetizing inductor has a comparable value with respect to its resonant counterpart, making it to be no longer ignored in resonance operation. As the magnetizing inductor is already integrated into the transformer and a transformer leakage inductor can also be considered as the resonant inductor, it is possible to convert the available SRC circuit to LLC resonant tank with no added extra cost (Choi, 2007; Liang et al., 2005; B. Yang et al., 2002).

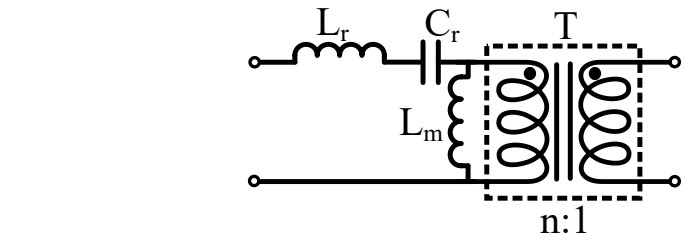

(a) LLC Resonant tank

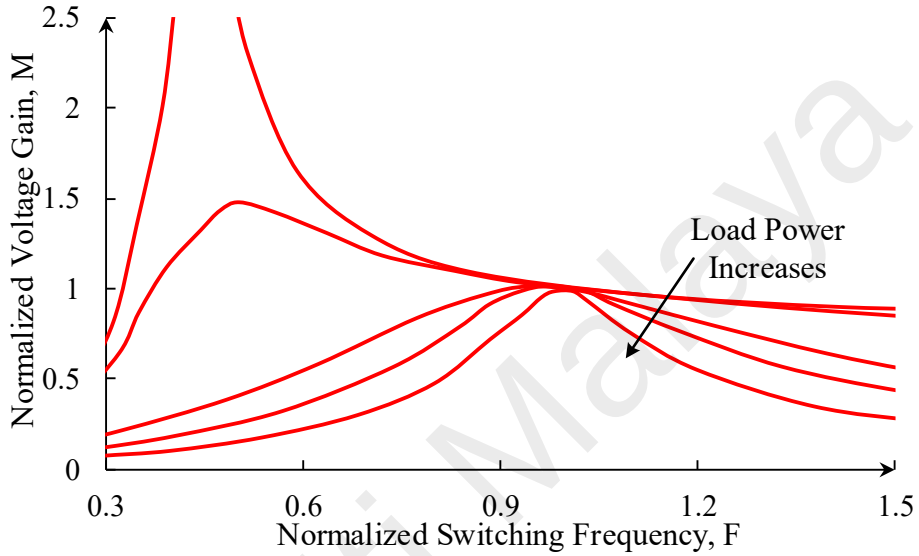

(b) DC Characteristics

Figure 2.20 LLC Resonant Converter

Similar to LCC, the LLC resonant tank exhibit two resonant frequencies: $f_{OC} = 1/2\pi\sqrt{(L_r + L_m)C_r}$ is the open-circuit resonant frequency and $f_{SC} = 1/2\pi\sqrt{L_r C_r}$ is the short-circuit resonant frequency. Nonetheless, f_{OC} is greater than f_{SC} that which suggests that the load-independent point of unity gain exists at a higher frequency than the maximum gain point based on prior LCC study, as shown in Figure 2.20(b). This characteristic of the LLC resonant tank enables the converter operation at peak efficiency point and that too within the ZVS range for which LCC fails in order to ensure ZVS. Moreover, the LLC brings together the benefits of SRC and PRC: the wide voltage gain range is observed, as the gain can be greater or less than unity. The switching frequency range is reduced as the different gain curves converge to the unity gain point under changing load conditions.

(c) *LCL Resonant Converters (LCL-RC)*

Similar to LLC, LCL resonant converter consists of a three-component resonant tank. An external inductor is added to the primary or secondary side of the transformer to modify the conventional SRC resonant tank. Unlike the LLC resonant tank, in which the magnetizing inductor as a whole participate in resonance, in LCL resonant tank, a part of magnetizing inductance along with an added parallel inductor constitutes the resonant network (Ashoka K.S. Bhat, 1994). The circuit configuration is shown in Figure 2.21(a).

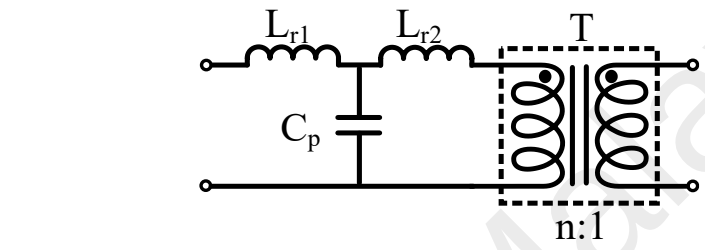

(a) LCL Resonant tank

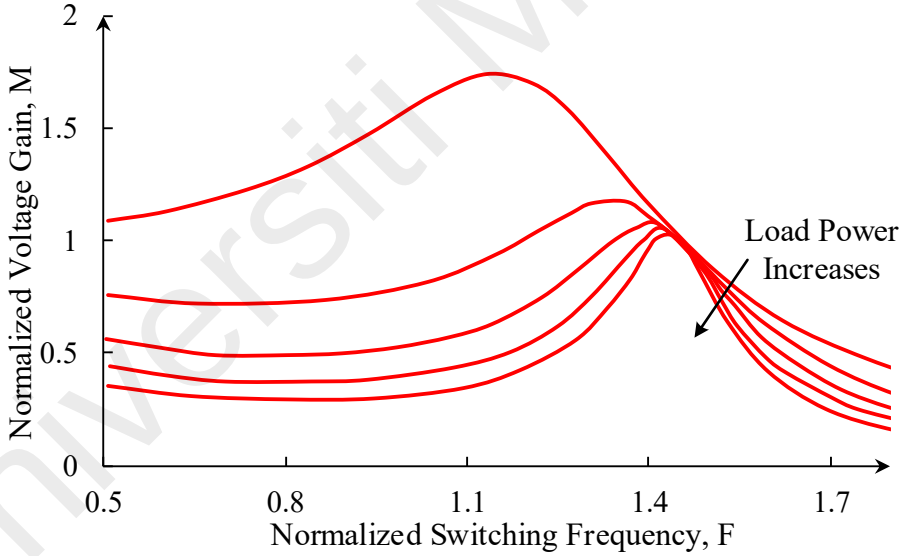

(b) DC Characteristics

Figure 2.21 LCL Resonant Converter

The DC characteristics of the LCL resonant tank is shown in Figure 2.21(b), which exhibits the point of unity gain for the above resonance switching frequency. As the voltage gain characteristics are load-independent, the converter requires a narrow range of switching frequency to achieve the desired gain from full load to a light load. For the explained advantages of ZVS, the operation is in the above resonance region.

2.1.2.3 Multi-component Resonant Converters

(a) ***CLLC Resonant Converters (CLLC-RC)***

As shown in Figure 2.20(a) and Figure 2.21(a), the four-component resonant tanks are relatively similar to that of the LLC resonant tank except for an additional resonant capacitor in each design. These two types of CLLCs can be combined in a bi-directional converter (Wei et al., 2010). Figure 2.22 shows the forward power flow resonant tank network, and in Figure 2.23, the resonant tank for backward power flow is represented.

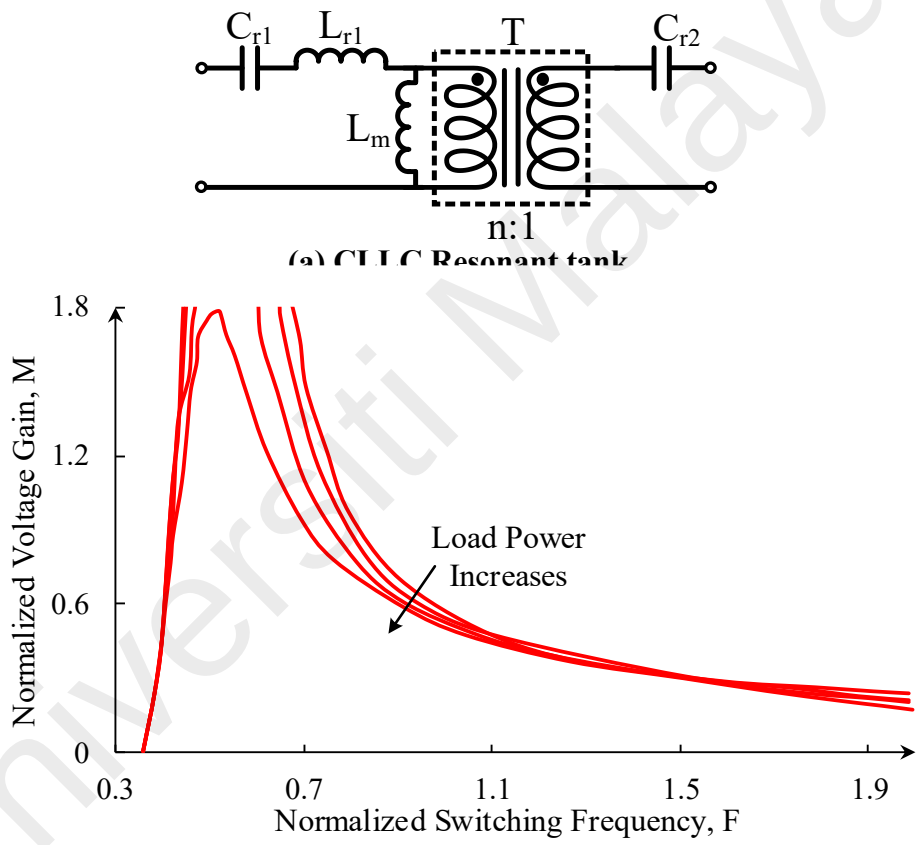

(a) CLLC Resonant tank

(b) DC Characteristics

Figure 2.22 CLLC (forward) Resonant Converter

Both resonant tank configurations have two identical inductors: Lr and Lm, in which the leakage inductance of primary as well as secondary windings of the transformer can be combined as the resonant inductor, and the magnetizing inductance is considered as Lm. The resonant capacitors C_{r1} and C_{r2} can also be considered as blocking capacitors according to the current flow direction in order to achieve the flux balance in

the transformer. As observed from Figure 2.22(b) and Figure 2.23(b), it can be highlighted that both resonant tanks DC characteristics exhibit the peak gain points on each side of the unity normalized switching frequency. CLLC (forward) resonant tank has a wide inductive slope region and an improved peak gain for reduced switching frequency.

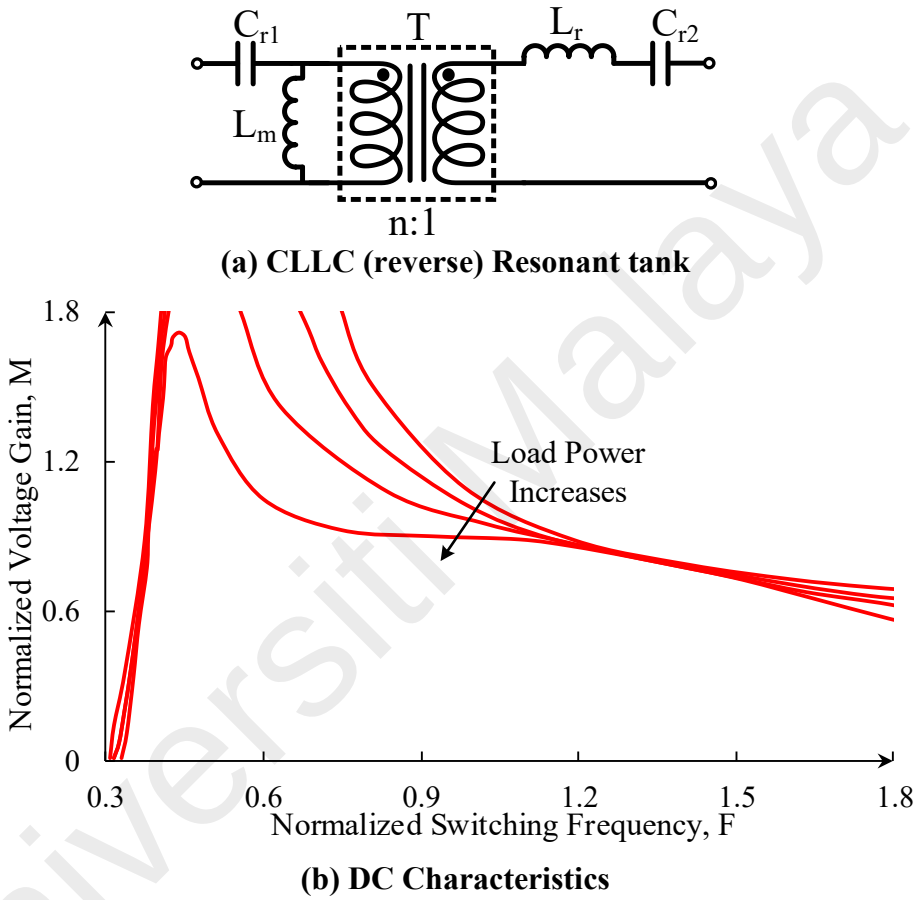

(a) CLLC (reverse) Resonant tank

(b) DC Characteristics

Figure 2.23 CLLC (reverse) Resonant Converter

However, the gain in forward mode resonant tank at higher switching frequency is considerably lower than CLLC (reverse) resonant tank, and particularly the difference is obvious in the region of normalized switching frequency more than unity. However, in both types of resonant tanks, the voltage gain is reduced as the switching frequency decreases for high-load conditions.

(b) ***CLTC Resonant Converters (CLTC-RC)***

CLTC resonant converter, as proposed in (C.-S. Wang et al., 2019), consists of an auxiliary transformer and extra resonant capacitor that are added based on LLC resonant tank. Owing to the added transformer and capacitor, CLTC resonant tank identifies as a multi-component resonant tank. CLTC accumulates the advantages of SRC, LLC, and CLLC resonant tanks. The circuit configuration of the CLTC resonant tank is shown in Figure 2.24(a).

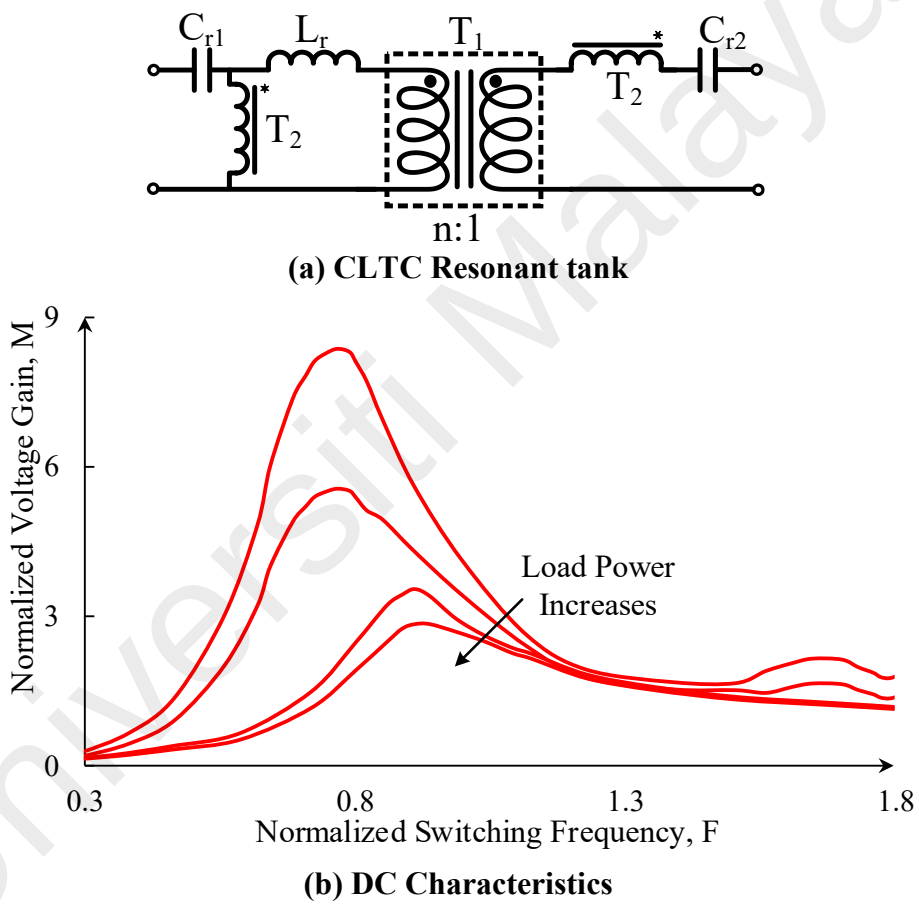

(a) CLTC Resonant tank

(b) DC Characteristics

Figure 2.24 CLTC Resonant Converter

Similar to LLC, the magnetizing inductance of the T_1 transformer is used to achieve higher peak voltage gain. The DC voltage gain characteristics with respect to normalized switching frequency for changing load conditions have been depicted in Figure 2.24(b). The transformer T_2 operates similar to transformer operation in SRC in which the magnetizing inductance of T_2 is used to obtain steeper slope characteristic under heavy-

load conditions. The resonant inductor L_{r1} and resonant capacitor C_{r1} are used to achieve ZCS and ZVS for the entire load range. The secondary resonant capacitor C_{r2} is added to assist in symmetrical bidirectional power flow identical to CLLC resonant converter.

(c) *CLLLC Resonant Converters (CLLLC-RC)*

In order to achieve the symmetrical operation of both forward and backward power flow, the LLC resonant tank can be changed to a CLLLC resonant tank with five reactive components, as shown in Figure 2.25(a). Because of its symmetrical configuration, it is useful in bidirectional power flow applications (Jung et al., 2013). The resonant inductors L_{r1} and L_{r2} constitute the leakage inductance from the primary and secondary windings of the transformer. The adjustable flux balance is provided by the resonant capacitors C_{r1} and C_{r2}.

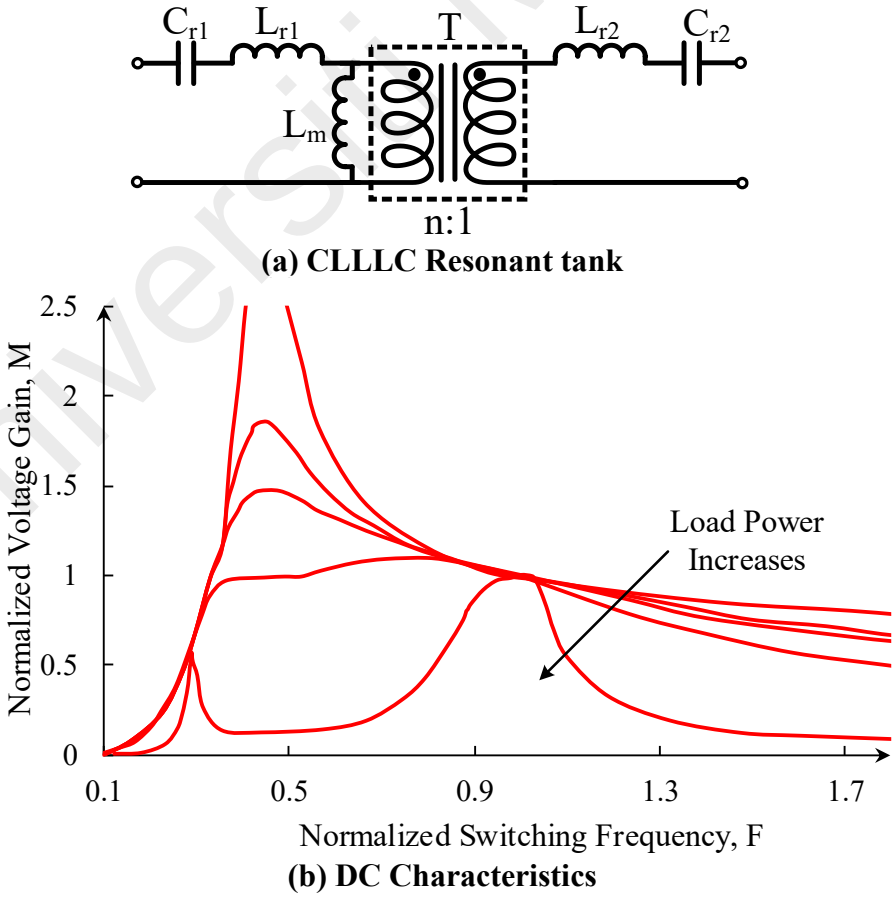

Figure 2.25 CLLLC Resonant Converter

Figure 2.25(b) displays the voltage gain characteristics of the CLLLC resonant tank as the function of the normalized switching frequency. The resonant tank exhibits the peak gain point at the decreased resonant frequency as the magnetizing inductance participates in the resonance operation. Contrary to the LLC resonant tank, with a wider inductive slope region, it displays increased peak gain under light-load conditions. Nevertheless, for switching frequency equivalent to the resonant frequency, the voltage gain deviates from unity irrespective of load. However, the voltage gain can be reduced as the operating frequency decreases during high load conditions. The resonance operation becomes more complex for CLLLC configuration as compared to LLC resonant tank operation because of the addition of the Cr2 capacitor in the circuit.

2.2 Modulation Strategies for the Resonant Converters

In this section, the modulation strategies that have been mentioned for the bidirectional resonant DC-DC converters are discussed, and their important features are critically reviewed. The converter characteristics such as wide voltage gain range, soft-switching range, circulating power flow are all dependent on the employed modulation schemes for the resonant converters. Figure 2.26 presents a taxonomical classification of the mentioned modulation schemes in the literature.

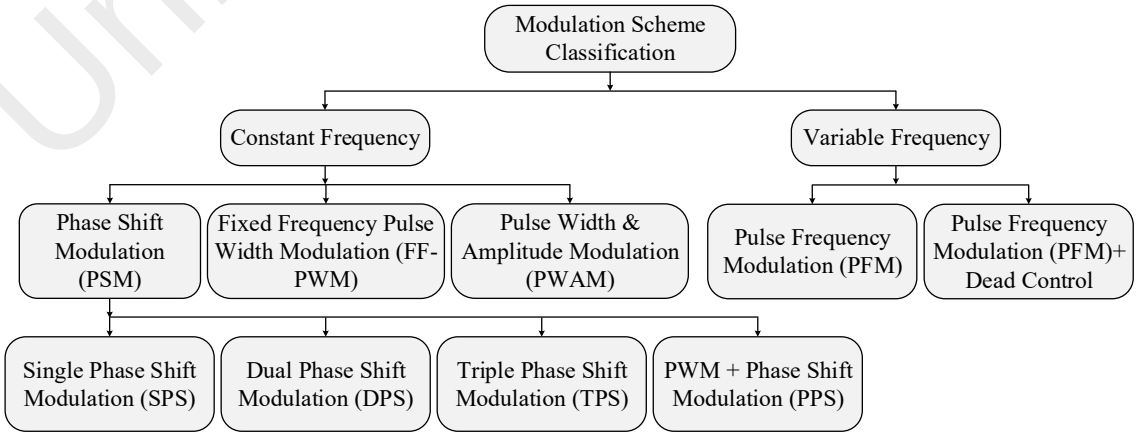

Figure 2.26 Classification of modulation schemes for bidirectional resonant converter

2.2.1 Phase Shift Modulation

Under phase shift modulation, the switches for the same leg can be operated at a 50% duty ratio and 180 degrees out of phase with each other. The modulation scheme generates the gate signal to determine when to turn on and off the power switches. Nonetheless, the phase shift value determines the percentage of overlap between the cross switches, which in turn determines the transferred energy. Hence, various types of phase shift modulation scheme have been introduced to generate the gate signals and achieve the particular control objectives such as wide voltage gain range, ZVS, and reduced circulating power flow in the isolated bidirectional resonant converters (Hua Bai & Mi, 2008; Shakib & Mekhilef, 2017; D. Xu et al., 2004).

2.2.1.1 Single Phase Shift Modulation

The single-phase shift (SPS) modulation employs constant duty cycle to turn ON/OFF the power switches. In SPS, the phase shift is introduced between the primary and the corresponding secondary side switches of the converter. It has been employed for different isolated bidirectional converters such as dual active bridge, three-port or hybrid converters (Mi et al., 2008; Phattanasak et al., 2015; L. Wang et al., 2012).

A dual-bridge LLC resonant converter with fixed frequency single phase shift modulation is presented and investigated in (Xiaodong, 2014) using a modified fundamental harmonic approximation approach. At unity voltage gain, the converter achieves ZVS for all switches under all load conditions. The magnetizing inductance of the HF transformer has been incorporated into the resonant tank to secure ZVS for secondary switches. Because of the low magnetizing inductance value, the converter suffers from high circulating current under light-load condition, thereby degrading the efficiency. To maintain the ZVS over the wide load range, the voltage gain of the converter is limited to unity. As the voltage gain deviates from unity, the converter loses

ZVS ability causing high switching losses. Thus, the converter becomes inadequate for wide input voltage range applications. A 300 W, 48 V prototype has been designed with a peak efficiency of 94.5% at peak load conditions.

A DAB series resonant converter with a tunable resonant tank is presented in (M. Yaqoob et al., 2017) for a wide output voltage and load range. With the switched inductor extending the ZVS range, a simple single-phase shift modulation is used to attain the wide voltage gain and bidirectional power flow. A generic concern with the SPS modulated DAB resonant converter is that the secondary side secondary switches fail to achieve soft switching operation for wide voltage gain under unity, especially at light load conditions. However, the switched inductor in the secondary side has effectively overcome the resonant converter problem as well as minimizing the circulating current at a nominal point of operation. A secondary switch and inductor added additional costs and losses compared to the converter mentioned in (Xiaodong Li & Bhat, 2010). A 480 W prototype is designed to validate the proposed method. The peak efficiency of 94.6% is reported with the topology and modulation scheme.

In (H. Park et al., 2018), a bidirectional series resonant converter is proposed employing a hybrid of SPS and extended phase shift (EPS) modulation to investigate the ZVS range based on power flow directions. Having an LC resonant tank, the converter includes the magnetizing inductance to design the ZVS conditions in backward power flow. The converter overcomes the problem of ZVS loss under light load conditions by switching between EPS and SPS modulation for forward power flow. The converter fails to provide a wide output voltage range limiting its usage for wide output range applications. The converter is reported to have seamless control during the transition from forward to backward operation or vice-versa. A prototype of 500 W is designed to validate the proposed modulation scheme, and a peak efficiency of around 96% is reported.

Though the SPS modulation is the most prevalent modulation scheme used in isolated converters, it fundamentally is an effective power-centred algorithm and appears to lack flexibility in power control, thereby adding to the stress on the devices used in the converter during continuous operation. Moreover, an efficient SPS can only be operated effectively when the conversion voltage gain is equal to one, and the circuiting power is much larger, and the efficiency is reduced for any mismatch between the voltage amplitudes of primary and secondary of the transformer. The SPS control can, therefore, only operate in a limited operating range under soft switching. These disadvantages inspire the research to improve the phase shift concept to overcome the mentioned problems.

2.2.1.2 Dual Phase Shift Modulation

In the power flow process, there exist time intervals in which reverse (negative) power occurs. In SPS control, the power transfer is dependent on the leakage inductor of the transformer (De Doncker et al., 1991). With the rise in the reverse power flow, the forward power flow increases to compensate for the losses. Consequently, the circulating power and current stress will increase, which results in an increased conduction loss in power MOSFETs and magnetic components and, therefore, decreased efficiency in the converter. To limit the reverse power flow in the converter, the idea of phase shift needs to be extended for different control signals (B. Zhao et al., 2012). In this control scheme, not only there is an outer phase-shift ratio (D2), which is the phase shift between the primary and secondary voltages of the isolation transformer, but also the inner phase-shift ratio (D1) is proposed, which is the phase-shift ratio between the driving signals in each side (Hua Bai & Mi, 2008). Dual phase shift modulation (DPS) extends the flexible range of power transmission and enhances voltage gain regulating flexibility; decreases the reverse power flow, and thereby reducing the conduction losses and enhancing the efficiency.

A zero-circulating current (ZCC) based modulation for isolated bidirectional DAB DC-DC converter is proposed in (Karthikeyan & Gupta, 2016) that employs dual phase shift ratio to eliminate the circulating power flow. The modulation scheme decides the two-phase shift ratios based on falling and the rising edge of the gate signals corresponding to the primary switches and secondary switches. The required condition for falling edge phase ratio is determined to eliminate the circulating power in the converter. The proposed modulation scheme also reduces the current stress on power devices. However, the elimination of circulating power flow is only limited to the output side, and the converter fails to limit the input side circulating power flow. To validate the proposed control strategy, a 200 W prototype is designed with a peak efficiency of 94.2% at 50 V input voltage.

To eliminate the circulating power flow on the input as well as the output side, a front and rear-end switch (FRS)-DAB bidirectional DC-DC converter is proposed in (Karthikeyan & Gupta, 2018). The converter employs DPS modulation for the operation, which results in lower current stress, increased power transfer capability, and extended ZVS range. However, the converter adds two extra switches that, in turn, increase the overall cost of the converter. Moreover, the primary and secondary blocking switches are stressed at a higher voltage and current as compared to DAB switches. A 350 W converter prototype is proposed to substantiate the theoretical results. The maximum efficiency of 96.2% for peak load condition with 8% efficiency improvement under light load condition in comparison to the conventional DAB converter is reported.

Introducing a degree-of-freedom to SPS enables the DPS to increase converter reliability and efficiency, minimize reactive power, and reduce the current stresses through the semiconductor devices. Nevertheless, a couple of DPS-based controllers are developed to improve the efficiency or current stress of isolated resonant converters (B. Zhao, Song, & Liu, 2013b; B. Zhao, Song, Liu, et al., 2013); they still have sub-

suboptimal operating modes and lack a global optimum solution, which is to be investigated.

2.2.1.3 Triple Phase Shift Modulation

In some applications, such as light-load situations, the triple phase-shift (TPS) control strategy that involves three phase shifts has been used to resolve the problem of low efficiency of resonant converters (Wen & Xiao, 2013). The first phase shift is between the primary and the corresponding secondary control switches; the second phase shift is between the diagonal control signals in the primary bridge, and the third is the phase shift between the diagonal control signals in the secondary bridge. The performance improvement in a wide load range is observed by the appropriate selection of operating modes and phase-shift values. In order to increase the ZVS range, triple phase shift adds an additional control variable and reduces the total loss, which increases the efficiency of the converter (Harrye et al., 2014).

In (Pistollato et al., 2019), a triple-phase shift modulation is proposed and analyzed for conventional dual active bridge topology aimed at maximizing the efficiency of the converter. The authors proposed three different approaches to employ TPS for the DAB converter. The modulation schemes are decided based on minimum current constraint with full or partial ZVS condition. The partial ZVS condition is mentioned as the switching region between fully ZVS and hard switching. A 1.5 kW prototype is constructed to validate the proposed modulation approaches with a peak efficiency of 97.1%. The light-load efficiency under TPS sees 11.2% efficiency improvement in comparison to SPS modulation.

A four-degree-of-freedom modulation strategy for DAB series resonant converter employing TPS modulation has been presented in (Muhammad Yaqoob et al., 2019) for loss minimization. The converter employs internal and external phase shifts between the

primary and secondary switches to eliminate the circulating power flow, reduce the RMS resonant tank current and achieve complete ZVS range minimizing the conduction losses and switching losses. The added degree-of-freedom in the modulation strategy makes the closed-loop implementation complex. A 1 kW prototype with a peak efficiency of 97.7% is designed to support the proposed modulation strategy.

2.2.1.4 PWM plus Phase Shift Modulation

A PWM plus phase shift (PPS) modulation varies the duty cycle with the conventional phase shift between the primary and corresponding secondary side switches.

A PWM plus phase-shift control bidirectional converter has been proposed in (D. Xu et al., 2004). In this, the varying duty cycle is employed to match the voltage between input and output, whereas the phase shift is used to control the power flow. The variable duty cycle acts as an electric transformer between the equivalent input voltage and equivalent output voltage, such that both positive and negative amplitudes of input voltage are equal to that of the equivalent output voltage. In comparison to phase shift control, PPS control can reduce the current stresses and RMS currents of the converter. The converter losses are also decreased with an extended ZVS range. However, the converter is failed to ZVS for light-load condition, thereby increasing the switching losses. Moreover, the phase shift ratio, as an added variable, makes the closed-loop controller design complex due to the interaction between the two variables. A 100-W prototype has been designed to validate the analysis with a peak efficiency of 94% at 24V output.

A decoupled PPS modulation for a dual half-bridge bidirectional DC-DC converter for energy storage system has been mentioned in (Xiangli et al., 2018). The decoupled control proposed two independent control freedoms- the duty cycle to control voltage gain and phase shift to control power flow, expanding the input voltage range. Additionally, the limited leakage inductor current reduces the current stress of the switches. A small-signal

model is derived to design a closed-loop controller to operate under light load conditions. The modulation strategy is more suitable for energy storage systems due to the discharge depth of the batteries. A peak efficiency of 94.8% is observed for the designed 200-W prototype converter.

2.2.2 Pulse Width and Amplitude Modulation

A bi-directional three-level LLC resonant converter is designed in (Jiang et al., 2016) with a constant frequency pulse width and amplitude modulation (PWAM). The converter has three operating modes, and to maintain a wide voltage gain range, it switches between these modes of operation. As seen, the ZVS and the voltage stress across the power switches depend on the voltage gain; hence ZVS only occurs in the primary switches. An extra flying capacitor and auxiliary switches are used in the topology, making the operation of the converter complicated and increasing the cost of the converter. Finally, to validate the theoretical study, a 1kW prototype is developed. With full load conditions, the maximum efficiency of 96.5% is achieved.

2.2.3 Fixed-Frequency Pulse Width Modulation

In fixed-frequency pulse width modulation, the voltage gain of the resonant tank is mainly controlled by varying the duty cycle keeping the switching frequency constant. Most commonly, this frequency is the same as that of the resonant frequency of the resonant converter to achieve maximum power transfer from input to output side (Rathore et al., 2016; X. Sun et al., 2017; Wu, Sun, et al., 2017).

A non-isolated bi-directional current-fed LCL resonant DC-DC converter based on fixed frequency varying duty cycle control is introduced in (Rathore et al., 2016) for the DC microgrid application. Owing to higher voltage conversion ratios, reduced magnetic bulk, and compact size, the converter exhibits superiority over the isolated counterpart. Although there was no such justification in the paper, the voltage gain range should be

constrained by the large circulating current for large duty ratios. At light load conditions, one of the switches fails to achieve ZVS, causing high switching losses and degrading the light-load efficiency of the converter. A 350 W rated converter is designed with a peak efficiency of 95.5% under boost mode and 95% under buck mode of operation.

A fixed-frequency PWM controlled bidirectional current-fed series resonant converter has been presented in (Wu, Sun, et al., 2017) for electric vehicle systems. The converter is derived using the integration of current-fed bidirectional buck/boost converter and DAB LC resonant converter. The converter consists of an extra auxiliary inductor on the primary side to achieve ZVS in the primary switches. The magnetizing inductance on the secondary side aid in achieving ZVS in the secondary switches. The voltage gain of the converter is purely dependent on the duty cycle control. Although the PWM control is simple and easy to implement, the auxiliary inductor increases the cost with limited gain achievability. A 1.6 kW prototype is built based on the theoretical results, and the peak conversion efficiency of 97% is achieved.

In (X. Sun et al., 2017), a dual bridge LLC resonant converter employing constant frequency PWM is presented. The topology is an integration of half-bridge and full-bridge LLC circuit. The employed constant frequency PWM achieves voltage gain independent of the quality factor and minimal effect of magnetizing inductance. This helps in simpler parameter design considerations. The converter includes an extra bidirectional power switch in the primary that is operated under hard switching conditions. Moreover, all the power switches suffer from high turn-off currents leading to an increased turn-off loss. A maximum efficiency of 96.5% is achieved at 150 W for the design 480 W, 24V/20A prototype.

A two-phase secondary-side interleaved PWM LLC resonant converter has been presented in (Z. Li et al., 2019) for medium/high power applications in electric vehicle charging. The converter employs a simple PWM control with a constant frequency. The primary bridge switches are switched at a 50% duty cycle in a complementary manner. The two-phase secondary is interleaved with two power switches and six power diodes. The secondary switches are PWM controlled. The converter exhibits optimum ZVS characteristics for wide output voltage and load ranges. The interleaving technique reduces the primary switch turn-off current, thereby reducing the switching losses. The dynamic performance of the converter is suffered due to PWM control. The topology employs an increased count of power switches and diodes. A 1.3 kW prototype has been designed with a peak efficiency of 97.3% at full load conditions.

2.2.4 Pulse Frequency Modulation

The variable frequency control is also known as the Pulse frequency modulation (PFM) control scheme that is the most widely used method for a resonant converter. This control is performed by varying the switching frequency (f_s) with respect to the resonant frequency (f_r). The output voltage of the converter is compared with the reference, and the error voltage (V_{err}) is feed to the PI controller. Finally, the following block generates the switching pulses using the calculated switching frequency generated by the PI controller.

In (Wei et al., 2010), a bi-directional CLLC type converter is reported for the uninterrupted power supply system. The conventional PFM with two current sensors is used to control the power flow and gate pulses. It is not stated clearly how the extra capacitor with LLC resonant tank has become advantageous in BDC and how the asymmetric CLLC network would work in the reverse direction. Like unidirectional LLC resonant converter, wide frequency variation is required to achieve the desired voltage

gain, which increased the size of the magnetics in the converter. The forward efficiency is degraded at minimum input and light load conditions due to the high circulating current flowing for a long time in the converter.

A bi-directional CLLC type resonant converter (Jung et al., 2013) is designed for a low voltage direct current power distribution system. This converter is similar to the one presented by (Wei et al., 2010). An extra inductor is used to make the converter symmetrical for both forward and backward power flow directions. The proposed converter has combined three control techniques associated with PFM: a Dead band control for deciding power flow directions, a switch control for power flow transitions, and a soft-start control for reducing electrical stresses in the converter devices. Nevertheless, the converter still has high turn-off switching losses and conduction losses due to wide frequency variation under wide input voltage. A 5kW prototype has been designed to validate the concept. The highest efficiency of 97.8% is achieved at 4kW.

In (Zahid, Dalala, Chen, Chen, & Lai, 2015), a detailed design procedure is represented for a bi-directional CLLLC type resonant converter for a battery charging application. This converter is similar to LLC type resonant converter except an extra inductor and capacitor used on the secondary side. The structure becomes symmetrical with the CLLLC tank, but the voltage gain characteristics for both BCM (battery charging mode) and RM (regeneration mode) are different for all loads and switching frequency variations. Simple PFM has been implemented in this converter to regulate the output voltage, while there was no other control associated with PFM for the automatic transition between BCM to RM or vice versa. The circulating current still exists for a longer time period at minimum input voltage condition, which hinders the efficiency of this converter. To achieved maximum voltage gain, the magnetizing inductance is designed to a very low value, which is responsible for the high magnetizing current resulting in huge

conduction losses, increased apparent power requirements for switches, and also increased peak voltage requirements for the primary side capacitor.

A bi-directional DAB LLC type resonant converter for energy storage systems is proposed in (Tianyang et al., 2015). To make the topology symmetrical in any operating mode, an extra inductor is added, which increases the power loss and cost for the system. A new variable frequency control scheme has been proposed where the power flow direction and output power of the bi-directional LLCL converter can be changed automatically and continuously. According to this control, the converter is always operated below the resonance frequency and having the same frequency as all switches, but the pulse width of gate drive signals for primary and secondary switches are different based on the voltage gain. The voltage gain is still limited to maintain high conversion efficiency; otherwise, reverse energy will be increased with switching frequency variation to achieve a high gain range. The converter is like a unidirectional LLCL converter with a diode rectifier when the gain more than unity and ZVS can be maintained up to parallel resonance frequency for both forward and backward power flow. On the other hand, the converter becomes out of ZVS, especially at a forward mode when the gain lower than unity. This converter is validated with a 1kW prototype and has a maximum efficiency of approximately 96% at full load conditions. The measured efficiency in forward operation is lower compared to conventional LLC converter with diode rectifier due to high switching and conduction losses at gain 0.8. However, the efficiency is approximately 5% greater than conventional DAB converter over most of the load and designed DC-link voltage conditions.

Pulse frequency modulation for resonance converter is advantageous in terms of wider soft-switching range and voltage regulation while it requires extra control circuitry for the bi-directional power flow applications.

2.3 Comparison of Selected Resonant Converter Topologies

The resonant converters have various ranges and characteristics of soft switching due to variations in resonant tank parameters and control strategies. The CLLC and CLLLC have wider voltage gain and soft-switching range compared to the LLC resonant converter, while additional components in the resonance tank increase both size and cost. Moreover, PFM resonant converters with CLLC and CLLLC need an additional control scheme for an automatic transition between forward to backward power flow operation. In comparison, the asymmetric CLLC resonant converter shows different behaviour from the symmetric resonant converter in forward and backward power flow directions. In contrast, the modulation scheme with phase shifts have a faster bi-directional transition but exhibit narrow voltage gain and ZVS range. The phase-shifted resonant LLC converter can secure ZVS for primary as well as secondary power devices in comparison with other resonant converters. The two other types: LCL and LCC, are equally efficient but have a narrow voltage gain and a soft-switching range. PFM has advantages in terms of efficiency and voltage power over constant frequency phase-shift modulation schemes.

A comparison of the selected resonant converter topologies employing a range of modulation schemes has been summarized in Table 2.2. The table presents an overview based on the selected resonant tank, ZVS range, modulation scheme, voltage gain range, and the ability to limit the circulating power flow in the resonant converters.

Table 2.2 A Comparison of Isolated Resonant Converter Topologies and Modulation Schemes

Topology	Modulation Scheme	Soft switching range	Voltage gain range	Circulating power flow control	Maximum Efficiency
LLC type resonant converter (Xiaodong, 2014)	SPS	Narrow	Unity gain	No	94.5% (300 W)
LC type tunable resonant tank (M. Yaqoob et al., 2017)	SPS	Wide	Wide	No	94.6% (480 W)
LC series resonant converter (H. Park et al., 2018)	SPS+EPS	Wide	Narrow	No	96% (500 W)
ZCC based resonant converter (Karthikeyan & Gupta, 2016)	ZCC modulation	Narrow	Narrow	Yes	94.2% (200 W)
FRS-DAB converter (Karthikeyan & Gupta, 2018)	DPS	Wide	Narrow	Yes	96.2% (350 W)
DAB resonant converter (Pistollato et al., 2019)	TPS	Wide	Medium	Yes	97.1% (1.5 kW)
LC-type resonant converter (Muhammad Yaqoob et al., 2019)	TPS+ frequency variation	Wide	Narrow	Yes	97.7% (1 kW)
CLLC type asymmetric resonant, (Wei et al., 2010)	PFM	Wide	Wide	No	96% (300 W)

Table 2.2 Continued

Topology	Modulation Scheme	Soft switching range	Voltage gain range	Circulating power flow control	Maximum Efficiency
CLLLC type Symmetric resonant (Zahid et al., 2015)	PFM	Wide	Wide	No	97.7% (3.15 kW)
LLC type (Tianyang et al., 2016)	PWAM	Wide	Wide	No	96% (1 kW)
LCL type Resonant (Rathore et al., 2016)	FF-PWM	Narrow	Wide	No	95% (350 W)
CLTC type resonant converter (C.-S. Wang et al., 2019)	PFM	Wide	Wide	No	96% (2.5 kW)

2.4 Summary

This chapter discussed the topological configurations that have been proposed to operate in terms of their interface voltage levels as well as a maximum power output. Among all the topologies, dual active bridge topology is most suitable for desired power ratings. However, for the dual phase, the integrated FB would result in larger switch counts encouraging in proposed dual phase modified FB as a topological structure having lower voltage stresses on the switches.

The phase shift, as well as frequency modulation schemes, which are employed in previous studies, have been critically reviewed, and their advantages, disadvantages, and control complexity have been discussed. Based on the described modulation schemes,

single-phase shift modulation having variable frequency selection would exhibit simpler control, wider load range operation, and smooth transition in bidirectional power flow applications. The following chapter discusses the proposed dual phase LLC resonant DC-DC converter with variable frequency phase shift modulation and its steady-state operation in terms of different control variables.

CHAPTER 3: PROPOSED LLC RESONANT CONVERTER TOPOLOGY

3.1 Introduction

This chapter discusses the proposed dual-phase LLC resonant converter topology and its equivalent circuit model. The operation of the proposed converter has been explained based on the phase-shifted secondary switches modulation. The proposed LLC converter employs a Fundamental Harmonic Approximation (FHA) for the steady-state analysis. The characteristics of the proposed converter, like voltage gain, voltage, and current stresses of power devices, have been discussed further. The soft switching operations of the proposed converter in which ZVS constraints for primary as well as secondary switches have been mentioned. Lastly, the reverse power flow in the proposed converter has been discussed.

3.2 Proposed Dual Phase LLC Resonant Converter

The circuit configuration of the proposed dual phase LLC resonant DC-DC converter for a wide input voltage range is shown in Figure 3.1. It consists of a high voltage side (HVS) and a low voltage side (LVS) as in the primary and secondary side of the high-frequency transformer. The output can be a DC voltage source like an energy storage system for getting bi-directional power flow or a resistive load with a capacitive filter for getting unidirectional power flow only. With the aim of wide input voltage range and zero reverse power flow (RPF) in the proposed converter, two LLC resonant tanks are series-connected on HVS of modified Full-bridge (FB) converter. The transformer leakage inductance is used with an extra inductor to constitute each LLC resonant tank. The series resonance capacitor filters out the DC component from any reverse current that might hamper the saturation of the transformer (Steigerwald, 1988). Both tanks have the same resonant parameters, i.e. $L_{r1} = L_{r2} = 0.5L_r$, $C_{r1} = C_{r2} = 2C_r$, $L_{m1} = L_{m2} = 0.5L_m$ and $n_1 = n_2$.

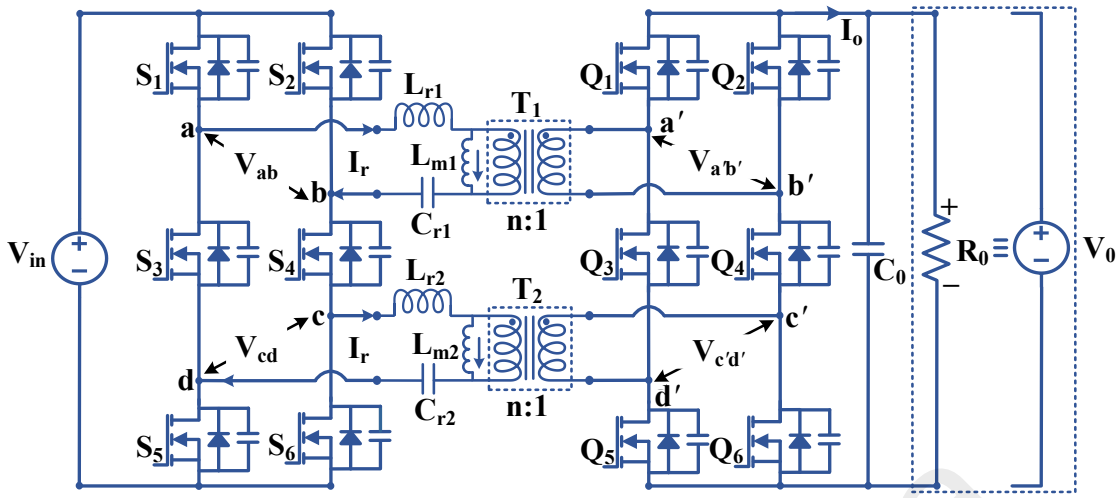

Figure 3.1: Proposed Dual Phase LLC Resonant Converter

The transformers T_1 and T_2 are series-connected on both sides. Hence, the current flowing through the windings are always equal, resulting in equal power distribution between the transformers. Moreover, the transformer has to be designed in such a manner to have a suitable value of magnetizing inductance in order to have reduced conduction losses and increased ZVS range in the converter. The output capacitor, C_o, is large enough to filter out the voltage ripples. The switching frequency for the converter is chosen to be larger than the main resonant frequency as the converter always operates in continuous conduction mode. The switching cycle and key operation waveforms is depicted in Figure 3.2. The power flow and voltage regulation are decided by the phase shift angle between primary and secondary switches and the duty cycle of the secondary switches, as discussed in detail later.

3.3 Modes of Operation

The proposed converter operation is symmetrical for the forward and backward direction of power flow. Hence, the forward power flow is elaborated in the subsequent part of the thesis. There is a total of 16 operation stages of the proposed double LLC resonant converter for one switching cycle. The stages from t_0-t_8 are introduced and elaborated with the detailed corresponding equivalents circuits for every half-switching cycle.

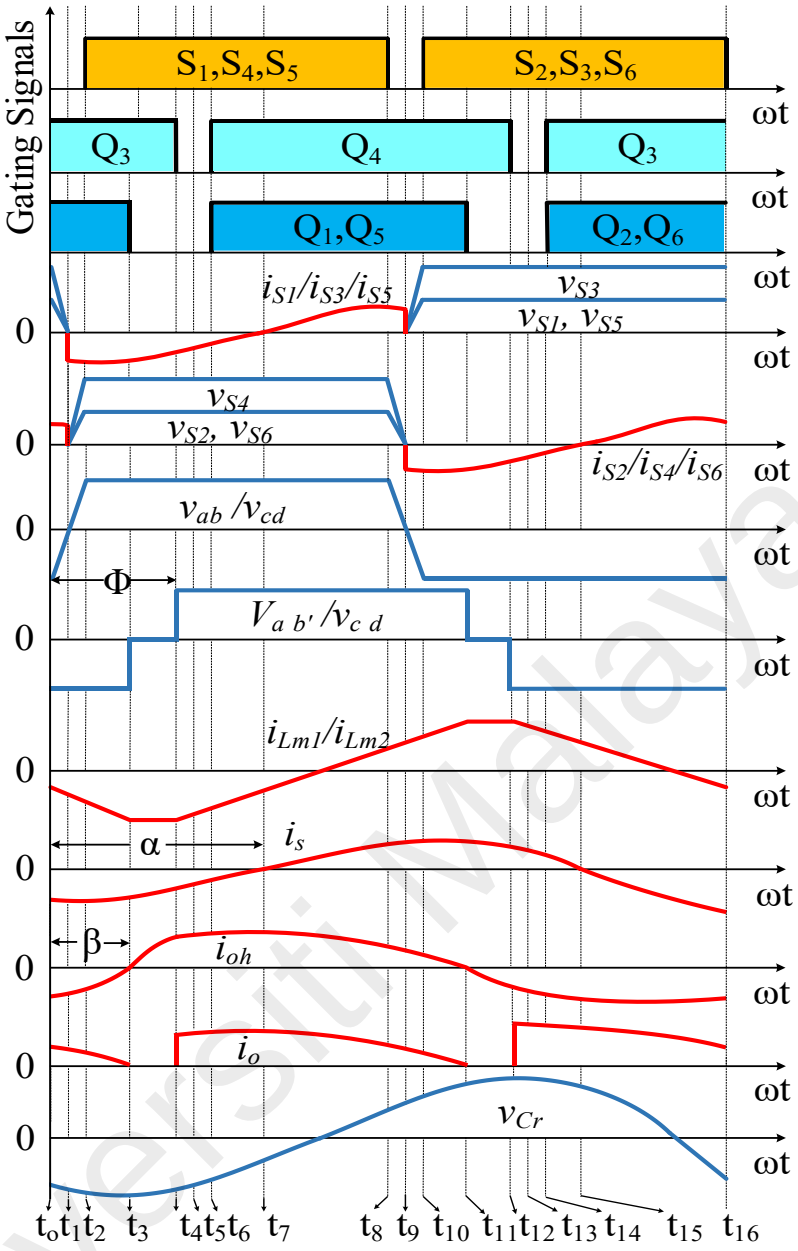

Figure 3.2 Key operation waveforms of the proposed dual phase LLC resonant converter

Stage 1 (t_0-t_1): This mode (Figure 3.3) starts ($t=t_o$) when the gate pulses to switches S_2, S_3, and S_6 are removed. Then, the free-wheeling mode starts. The lossless snubbing capacitors C_{oss2}, C_{oss3}, and C_{oss6}, are getting started to charge by the resonant current Ir. Consequently, the capacitor voltages V_{S2} and V_{S6} increase slowly from zero to $V_{in}/2$ and V_{S3} to V_{in}. Alternatively, the body capacitors of switches S_1, S_5, and S_4 are discharged, which results in a gradual decrease of their voltages from $V_{in}/2$ and V_{in} to zero, respectively. The voltage across each resonant tank increases to $V_{in}/2$. The switches S_2,

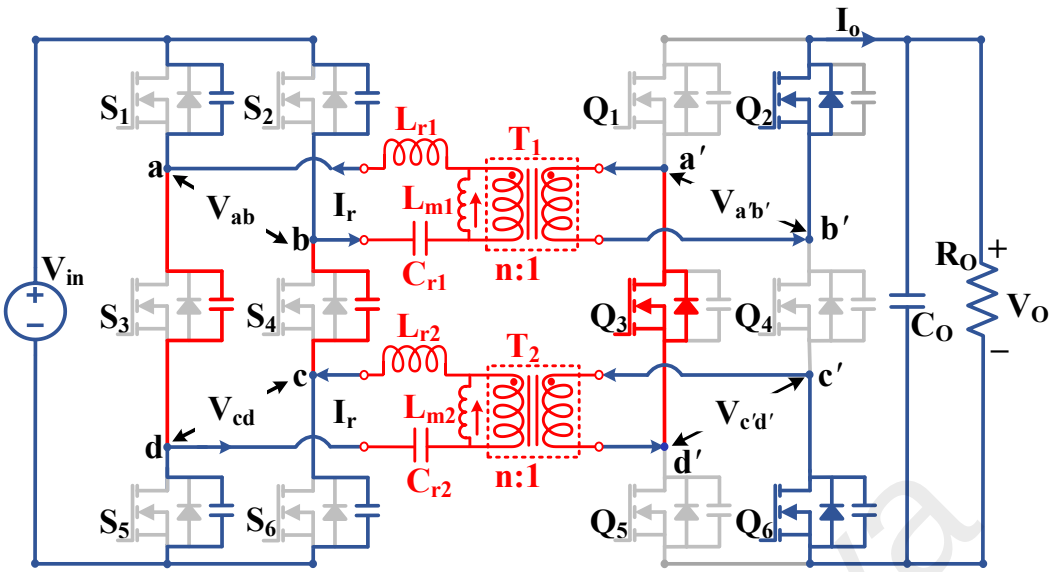

Figure 3.3 Operation in forward mode during stage 1 ($t_0 \sim t_1$)

S_3, and S_6 turn off with the ZVS transition. This stage ends when the charging capacitors are fully charged and vice-versa. Equation 3.1 expresses transient-state for stage 1.

$$\begin{cases} v_{S_1}(t) = v_{S_5}(t) = \dfrac{V_{in}}{2} - \dfrac{C_r}{C_{oss\_S}}\left(v_{cr}(t) - v_{cr}(t_0)\right) \\ v_{S_3}(t) = \dfrac{2C_r}{C_{oss'\_S}}\left(v_{cr}(t) - v_{cr}(t_0)\right) \\ v_{S_2}(t) = v_{S_6}(t) = \dfrac{C_r}{C_{oss\_S}}\left(v_{cr}(t) - v_{cr}(t_0)\right) \\ v_{S_4}(t) = V_{in} - \dfrac{2C_r}{C_{oss'\_S}}\left(v_{cr}(t) - v_{cr}(t_0)\right) \end{cases} \tag{3.1}$$

Stage 2 (t_1-t_2): As V_{S1}, V_{S4} and V_{S5} are equal to zero, the body capacitors are fully discharged. Mode 2 (Figure 3.4) begins at this state. With the short-circuited switching state, the antiparallel diodes of switches start to conduct and become forward biased. Hence, the tank power is pumped back into the HVS with the negative resonant current flowing through D_{S1}, D_{S4}, and D_{S5}. The secondary current flows into the load through Q_2, Q_3, and Q_6. This stage ends when turn on signals are given to S_1, S_4, and S_5. The transient-state equations are mentioned in Equation 3.2.

$$\begin{cases} i_{S_1}(t) = i_{S_4}(t) = i_{S_5}(t) = C_r \dfrac{d}{dt} u_{C_r}(t), i_{S_2}(t) = i_{S_3}(t) = i_{S_6}(t) = 0 \\ v_{S_1}(t) = v_{S_4}(t) = v_{S_5}(t) = 0, v_{S_2}(t) = v_{S_6}(t) = \dfrac{V_{in}}{2}, v_{S_3}(t) = V_{in} \end{cases} \tag{3.2}$$

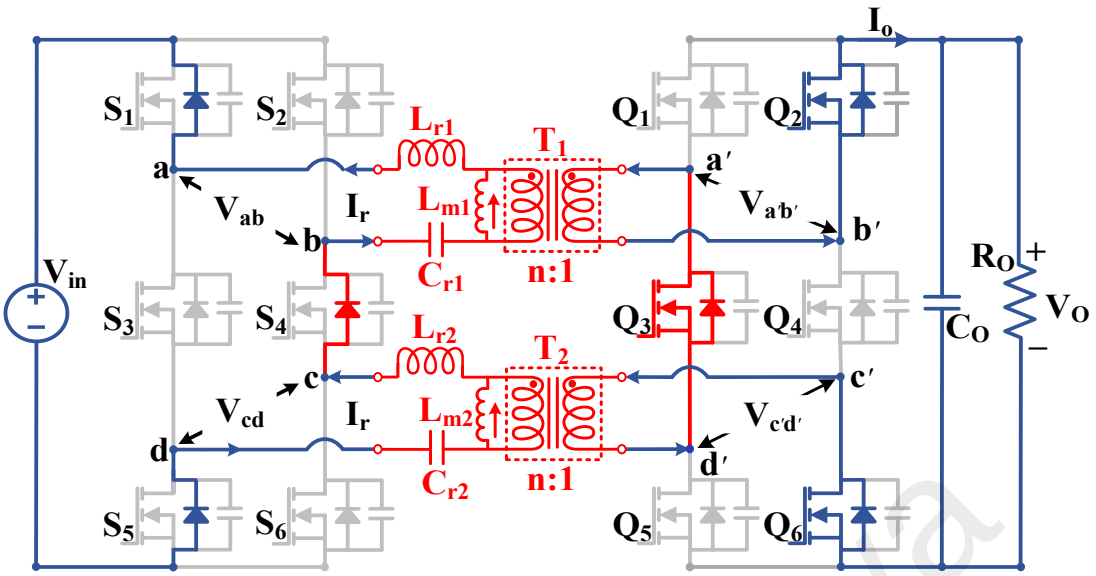

Figure 3.4 Operation in forward mode during stage 2 ($t_1 \sim t_2$)

Stage 3 (t_2-t_3): The triggering signals are provided to S_1, S_4, and S_5, while D_{S1}, D_{S4}, and D_{S5} are still conducting. Figure 3.5 depicts the stage 3 of the operation. The transformer current becomes zero at the end of this interval as the pump back power into the source finishes. Moreover, the resonant current flows towards zero. Accordingly, zero voltage and zero current switching turn on can be achieved for S_1, S_4, and S_5. The output current becomes zero at the end of this stage. Stage 3 transient-state is expressed in Equation 3.3.

$$\begin{cases} C_{r_1}\dfrac{d}{dt}u_{C_r}(t) = i_{L_{r_1}}(t) = i_{L_{m_1}}(t) + i_{oh}(t) \\ L_{r_1}\dfrac{d}{dt}i_{L_{r1}}(t) = V_{ab} - u_{C_{r1}}(t) - n\cdot v_{ab'}(t) \\ L_{m_1}\dfrac{d}{dt}(-i_{L_{m_1}}(t)) = n\cdot v_{ab'}(t) \\ v_{ab'}(t) = -\dfrac{V_{oh}}{2} \end{cases} \tag{3.3}$$

Stage 4 (t_3-t_4): At the start of this interval (as shown in Figure 3.6), the transformer current I_{t1}=I_{t2} reaches zero and starts to rise in a positive direction. The secondary current tries to flow in a negative direction, but the improved modulation scheme with the six-switch configuration results in ZCS turn-on of Q_3 that short circuits the transformer secondary with the body diode of already conducting Q_4. It is hence inhibiting the output current in

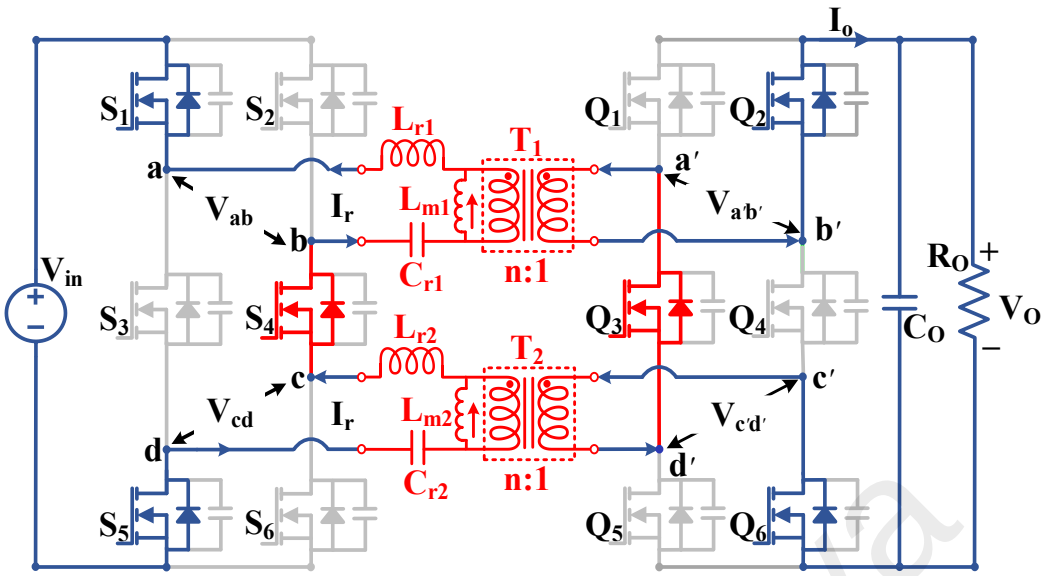

Figure 3.5 Operation in forward mode during stage 3 ($t_2 \sim t_3$)

the reverse direction. Thus, there is no reverse power during this interval, thereby having the advantage of reduced conduction losses. In this mode, the current is discontinuous. This interval ends when Q_3 is turned OFF. Moreover, the clamped zero voltage at L_m results in the constant magnetizing current (i_{Lm}) in the transformer. The same has been demonstrated as in transient-state equations for stage 4 in Equation 3.4.

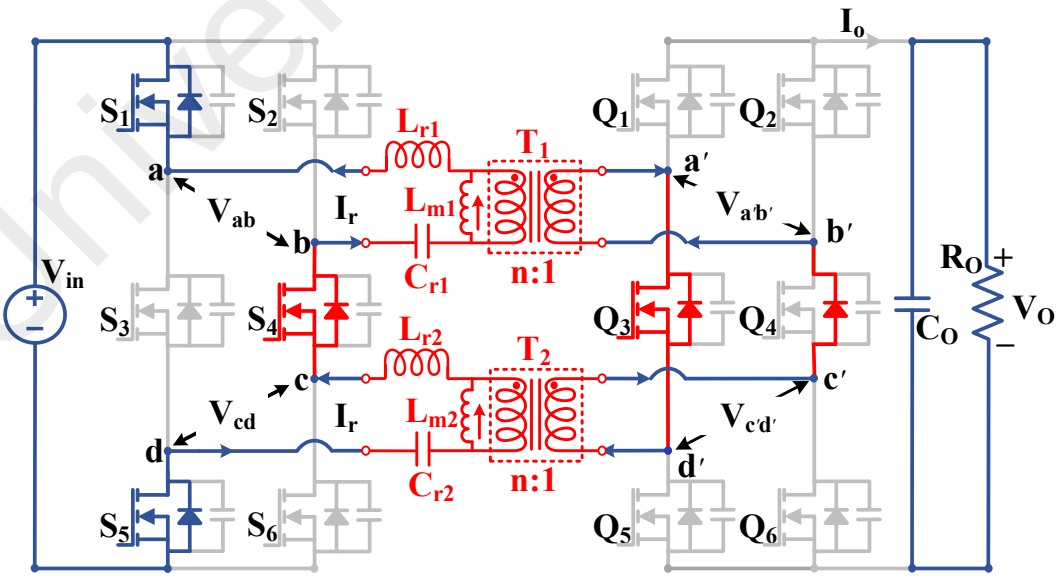

Figure 3.6 Operation in forward mode during stage 4 ($t_3 \sim t_4$)

$$\begin{cases} C_{r_1}\dfrac{d}{dt}u_{C_r}(\mathrm{t}) = i_{L_{r_1}}(\mathrm{t}) = i_{L_{m_1}}(\mathrm{t}) + i_{oh}(\mathrm{t}) \\ L_{r_1}\dfrac{d}{dt}i_{L_{r1}}(\mathrm{t}) = V_{ab} - u_{C_{r1}}(\mathrm{t}) - n\cdot v_{ab'}(\mathrm{t}) \\ L_{m_1}\dfrac{d}{dt}(-i_{L_{m_1}}(\mathrm{t})) = 0 \text{ i.e. } i_{L_m} = \text{constant} \\ v_{ab'}(\mathrm{t}) = 0 \end{cases} \tag{3.4}$$

Stage 5 (t_4-t_5): Figure 3.7 depicts the stage 5 of the operation. The secondary current through the series-connected windings of both the transformer starts to flow in the positive direction after Q_3 and D_{Q4} are turn off. The positive current flows to load. On the HVS, S_1, S_4 and S_5 are conducting. On the secondary side, the lossless snubbing capacitors of Q_1, Q_4, and Q_5 discharge and Q_2, Q_3, and Q_6 are charged by the positive secondary current, which results in ZVS turn off for three switches. The positive voltage across secondary is reflected back to the HV side, resulting in an increase in magnetizing current of both transformers in the positive direction. Equation 3.5 demonstrates the transient-state of the converter during this stage.

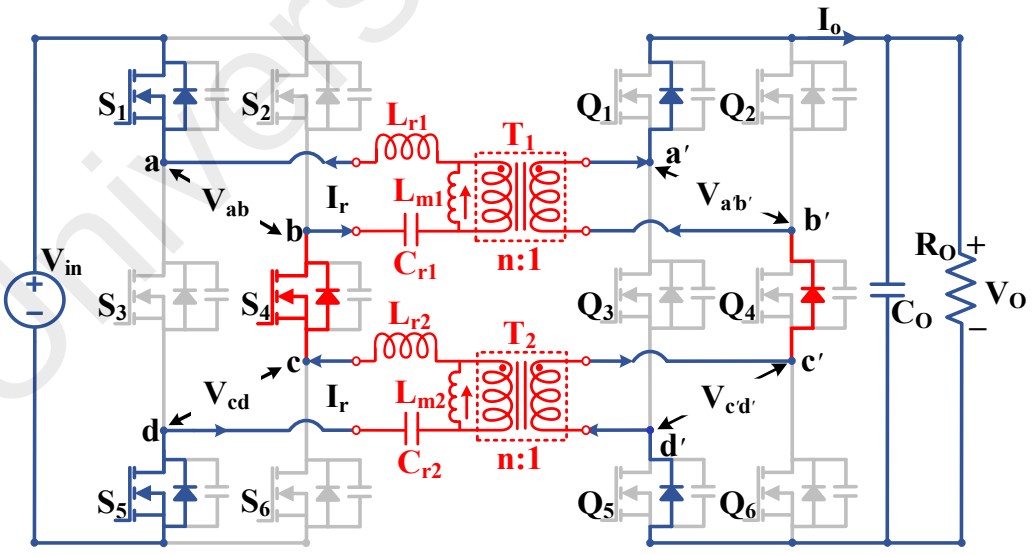

Figure 3.7 Operation in forward mode during stage 5 ($t_4 \sim t_5$)

$$\begin{cases} v_{Q_1}(t) = v_{Q_5}(t) = \dfrac{V_{in}}{2} - \dfrac{C_r}{C_{oss\_Q}}\left(v'_{C_r}(t) - v'_{C_r}(t_4)\right) \\ v_{Q_3}(t) = \dfrac{2C_r}{C_{oss'\_Q}}\left(v'_{cr}(t) - v'_{cr}(t_4)\right) \\ v_{Q_2}(t) = v_{Q_6}(t) = \dfrac{C_r}{C_{oss\_Q}}\left(v'_{cr}(t) - v'_{cr}(t_4)\right) \\ v_{Q_4}(t) = V_{in} - \dfrac{2C_r}{C_{oss'\_Q}}\left(v'_{cr}(t) - v'_{cr}(t_4)\right) \end{cases} \tag{3.5}$$

Stage 6 (t_5-t_6): This interval begins when the body capacitors of C_{Q1}, C_{Q4}, and C_{Q5} are discharged completely to zero voltage. Figure 3.8 depicts the stage 6 operation of the converter. The body diode D_{Q1}, D_{Q4}, and D_{Q5} are conducting and remain in forward bias until the end of this interval when the trigger pulses are given. The secondary output current is positive during the interval. The transient-state is expressed in Equation 3.6 during this stage.

$$\begin{cases} i_{Q_1}(t) = i_{Q_4}(t) = i_{Q_5}(t) = C_r \dfrac{d}{dt} u'_{C_r}(t), i_{Q_2}(t) = i_{Q_3}(t) = i_{Q_6}(t) = 0 \\ v_{Q_1}(t) = v_{Q_4}(t) = v_{Q_5}(t) = 0, v_{Q_2}(t) = v_{Q_6}(t) = \dfrac{V_{in}}{2}, v_{Q_3}(t) = V_{in} \end{cases} \tag{3.6}$$

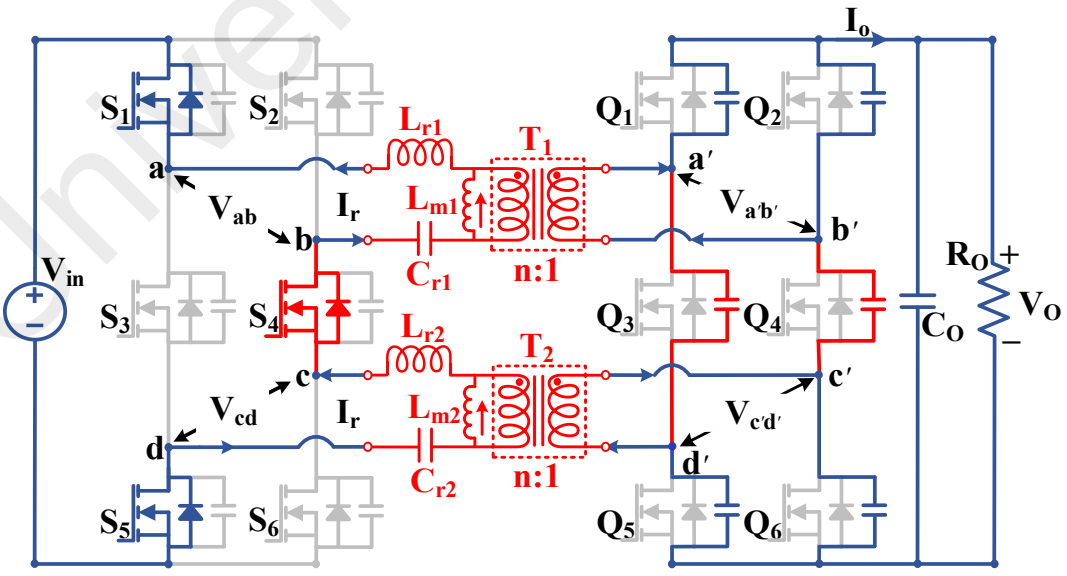

Figure 3.8 Operation in forward mode during stage 6 ($t_5 \sim t_6$)

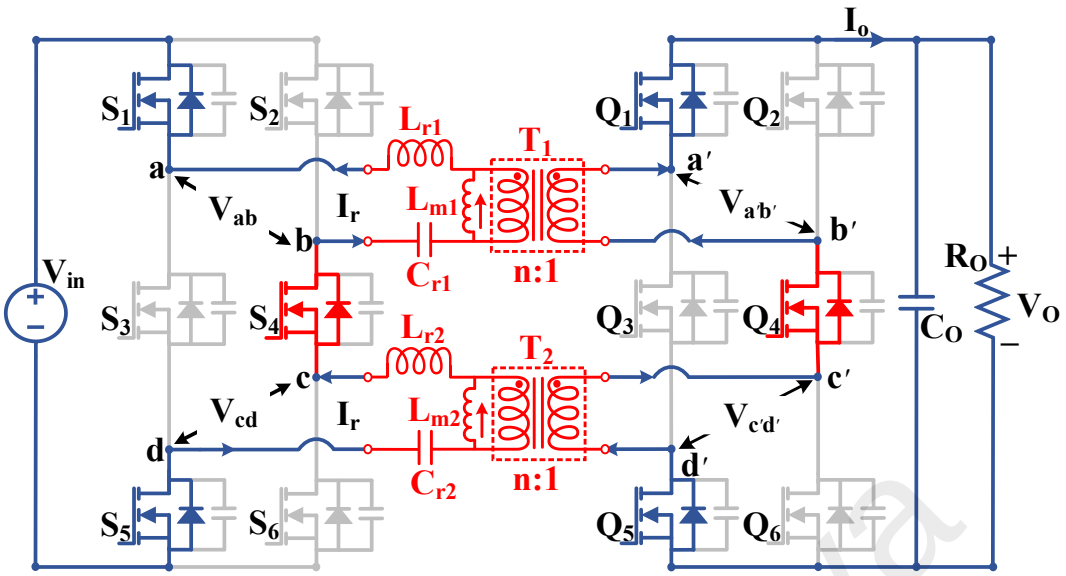

Figure 3.9 Operation in forward mode during stage 7 ($t_6 \sim t_7$)

Stage 7 (t_6-t_7): This stage as shown in Figure 3.9 starts with ZVZCS turn-on of Q_1, Q_4, and Q_5. The forward power transfer from source to load takes place. The resonant current, $I_{r1}=I_{r2}$, goes towards positive through zero. The interval ends at the instant when $I_{r1}=I_{r2}$ becomes zero. The current flows through switches instead of diodes.

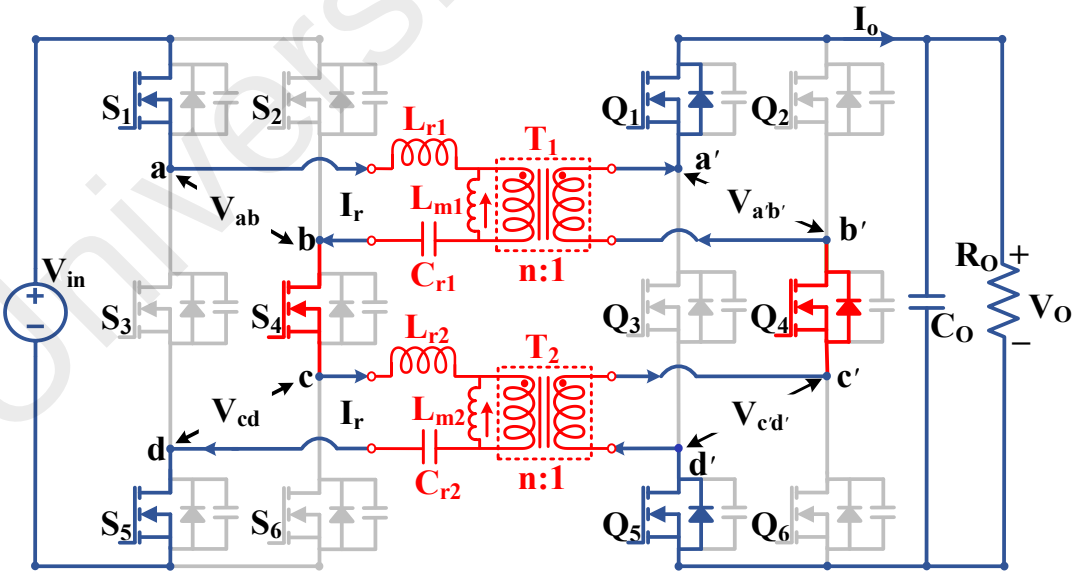

Figure 3.10 Operation in forward mode during stage 8 ($t_7 \sim t_8$)

Stage 8 (t_7-t_8): During this interval, the converter operates with positive power flow from HVS to LVS through the resonant tank and the transformers. The resonant waveforms change to a sine-waveform. Moreover, the magnetizing current i_{Lm} is increased through

zero up to i_{Lm1}. The stage ends when S_1, S_4, and S_5 are turned off and are starting to go under dead-time operation.

3.4 Steady-State Analysis

The time-domain analysis involves solving a set of differential equations in continuous time intervals in any high-frequency period. The behavioral equations of the steady-state provide accurate results but at the cost of calculation complexity. With the increased reactive component counts in the resonant tank, the resulting high-order differential equations would be quite complex, and the analytical inference drawn using the closed-form would be impossible. The frequency-domain analysis proposes the analytical formulas for variables like voltage gain and current/voltage stresses, thereby reducing the calculate ions. Nonetheless, the conventional FHA results are not very acceptable when the converter operates under critical conduction mode. Hence, a modified FHA analytical model is employed to improve the accuracy of the conventional FHA method. The same will be used to determine the voltage gain and current/voltage stresses. The proposed bidirectional converter has a similar operation in forward and backward power flow. The power is transferred from the input side to the load side with the help of resonant tank components L_r (sum of L_{ext} and transformer leakage inductor), C_r, L_m , and the phase shift (φ) angle between the HV bridge and LV bridge.

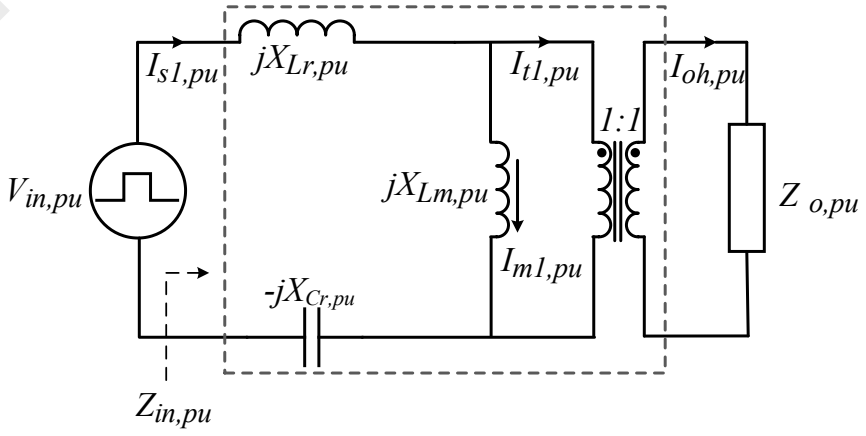

Figure 3.11 Phasor domain equivalent two-port circuit of the proposed converter

The current through the resonant components is nearly sinusoidal (Figure 3.1). The approximate sinusoidal resonant current allows the FHA for DC analysis of the converter, which emphasizes that the fundamental component of any square wave is majorly responsible for power transfer to the load. The ac-equivalent circuits for both resonant tanks are identical and given as an ac-equivalent two-port model, as shown in Figure 3.11. For the sake of analysis simplification, some assumptions are made, which are as follows. All the switches, inductors, capacitors, and high-frequency transformers are ideal and lossless. Moreover, there is no effect of the snubber circuit and dead gap. The LV side parameters are transferred to the HV side and are denoted by a superscript (’). To begin with, for the sake of calculation simplification, all the parameters are normalized using the following base quantities and expressed in Equation 3.7 as :

$$\begin{cases} V_{base} = V_H \\ Z_{base} = \sqrt{\dfrac{L_r}{C_r}} = \omega_r L_r = \dfrac{1}{\omega_r C_r} \\ \omega_B = \omega_r = \dfrac{1}{\sqrt{L_r C_r}} \\ I_{base} = \dfrac{V_{base}}{Z_{base}} \end{cases} \tag{3.7}$$

where ω_r is the series resonant frequency. The switching frequency in per unit or the normalized switching frequency is defined as,

$$F = \frac{\omega_s}{\omega_r} \tag{3.8}$$

where $\omega_s = 2\pi f_s$ and f_s is the switching frequency.

With the objective of achieving ZVS/ZCZVS for primary as well as secondary switches, the converter is operated in the inductive region of the gain curve, keeping the switching frequency always greater than the resonant frequency.

The per-unit reactance values in the resonant circuit are

$$X_{Lr,pu} = F, X_{Cr,pu} = \frac{1}{F}, X_{Lm,pu} = \frac{F}{k} \tag{3.9}$$

where $k = \frac{L_r}{L_m}$ is the series-parallel inductance ratio in LLC resonant tank. The per-unit fundamental input voltage on the primary side is given as

$$v_{in,pu}(\mathrm{t}) = \sqrt{2}V_{in,\mathrm{rpu}} \sin(\omega_s \mathrm{t}) = \frac{4}{\pi}\sin(\omega_s \mathrm{t}) \tag{3.10}$$

where $V_{in,\mathrm{rpu}} = \sqrt{8}/\pi$ is the per-unit fundamental RMS voltage of v_{in}. As discussed earlier, the output voltage of the resonant tank at the HF transformer is a quasi-square wave voltage whose fundamental value is

$$v_{oh}(\mathrm{t}) = \sqrt{2}V_{\mathrm{oh,rms}} \cos\frac{\theta}{2}\sin(\omega_s \mathrm{t} - \phi) \tag{3.11}$$

The per-unit fundamental voltage is given as

$$\begin{cases} v_{oh,pu}(\mathrm{t}) = \sqrt{2}V_{\mathrm{oh,rpu}} \cos\frac{\theta}{2}\sin(\omega_s \mathrm{t} - \phi) \\ = \frac{4M}{\pi}\cos\frac{\theta}{2}\sin(\omega_s \mathrm{t} - \phi) \end{cases} \tag{3.12}$$

where $V_{\mathrm{oh,rpu}} = \sqrt{8}M/\pi$ is the per-unit fundamental RMS resonant tank output voltage, ϕ is the controlled phase-shift angle between the input voltage and resonant tank output voltage, θ is another controlled angle for secondary side switches, M is converter voltage gain given as

$$M = \frac{V'_{ol}}{V_{base}} = \frac{nV_{ol}}{V_H} \tag{3.13}$$

For calculation of $\underline{I}_s$, time-domain equations can be written in phasor form (easy to write as equivalent circuit consists of two sources parted by a reactance $j(\mathrm{F}-1/F)$, and then, reverting to the time domain, we get

$$i_{s,pu}(\mathrm{t}) = \frac{4F}{\pi(\mathrm{F}^2-1)}\left(\sin(\omega_s\,\mathrm{t}-90) - M\cos\theta/2\sin(\omega_s\,\mathrm{t}-\phi-90)\right) \tag{3.14}$$

The per-unit fundamental resonant current $i_{s,pu}(\mathrm{t})$ can also be written as,

$$i_{s,pu}(\mathrm{t}) = \sqrt{2}I_{s,rpu}\sin(\omega_s\,\mathrm{t}-\alpha) \tag{3.15}$$

where $I_{s,rpu}$ is the per-unit fundamental resonant RMS current given as below, α is the phase angle of the input impedance or with respect to $v_{in,pu}(\mathrm{t})$.

$$I_{s,rpu} = \frac{2\sqrt{2}F}{\pi(\mathrm{F}^2-1)}\sqrt{1+M^2\cos^2\frac{\theta}{2}-2M\cos\phi\cos\theta/2} \tag{3.16}$$

$$\alpha = \arctan\left(\cot\phi - \frac{1}{M\sin\phi\cos\theta/2}\right) \tag{3.17}$$

Using (3.16), the per-unit input current can be found as,

$$I_{in,pu} = \frac{\sqrt{2}}{\pi}I_{s,rpu}\cos\alpha \tag{3.18}$$

Moreover, the per-unit input DC power is given as,

$$P_{in,pu} = \frac{V_H\cdot I_{in}}{V_{base}\cdot I_{base}} = \frac{4}{\pi}I_{s,rpu}\cos\alpha \tag{3.19}$$

The per-unit fundamental capacitor voltage is given as,

$$\begin{cases} V_{C,pu} = I_{s,rpu} \times \dfrac{1}{F} \\ \qquad = \dfrac{2\sqrt{2}}{\pi(\mathrm{F}^2-1)} \sqrt{1 + M^2 \cos^2 \dfrac{\theta}{2} - 2M \cos\phi \cos\theta/2} \end{cases} \tag{3.20}$$

The power transferred in forward power flow can be calculated from the secondary side. Hence, the instantaneous power as evaluated from the output side is

$$\begin{cases} p_{pu}(\mathrm{t}) = v_{oh,pu}(\mathrm{t}) \times i_{s,pu}(\mathrm{t}) \\ \qquad = \dfrac{16MF}{\pi^2(\mathrm{F}^2-1)} \cos\dfrac{\theta}{2} \left(\dfrac{M}{2} \cos\dfrac{\theta}{2} \sin 2(\omega_s \mathrm{t} - \phi) \right. \\ \qquad\qquad \left. - \cos(\omega_s \mathrm{t}) \sin(\omega_s \mathrm{t} - \phi) \right) \end{cases} \tag{3.21}$$

The output real power is the average value of instantaneous power

$$P_{o,pu}(\mathrm{t}) = \frac{1}{2\pi} \int_0^{2\pi} p_{pu}(\mathrm{t}) \times \mathrm{d}(\omega_s \mathrm{t}) = \frac{8MF}{\pi^2(\mathrm{F}^2-1)} \cos\frac{\theta}{2} \sin\phi \tag{3.22}$$

As the range θ is [0, π/2], the above equation reinforces the idea of positive/forward power flow for $\phi \geq 0$ and backward power flow for $\phi \leq 0$. The equation can also be used to calculate the phase-shift angle for a certain amount of power delivery. The power transmission curve with respect to ϕ and θ for F=1.2 and M=1 is shown in Figure 3.12. It demonstrates the power delivery and voltage regulation in terms of two degrees of control freedom. The gain value and the switching frequency also determine the rated power transfer, as discussed later in resonant tank design.

Now the per-unit fundamental transformer current $i_{oh,pu}(\mathrm{t})$ is

$$i_{oh,pu}(\mathrm{t}) = \sqrt{2} I_{\mathrm{oh},rpu} \sin(\omega_s \mathrm{t} - \beta) \tag{3.23}$$

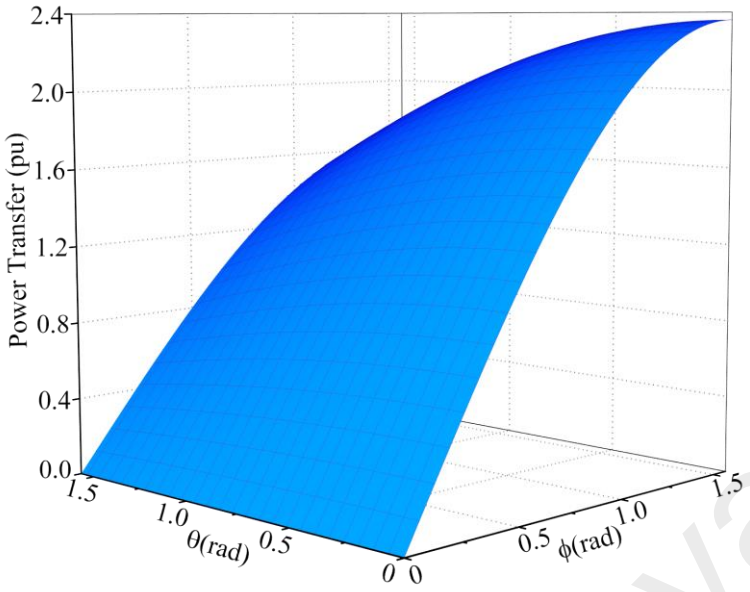

Figure 3.12 Plot of transmitted power with respect to ϕ and θ for F=1.1, k=0.65

where $I_{\mathrm{oh},rpu}$ is the per-unit fundamental transformer RMS current, β is the lagging phase angle with respect to $v_{in,pu}(\mathrm{t})$. The secondary output current is under critical conduction mode. As shown in Figure 3.2, the average value of $i_{oh,pu}(\mathrm{t})$ upon active-rectification at the angles ϕ and β gives the output DC current $I_{0,pu}^{'}$

$$I_{0,pu}^{'} = \frac{1}{\pi}\int_{\phi}^{\pi+\beta} \sqrt{2} I_{\mathrm{oh},rpu} \sin(\omega_s \mathrm{t} - \beta) \tag{3.24}$$

which results in

$$I_{\mathrm{oh},rpu} = \frac{\pi \cdot I_{0,pu}^{'}}{\sqrt{2}[1+\cos(\phi-\beta)]} \tag{3.25}$$

The conventional FHA employs R_{ac} as the equivalent AC resistance of the resonant tank obtained as $8R_o^{'}/\pi^2$ or $\pi^2/8R_o^{'}$. It represents the diode-rectifier, output filter, HF transformer, and DC load. Nonetheless, the active-rectification of secondary switches changes the equivalent resistance in dual-active bridge converters (X. Li, 2014b). Hence, in order to obtain a more accurate steady-state analysis, the equivalent AC resistance R_{ac}

must be replaced by modified equivalent AC impedance $Z'_{o,M,pu}$, which includes the secondary equivalent circuit referred to the primary side consisting of active-rectifier instead of diode-rectifier as in conventional converter. With the help of fundamental values of the transformer voltage and transformer current, $Z'_{o,M,pu}$ can be calculated as the quotient of these. Using (3.12) and (3.24), it can be given as

$$\mathbf{Z'_{o,M,pu}} = \frac{\sqrt{2}V_{\text{oh,rpu}}\cos\frac{\theta}{2}\sin(\omega_s\,\text{t}-\phi)}{\sqrt{2}I_{\text{oh},rpu}\sin(\omega_s\,\text{t}-\beta)} = \frac{\cos^3\frac{\theta}{2}}{Q}\angle(-\theta) \tag{3.26}$$

where $\theta = \phi - \beta$ is the phase angle of the modified AC equivalent impedance and the quality factor Q is given as

$$Q = \frac{\pi^2 Z_{base} P_o}{8n^2 V_o^2} \tag{3.27}$$

The phase angle θ and β has a direct relationship with the controlled phase-shift angle ϕ as

$$\begin{aligned}\theta &= \arctan\left[\frac{M}{\sin\phi}\left(1+k-k/F^2\right)-\cot\phi\right]\\ \beta &= \arctan\left[\frac{\sin\phi}{M\left(1+k-k/F^2\right)}-\cot\phi\right]\end{aligned} \tag{3.28}$$

While observing the phasor-domain equivalent circuit, the input impedance can be defined as,

$$\text{Z}_{\text{in,pu}} = j(F-\frac{1}{F}) + \text{Z}'_{\text{o,M,pu}} \| j\frac{F}{k} = |\text{Z}_{\text{in,pu}}|\angle\alpha \tag{3.29}$$

where $|\text{Z}_{\text{in,pu}}| = \dfrac{Z_1 + jZ_2}{Z_3}$ and

$$
\begin{aligned}
Z_1 &= \frac{F}{k} \\
Z_2 &= \left[(F - \frac{1}{F}) \left(\frac{k \cos^3 \theta/2}{FQ \cos\theta} + \frac{FQ}{k \cos\theta \cos^3 \theta/2} - 2\tan\theta \right) \right. \\
&\qquad \left. + \frac{\cos^3 \theta/2}{Q \cos\theta} - \frac{F}{k}\tan\theta \right] \\
Z_3 &= \frac{k \cos^3 \theta/2}{FQ \cos\theta} + \frac{FQ}{k \cos\theta \cos^3 \theta/2} - 2\tan\theta
\end{aligned}
\tag{3.31}
$$

$$
\begin{aligned}
\alpha = \arctan\left(\frac{Z_2}{Z_1}\right) = \arctan\left[(F - \frac{1}{F}) \left(\frac{k^2 \cos^3 \theta/2}{F^2 Q \cos\theta} + \frac{Q}{\cos\theta \cos^3 \theta/2} \right.\right. \\
\left.\left. - \frac{2k}{F}\tan\theta \right) + \frac{k \cos^3 \theta/2}{FQ \cos\theta} - \tan\theta \right]
\end{aligned}
\tag{3.30}
$$

3.4.1 Voltage Gain

As the converter operates in the inductive region, the operating frequency is always larger than the resonant frequency. The voltage gain of the proposed converter can be calculated by analyzing the two-port model. The voltage gain can be expressed as the absolute quotient value of the referred secondary voltage to primary input voltage given as,

$$
M = \left| \frac{V_{oh,pu}}{V_{in,pu}} \right| = \left| \frac{Z'_{o,M,pu} \parallel jF/k}{Z_{in,pu}} \right| \tag{3.32}
$$

$$
\mathrm{M} = \sqrt{\frac{\left(\frac{F}{k}\right)^2 + \left(\frac{\cos^3 \theta/2}{Q \cos\theta} - \frac{F}{k}\tan\theta \right)^2}{\left(\frac{F}{k}\right)^2 + \left[\left(\frac{\cos^3 \theta/2}{Q \cos\theta} - \frac{F}{k}\tan\theta \right) + \left(F - \frac{1}{F} \right) \left(\frac{k \cos^3 \theta/2}{FQ \cos\theta} + \frac{FQ}{k \cos\theta \cos^3 \theta/2} - 2\tan\theta \right) \right]^2}} \tag{3.33}
$$

The simplified equation of the voltage gain is given as (3.33). The voltage gain, as obtained theoretically, is plotted against the normalized switching frequency, as shown in Figure 3.13. It can be observed that the converter voltage gain is varied broadly for all

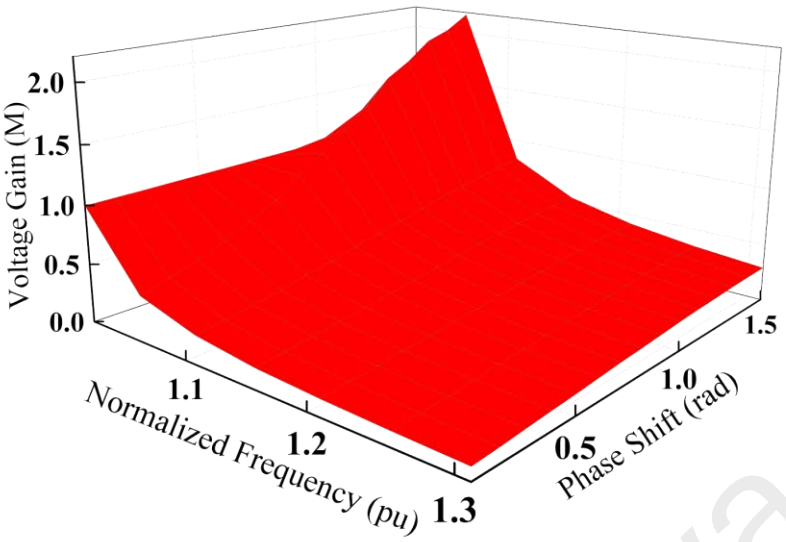

Figure 3.13 Plot of voltage gain with respect to normalized switching frequency for F=1.1, k=0.65 & Q=2.8

phase shift values making it employable for a wide input voltage range. The inductor ratio (k) has minimal outcome on the gain that can be assumed to be non-dependent on k. To design the converter for varying input voltage and loading conditions, the voltage gain is kept constant by controlling the phase shift and the frequency, respectively. The narrow frequency variation to keep voltage gain constant is the added advantage of the employed modulation scheme. The wide frequency variation suffers from the challenge of magnetic components optimization, which can thereby affect the power density and cause more conduction losses.

3.4.2 Voltage and Current Stresses of Power Devices

Based on the operation principles as discussed above, the peak voltage stresses on S_1~S_6 (except S_3/S_4) are $V_{in}/2$ and S_3/S_4 are V_{in}. The peak voltage stresses on Q_1~Q_6 (except Q_3/Q_4) are $V_0/2$, and Q_3/Q_4 are V_0. The peak current stresses are summarized in Table 3.1.

Table 3.1 Summarized Voltage and Current Stress

Power Semiconductor switches	Voltage Stress	Current Stress
$S_1/S_2/S_5/S_6$	$\frac{V_{in}}{2}$	$\frac{2F}{\pi(\mathrm{F}^2-1)}\sqrt{1+M^2\cos^2\frac{\theta}{2}-2M\cos\phi\cos\theta/2}$
S_3/S_4	V_{in}	
$Q_1/Q_2/Q_5/Q_6$	$\frac{V_0}{2}$	$\frac{2nF}{\pi(\mathrm{F}^2-1)}\sqrt{1+M^2\cos^2\frac{\theta}{2}-2M\cos\phi\cos\theta/2}$
Q_3/Q_4	V_0	$-\frac{2nM}{\pi F}k\cos\frac{\theta}{2}$

3.5 Soft Switching Operations

The soft switching of the power MOSFETs is required in the operation of the resonant converters to have minimum switching losses, which can be severe for the converters under the high-frequency application. The soft switching achievement of the power MOSFETs plays an important role in ascertaining that the converter operates in high conversion efficiency. The soft switching operations of the proposed resonant converter can be explained in terms of ZVS operation of primary as well as secondary MOSFETs for all load and input voltage values. The necessary as well as sufficient ZVS constraints have been determined specifically for both sides of switches.

3.5.1 ZVS in Primary Side Switches

The ZVS turn-on of the primary MOSFETs can be secured when the resonant converter is operating under the inductive slope region of the converter gain. Under the inductive region, the input impedance to the fundamental input voltage would be inductive. As a result, the resonant current would lag behind the fundamental primary voltage. Henceforth, the necessary constraint for the primary MOSFETs ZVS is the resonant

current being inductive with reference to the fundamental primary input voltage. This relation in analytical form can be written as $\alpha > 0$. Using (3.31) and simplifying, we have

$$\tan^{-1}\left[(F-\frac{1}{F})\left(\frac{k^2\cos^3\theta/2}{F^2Q\cos\theta}+\frac{Q}{\cos\theta\cos^3\theta/2}-\frac{2k}{F}\tan\theta\right)+\frac{k\cos^3\theta/2}{FQ\cos\theta}-\tan\theta\right]\geq 0 \quad (3.34)$$

After the simplification of (3.34), using (3.28), we have

$$F-\frac{1}{F}\geq\frac{\sin 2\phi-\cos^3\theta/2}{3Q} \quad (3.35)$$

For any values of ϕ and θ, $\sin 2\phi-\cos^3\theta/2$ will always be less than unity, thus further simplifying (3.35) to,

$$F-\frac{1}{F}\geq\frac{1}{3Q} \quad (3.36)$$

The above equation defines the switching frequency range for any selected Q-value for the desired ZVS in all primary MOSFETs. The variation of the input impedance angle (α) and the converter gain with respect to the phase shift angle for a range of Q-values have been plotted in Figure 3.14 using (3.36). It can be seen that the apt selection of phase shift

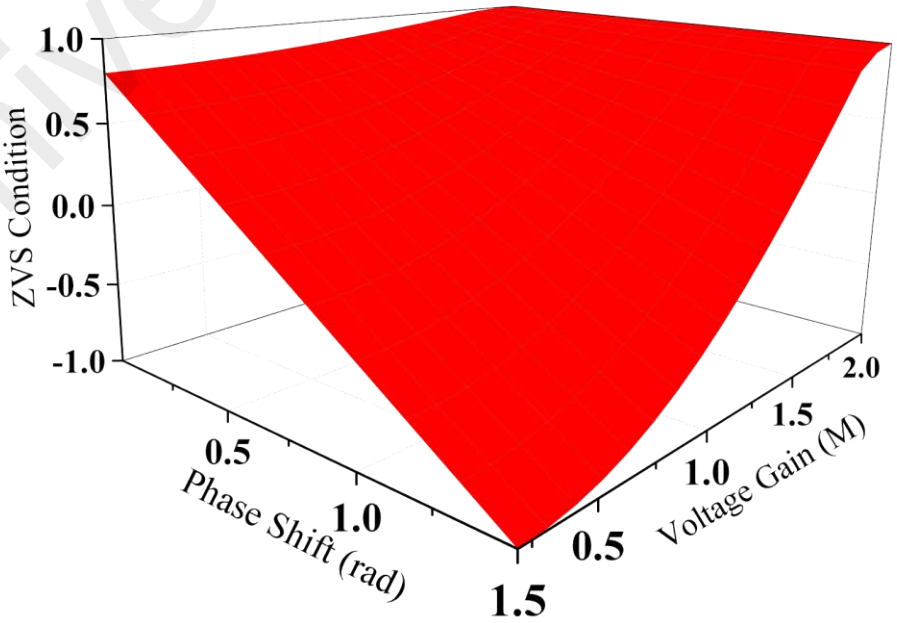

Figure 3.14 Plot of α vs ϕ & M at F=1.1 and k=0.65 for ZVS condition in primary switches

for power transfer can achieve the ZVS in primary switches for the complete range of Q-values for the selected range of switching frequency.

Hence, the positive α for M greater than unity under all Q-values demonstrates the ZVS achievement also for light-load condition, which is usually lost when conventional PSM is used. This implies a wider range of ZVS for all primary MOSFETs. For the fixed frequency SPM control based converter, voltage gain is limited to unity to maintain ZVS turn-on in the primary side switches at light load conditions (Xiaodong Li & Bhat, 2010).

However, as per the dynamics of the converter, the instantaneous resonant current must be large enough to discharge or charge the lossless snubbing capacitances of the MOSFET for turn on and turn off switching operation, respectively. The resonant current for the primary and secondary switches in one-leg of the bridges has been shown in Figure 3.15. Each output capacitor across the switch is the combination of MOSFET drain-to-source capacitance and stray capacitance. When S_2, S_3, and S_6 turn-off, the resonant current i_s charges and discharges the output capacitors C_{oss2}, C_{oss3}, C_{oss6} and C_{oss1}, C_{oss4}, C_{oss5}, respectively. Thus, ZVS turn-on for the switches S_1, S_4, and S_5 can be achieved once C_{oss1}, C_{oss4}, and C_{oss5} are discharged completely. Identically, the realization of ZVS for another

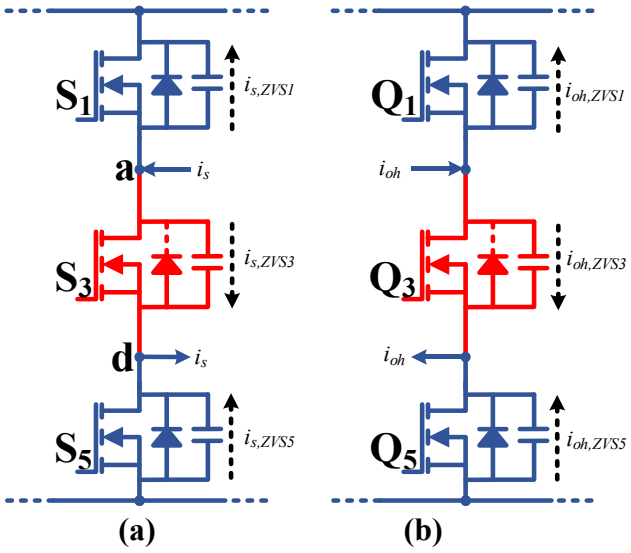

Figure 3.14 Resonant current direction (a) Primary switches and (b) Secondary switches

pair of switches is the same. Assuming, all the output capacitances across the switches have the same value i.e. $C_{oss1} = C_{oss2} = C_{oss3} = C_{oss4} = C_{oss5} = C_{oss6} = C_{oss\_s}$. The current i_s on the primary side is negative. However, the absolute value of i_s should be larger than the resonant current $I_{s,\,ZVS}$ consisting of the resonant tank and the output capacitance of the respective MOSFET during switching transient. The discharging resonant current for MOSFET S_1 and S_5 would be equal and given as $I_{s,\,ZVS1}$, while the charging current for S_3 is given as $I_{s,\,ZVS3}$ with switch voltage different from S_1 and S_5.

$$I_{s,ZVS1} = \frac{C_{oss\_S} \cdot V_{in}/2}{T_d},\ I_{s,ZVS3} = \frac{C_{oss\_S} \cdot V_{in}}{T_d} \tag{3.37}$$

As discussed above, the sufficient condition for ZVS in the primary switches is $\sqrt{2} I_{s,r} \sin\alpha \geq I_{s,ZVS1}$, and by using (3.37), it can be written as,

$$\tan\alpha \geq \frac{C_{oss\_S} \cdot V_{in}^2}{2\pi P_{in} T_d} \tag{3.38}$$

$$\Rightarrow ZVS_p(\phi,\theta) = \cot\phi - \frac{1}{M \sin\phi \cos\theta/2} \geq \frac{C_{oss\_S} \cdot V_{in}^2}{2\pi P_{in} T_d} \tag{3.39}$$

where C_{oss_S} is the output capacitance of primary MOSFETs, and T_d is the gating signal deadband.

The ZVS turn-off of the switches depends on the parallel capacitors, which are limiting the rate of rise of (dv/dt) voltage during the turn-off. The larger the parallel capacitors are lesser are the turn-off losses. However, the current commutates to the parallel capacitors after removing the gate signals, and that helps the switches to turn-off completely before raising the drain-to-source voltages significantly.

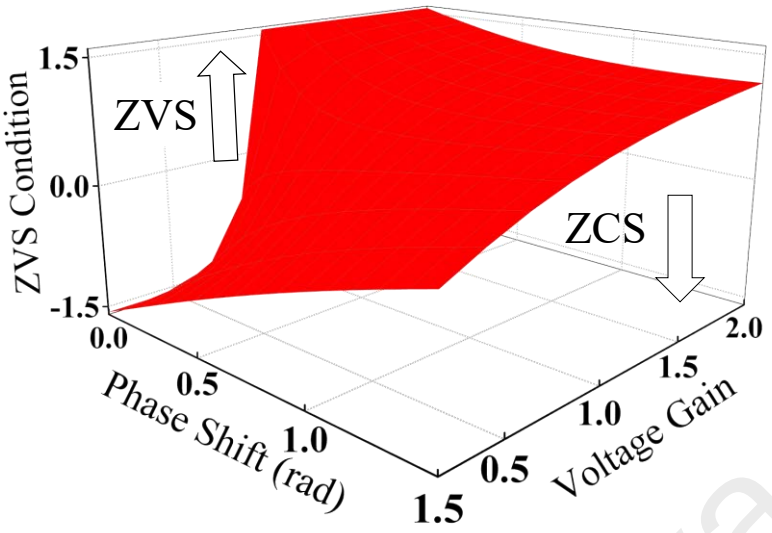

Figure 3.15 Plot of θ vs ϕ and M at F=1.1 and k=0.65 for ZVS condition in secondary switches

3.5.2 ZVS in Secondary Side Switches

On a similar note, as in primary switches, the ZVS in secondary MOSFETs can be achieved by calculating the phase angle between transformer current and voltage. The capacitive transformer current with reference to quasi-square transformer voltage makes sure that the ZVS has been secured. Hence, to sustain the ZVS in the secondary side, the necessary condition is $\phi - \beta = \theta \geq 0$. Using (3.28), the same can be written as,

$$\left[\frac{M}{\sin\phi}\left(1+k-{}^{k}\!/_{F^2}\right)-\cot\phi\right]>0$$
$$\Rightarrow M > \frac{\cos\phi}{1+k-{}^{k}\!/_{F^2}} \tag{3.40}$$

The above equation defines the necessary requirement for ZVS in the secondary switches for all values of phase shift, ϕ.

As in primary switches, the secondary MOSFET body diode must be conducted before its turn on. The positive transformer current, i_{oh} going into the MOSFET, as shown in Figure 3.14(b), should be large enough to charge and discharge the body capacitance of the secondary MOSFETs during the switching operation. The absolute value of i_{oh} should be higher than the resonant current, $I_{oh,ZVS}$ consisting of the input resonant tank and the

output capacitance of the secondary MOSFETs during switching transient. The discharging resonant current for MOSFET Q_1 and Q_5 would be equal and given as $I_{oh,ZVS1}$, while the charging current for Q_3 is given as $I_{oh,ZVS3}$ with switch voltage different from S_1 and S_5.

$$I_{oh,ZVS1} = \frac{C_{oss'\_S} \cdot V_{in}/2}{T_d},\ I_{oh,ZVS3} = \frac{C_{oss'\_S} \cdot V_{in}}{T_d} \tag{3.41}$$

As discussed and using (3.24), we have,

$$i_{oh,pu}(-90-\phi) = \frac{4F}{\pi(\mathrm{F}^2-1)}\left(-\sin\phi + M\cos(\theta/2)\sin(2\phi)\right) + \frac{4F}{\pi k} M\cos\theta/2\sin(2\phi) \geq 0 \tag{3.42}$$

$$\Rightarrow ZVS_s(\phi,\theta) = k \leq \frac{(F^2-1)\left[M\cos(\theta/2)\sin(2\phi)\right]}{\sin\phi - M\cos(\theta/2)\sin(2\phi)} \tag{3.43}$$

The inductor ratio k can be selected for the required range of ZVS in the secondary switches. The switching frequency variation with reference to load, Q-values has been defined in (3.36) for the soft-switching operation of the primary MOSFETs. Henceforth, ZVS can be realized for all MOSFETs whenever the operation of the converter is within the ZVS conditions, as defined in the above discussion.

In conventional DAB-SRC, the maximum switching frequency defines the ZVS conditions. As wide as the frequency range is, wider is the ZVS range. A comparison table, as in Table 3.1, compares the proposed double-phase converter with conventional single-phase converter and three-phase wye-wye converter in terms of the ZVS range, transformer voltage stress, and employed frequency range in modulation scheme. The variable frequency modulation has been employed in the single-phase resonant converter in order to maintain the constant output voltage. On the one hand, the power transfer range is lesser than the three-phase wye-wye converter. On the other hand, the range of ZVS capability is constrained due to the limited frequency range. In other words, the

Table 3.2: Comparison of the Single-Phase Resonant Converter, Three-Phase Resonant Converter and the Proposed Converter

Parameters	Single-phase Resonant Converter	Three-phase Resonant Converter	Proposed Converter
Control modulation	PFM or PSM	PFM	VF-PSM
Primary winding voltage stress	V_{in}	$\frac{2V_{in}}{3}$	$\frac{V_{in}}{2}$
ZVS range	Narrow	Medium	Wide
Frequency range	Wide	Medium	Narrow

limitation in resonant tank design because of the higher frequency range inhibits the ZVS capability of the converter in comparison to the wye-wye converter at the same power rating. The primary transformer current and voltage stress is also higher pertaining to single-phase covering all load ranges, whereas the three-phase converter has reduced voltage as well as current stress. Nevertheless, the wye-wye configuration can be rearranged as three single-phase, thereby limiting the ZVS capability. The wider the frequency range is, the wider is the ZVS capability of the converter. However, the wide switching frequency operation requires a more accurate resonant tank design and causes electromagnetic interference (EMI) disturbances in the converter. The proposed modulation scheme allows the converter to operate in a narrow switching frequency range with an increased ZVS capability range of the converter. The selection of larger inductor ratio k increases the ZVS range of secondary MOSFET switches of the converter. The proposed converter has the lowest voltage and current stresses to the

transformer primary because of the novel topology. The voltage stress is limited to half of the input voltage, which can be highly utilized in medium or high power applications.

3.6 Reverse Power Flow

When the power flows from input to output, a part of power freewheels back to the input side due to the phase difference between the transformer voltage and current, this reverse power flow causes an increase in conduction losses due to freewheeling energy. This becomes severe under minimum input voltage and light load conditions, causing severe conduction losses and thereby affecting the performance of the converter. The operating waveforms for the output current under SPS modulation and the proposed modulation have been drawn in Figure 3.17. The shaded yellow-portion corresponds to the reverse power from the output side to the input side. The negative output current during t_3-t_4 duration causes the reverse power flow in the converter. The reverse power in a half cycle is given as:

$$P_r = \frac{1}{\pi} \int_{0.5-\frac{\theta}{\pi}}^{\pi} v_{oh}(\omega_s t) \cdot i_o(\omega_s t) d(\omega_s t) \tag{3.44}$$

For the proposed modulation,

$$i_o(\omega_s t)=0 \text{ for } (t_3\text{-}t_4) \text{ interval}$$

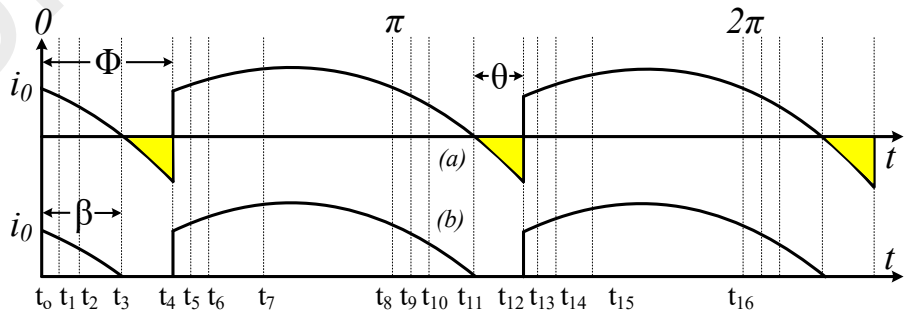

Figure 3.16 Comparison of output current (a) SPS modulation, (b) Proposed Modulation

Hence, theoretically, the reverse power is zero in the proposed converter, which is verified in simulations well as experimental results later. The duty ratio control of secondary switches Q_3 and Q_4 ensures the negative current is zero. The appropriate duty ratio values will ensure the zero reverse power flow in the proposed converter.

3.7 Summary

This chapter discussed the converter operation and its characteristics analysis for the mode of operation. Out of the existing three different steady-state methods: the frequency domain, the state-plane method, and the time-domain method, the frequency-domain approach is taken. The fundamental harmonic analysis employing the Fourier series has been done to avoid the computational burden. The characteristics analysis gives the voltage gain, voltage and current stresses, and ZVS constraints for the power switches. The voltage gain is maintained constant for the changing input voltages and load values by controlling the phase shift and switching frequency. The ZVS constraints for all power semiconductor switches have been discussed in detail. The existence of reverse power in the converter causes degradation in converter performance. The proposed modulation scheme eliminates the reverse power flow from the output side to the input side in the converter. The next chapter discusses the design considerations of the proposed converter, followed by a detailed explanation of the improved control scheme. The converter power loss analysis will also be discussed in the next chapter.

CHAPTER 4: CIRCUIT DESIGN AND PROTOTYPE CONSTRUCTION

4.1 Introduction

On the note of detailed steady-state analysis, a design sample of the prototype is provided in the chapter. The converter parameters are selected as per the required objectives. The prototype to be built has the following design specifications: Power rating P_o = 1.5 kW, Input voltage range V_{in} = 210 V - 400 V, Output Voltage V_o = 80 V. The significance of the design objectives is to maintain a high and wide input voltage range, achieve ZVS operation for the entire load range, and eliminate the RPF due to circulating current at all-load conditions. The magnetics design of the high-frequency transformer and the resonant converter has also been explained. Lastly, the converter power loss analysis has been explained along with the light load efficiency improvement in the proposed converter.

4.2 Selection of Quality Factor at Full-Load

The quality factor Q, having other parameters fixed, must be selected so as to reduce the size of the reactive components and to have minimum resonant RMS current. The quality factor is directly proportional to L_r, L_m, and inversely to C_r, as seen in (3.1)-(3.33). Hence, to have smaller inductive and magnetic components, Q-value should be small. However, a smaller Q-value, using (3.36), could result in a larger switching frequency range, making it complex for magnetic components optimization. Moreover, smaller L_m could cause a larger inductor current independent of load flowing through the parallel inductor. The plot in Figure 4.1 illustrates the variation of resonant RMS current with respect to phase shift for different Q-values at fixed M, F, and k values. From the plot, it can be concluded that the RMS current reduces for smaller Q values, although insignificantly. After the above considerations, a trade-off has to be made, and a full load Q value equal to 2.8 is chosen.

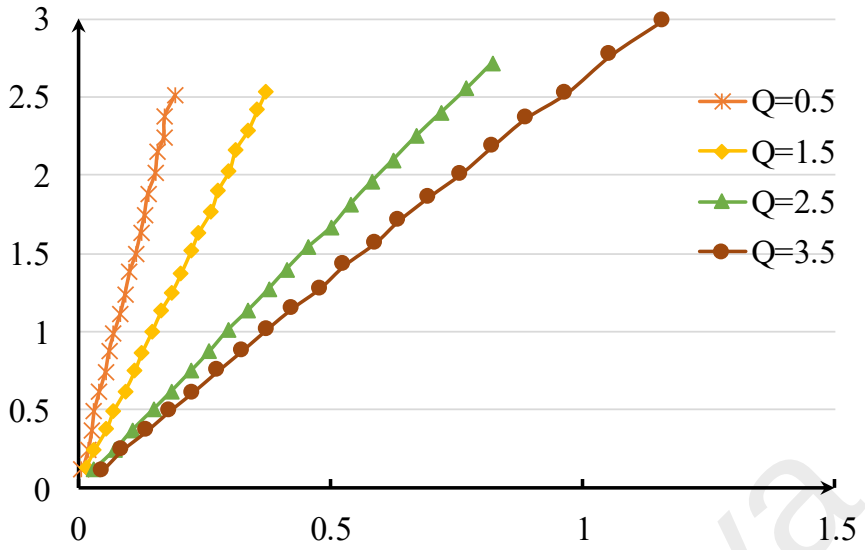

Figure 4.1 Plot of per unit RMS resonant current ($I_{S,RMS,pu}$)vs ϕ at different Q values for F=1.1 & k=0.65

4.3 Selection of Normalized Switching Frequency Range

The switching frequency range plays a vital role in the proper selection of magnetic components. It also ensures ZVS operations in all MOSFETs on primary as well as on secondary bridges. For the selected Q = 2.8 value, the switching frequency range can be calculated using (3.36). The sequential frequency selection with varying load results in load-independent voltage gain. For the desired operation of load change from 20% load to full load, the quality factor Q ranges from 0.56-2.8, respectively. This range of Q value results in the normalized switching frequency range of 1.061-1.341, which is calculated using (3.36). This range can be iteratively attuned to keep ZVS in check and enhance converter performance.

4.4 Selection of Converter Gain

The converter gain, M, should be chosen in such a manner that the ZVS conditions are maintained for all input voltage and load variations. In order to select the minimum converter gain M_{min}, the plot of θ vs. ϕ for different M values has been analyzed, as in

Figure 3.16. For any selected value of converter gain M greater than 0.84, the ZVS conditions are satisfied. From the above discussion, we have,

$$M_{\min} = 0.84 \tag{4.1}$$

Therefore, with the design point of maximum input voltage, the transformer turn ratio can be calculated as,

$$n = \frac{M_{\min} \cdot V_{in\_\max}}{V_o} \tag{4.2}$$

$$n = 21:5 \tag{4.3}$$

Using n, the maximum converter gain is calculated as,

$$M_{\max} = \frac{n \cdot V_o}{V_{\text{in\_min}}} \tag{4.4}$$

Hence,

$$M_{\max} = 1.6 \tag{4.5}$$

4.5 Selection of Inductor Ratio

The inductor ratio *k* has no to little effect on the gain values in the proposed converter. The inductor ratio *k* (or magnetizing inductor L_m) governs the ZVS range of secondary MOSFET switches. The larger the inductor ratio *k* is, the larger is the ZVS range. However, the conventional PSM and variable frequency PSM proposed in (Shakib & Mekhilef, 2017) discuss the limitation of larger inductor ratio k of increased reverse energy or circulating power in the converter under light-load conditions. The circulating current causes increased conduction losses, thereby reducing the converter efficiency. However, this limitation can be overcome using the proposed modulation scheme. The control technique ensures the proper control of secondary switches with varying duty cycle control and not allowing the negative secondary current flowing back to the

primary. This results in the circulating current suppression by the control technique, thereby permitting the increased value of inductor ratio k for increasing the secondary ZVS range. Based on the discussion, the ZVS condition in (3.40) should be satisfied by the selected inductor ratio k. Thereby calculating inductor ratio k at the extreme conditions, i.e., ϕ=0, no-load, F_{max} = 1.341, M_{min} = 0.84, we have

$$k > 0.428 \tag{4.6}$$

Therefore, $k = 0.428$ has been selected as the inductor ratio to maintain ZVS conditions in the secondary MOSFET switches. Moreover, the larger inductor ratio increases the ZVS range with no increased reverse power in the converter, thereby maintaining the efficiency of the converter.

4.6 Design of Resonant Tank Components

With the selected value of inductor ratio, k the variation of M, α, and θ with respect to phase shift has been plotted in Figure 4.2 for selected values of Q and F. It can be

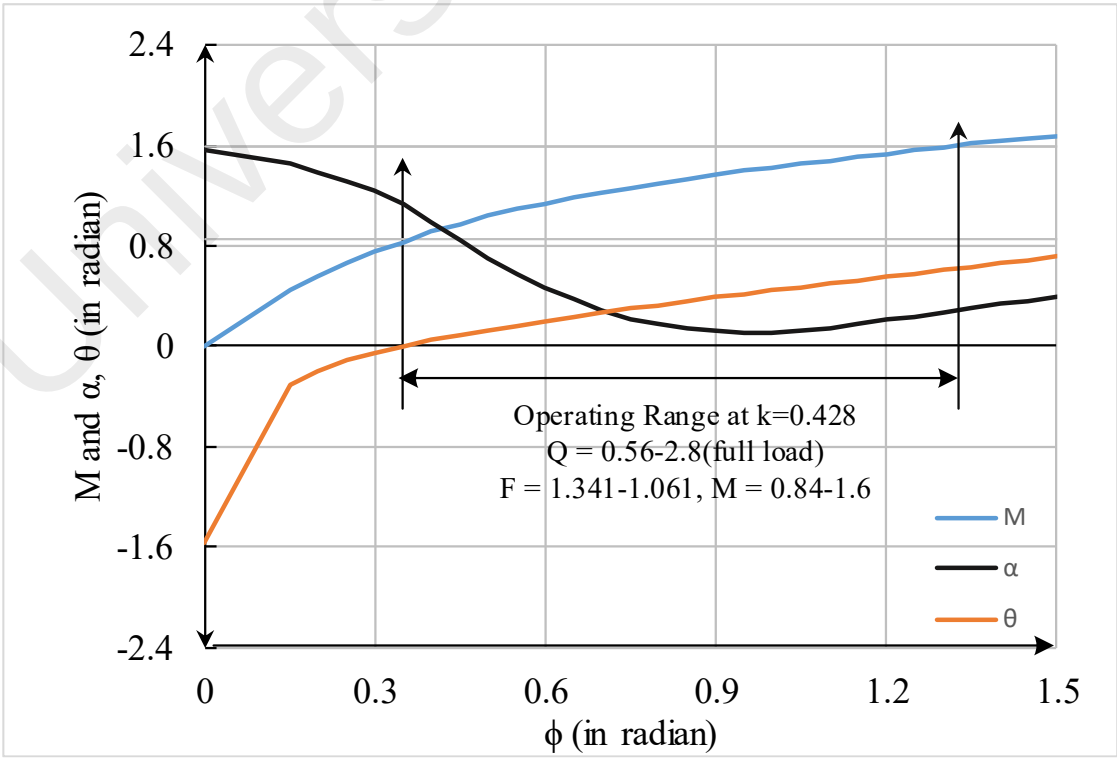

Figure 4.2 Plot of gain (M), α and θ vs ϕ at the operating conditions

established that α and θ are always positive in the entire range of operation. In other words, ZVS is achieved for both primary as well as secondary MOSFETs for the selected gain range of 0.84-1.6. Finally, using (3.7)-(3.9) and (3.27), the resonant components have been calculated as discussed further.

$$L_r = \frac{8R_oQn^2}{\pi^2\omega_r} = 362.52\ \mu\text{H} \tag{4.7}$$

$$C_r = \frac{\pi^2}{8\omega_r R_o Q n^2} = 12.41\ \text{nF} \tag{4.8}$$

$$L_m = \frac{L_r}{k} = 847\ \mu\text{H} \tag{4.9}$$

With the calculated resonant tank components, the complete design specifications of the converter are given as in Table 4.1.

Table 4.1 Designed Specifications of the Prototype

Parameters	Value
Rated Output Power, P_o	1500 W
Input Voltage, V_{in}	210-400 V
Output Voltage, V_o	80
Resonant Frequency, f_r	75 kHz
Transformer Turns ratio (n:1)	4.2
Resonant Inductor (L_{r1} , L_{r2})	181.26 µH
Resonant Capacitors (C_{r1}, C_{r2})	24.82 nF
Output Filter Capacitor (C_o)	100 µF
Magnetizing Inductance (L_{m1}, L_{m2})	423.5 µH
Load Resistance, R_o	4.27 Ω

4.7 Improved Modulation Scheme

As seen in (3.22), the power transferred to the output is controlled by phase shift angle (ϕ) along with the switching frequency (f_s) and the control angle θ (defining the duty ratio

for secondary switches). To limit the reactive power flow and overcome the unity gain issue with ZVS, the SPM has been modified and been termed as variable frequency zero circulating current phase shift modulation (VF-ZCCPSM). A simplified block diagram of the proposed technique has been shown in Figure 4.3.

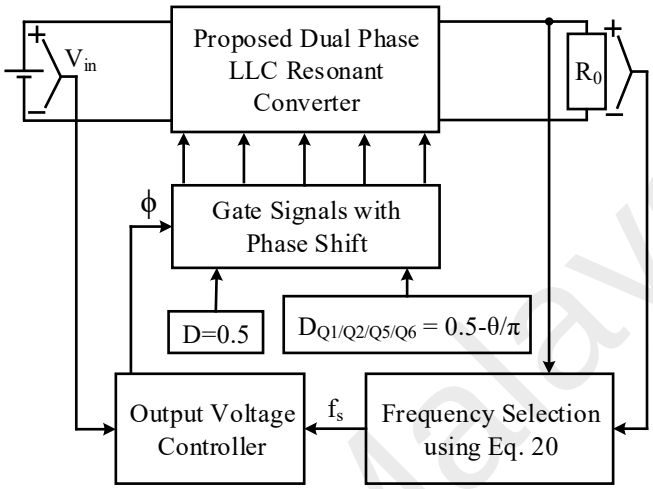

Figure 4.3 Simplified block diagram of the proposed modulation scheme

The switching frequency range is defined solely by the variation of load (Q-values) to achieve ZVS in the primary MOSFETs. The selective frequency approach minimalized the effect of Q-value and maintained an identical voltage gain characteristic of all phase shift angle values. Furthermore, the phase shift angle is regulated to maintain the constant output voltage for varying input voltage and maintain the frequency range within the defined limits. Additionally, the duty ratio control of the secondary switches (Q_1/Q_2 and Q_5/Q_6) calculates the suitable duty ratio to eliminate the reverse power in the converter.

In order to implement the derived control law, a high precision DSP TMS320F28335 with the system clock of 150MHz is employed. The ePWM module operating in up and down count mode generates the gate signals for the switches. The A/D input of the DSP samples the voltage input and regulates the phase shift, switching frequency, and duty

ratio by changing the register values. Hence, the output voltage can be maintained for the required values using the control flowchart, as shown in Figure 4.4.

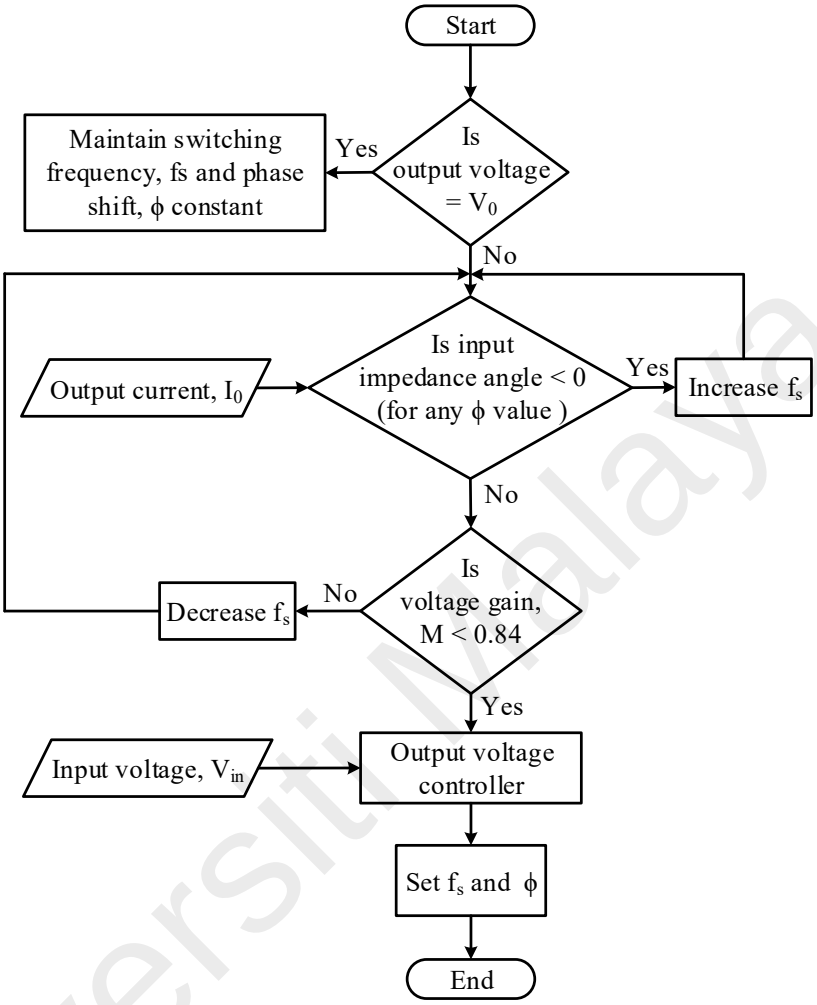

Figure 4.4 Flowchart for the proposed control scheme

4.8 Loss Modelling of Converter

In the previous chapter, equations based on a lossless circuit model describe the waveforms and magnitudes of currents and voltages. When the voltage drops in the switching networks and other circuit components are small compared to the input source, the lossless model is rational. However, all potential losses have to be taken into account in order to achieve a precise power loss model. The switching and conduction losses of the switching networks, magnetization, and resistive losses of the magnetic components of the power converters are usually the main power loss contributors.

The model of the circuit shown in Figure 3.1 is the optimal model where all the devices are in ideal conditions. Conduction losses in the switches depend upon ON-state resistances and the currents flowing through them. Resistive losses in magnetic components' winding resistance and corresponding series resistance (ESR) in capacitors occur in the form of I^2R. Moreover, the switching losses depend on the switching characteristics of the MOSFETs.

4.8.1 Switching Power Loss

The switching turn-on and turn-off power losses contribute to the switching losses. As the ZVS is achieved for primary as well as secondary MOSFETs, the switching turn-on losses can be accounted for as zero, and the switching losses only consist of turn-off losses. In addition, when stored energy in the output capacitors (C_{oss}) is transferred from one MOSFET to another, turn-off losses are considered. The MOSFET turn-off loss is given as

$$P_{turn\_off} = \frac{V_{ds\_off} I_{d\_off}}{2} t_f f_s \tag{4.10}$$

where V_{ds_off} is the reverse blocking voltage of MOSFET, I_{d_off} is the MOSFET turn-off current, t_f is fall time, and f_s is the switching frequency.

4.8.2 MOSFET Conduction Loss

The conduction losses in the primary side switches are dependent on RMS currents following through the switches and on state drain-to-source resistance of the switches. Also, conduction losses in the resonance inductor and transformer are defined by the respective RMS currents and equivalent series resistances. For the secondary side, the current flows through the switch in the reverse direction for a longer time duration in a half switching period. So, switching currents could be divided to flow in between body diode and switch or only through switch itself. However, for the high voltage MOSFET

switch, the reverse voltage is large enough to forward bias its body diode, then the current will be partitioned between MOSFET and its diode to achieve the reverse voltage drop. For the low voltage MOSFET, it can be assumed that the body diode will not conduct as the MOSFET drain-to-source on-state resistance is insufficiently small that the body diode will not reach the threshold. The body diodes conduct only for a short interval of time before turning on the MOSFETs in the primary side, and the magnitudes of the currents at that time are very small. Hence, the conduction losses due to body diode can be negligible in this case. Thus, the total conduction losses can be defined as follows,

$$\begin{aligned} P_{cond} &= P_{cond\_pri} + P_{cond\_\sec} \\ &= \sum I^2{}_{s,rms} R_{ds\_on\_pri} + \sum I^2{}_{oh1,rms} R_{ds\_on\_\sec} \end{aligned} \tag{4.11}$$

Where $I_{s,\ RMS,}$ and $I_{oh1,\ RMS}$ are primary and secondary RMS current, and R_{ds_on} are respective on-state resistances of the MOSFETs.

4.8.3 Gate Driver Loss

Gate driver losses for any switching device depend on the energy supplied by the driver itself during the charging process of the gate and the energy which is stored in the gate of the device at the end of the turn-on. The total energy loss can be defined by the following equation.

The energy loss per switching period is given by

$$E_g = 2 \cdot \left(\int V_g I_g(\mathrm{t})\,\mathrm{dt} - \frac{1}{2} Q_g V_g \right) = Q_g V_g \tag{4.12}$$

with the total gate charge depending on the gate current $I_g(t)$,

$$Q_g = \int I_g(\mathrm{t})\,\mathrm{dt} \tag{4.13}$$

where Q_g is the total gate charge, V_g and I_g are the gate driver voltage and current, respectively.

4.8.4 Magnetic Loss

The magnetic losses occurring in the resonant inductor and the transformers can be classified into two as conduction loss and core loss. The conduction loss in the resonant inductor is given as

$$P_{cond\_ind} = I^2_{s,rms} R_{dc\_ind} \tag{4.14}$$

where R_{dc_ind} is the dc resistance of the inductor, which can be measured using LCR meter and $I_{s,RMS}$ is the primary RMS resonant current.

Steinmetz's equation is used to estimate the core loss in the transformer.

$$P_{core\_ind} = \mathrm{V_e} C_m f^x B^y{}_{AC} \tag{4.15}$$

Where V_e is the effective core volume area, C_m, x, and y are constants based on the core material and provided from the datasheet, and B_{AC} is the AC flux density in the core.

Lastly, the conduction loss in the transformer windings is calculated using

$$P_{cond\_tr} = I^2_{\mathrm{s},rms} R_{dc\_\mathrm{pri}} + I^2_{oh,rms} R_{dc\_\mathrm{sec}} \tag{4.16}$$

where $I_{s,RMS,}$ and $I_{oh,RMS}$ is the RMS transformer primary, and secondary current and R_{dc_x} are the winding resistances.

4.9 Summary

This chapter discussed the design considerations for the proposed isolated bidirectional resonant converter. It mentioned the ZVS range for constant frequency SPM scheme based resonant converter. However, a variable frequency and duty cycle control have

been integrated with SPM control to increase the ZVS operation range for wide load and voltage gain as well as to eliminate the reverse power flow in the converter. Accordingly, the parameters like full load quality factor, switching frequency range, inductor ratio, and resonant tank components have been selected for the specified power range. The modified control has changed the characteristics of conventional bi-directional DC/DC converter in terms of voltage gain and ZVS range. The RMS resonant current and reverse power flow play a major role in deciding the conduction losses, so their reduction would result in a significant enhancement in power efficiency. The following chapter verifies the theoretical analysis through various simulation and experimental results.

CHAPTER 5: RESULTS AND DISCUSSIONS

5.1 Introduction

In this chapter, the prototype specifications mentioning the employed components, design considerations along with the simulation and experimental results for different input voltage and load conditions have been discussed. Firstly, the proposed converter is simulated in MATLAB to verify the operating characteristics, and the simulation results have been presented. Secondly, the experimental tests are done on the built laboratory prototype to validate the experimental results with the simulation results. The power loss distribution, along with the measured efficiency of the proposed converter, is further presented. Lastly, the comparisons of the proposed LLC resonant converter has been performed with the recent state of works based on parameter/components and cost.

5.2 Prototype Specifications

The parameters and specifications of the converter have been listed in Table 4.1. The input voltage varies from 210 V- 400 V maintaining a constant 80 V output voltage. To achieve reduced power losses and for high-frequency operation, SiC MOSFETs C2M0280120D are used as S_1~S_6 suitably rated for medium to high voltage applications. IRFSL4227PbF has been chosen as secondary MOSFETs. It is noteworthy that the primary MOSFET's peak voltage stress of the proposed circuit is 200 V for 4 out of 6 MOSFETs. However, due to the availability of the switching devices in the laboratory, 1200V SiC MOSFETs are used in the prototype design. The dead-band is sufficiently chosen to achieve the ZVS operation and avoid the simultaneous conduction of the switches in the same leg avoiding the short circuit of source or load. A high resonant frequency is chosen so as to reduce parasitic effects in the circuit, which could be there due to unwanted resonance between the resonant inductor and parasitic capacitances in the circuit. The multithread Litz wire is used for the windings with a transformer turns ratio of 21:5. To assimilate the parallel inductor into the HF transformer, an air-gap is

meaningfully added in the middle polar and side limb of the core. Hence, the magnetizing inductance of each transformer is 423.5 μH. A control board of eZdspTMS320F28335 by Texas Instruments (TI) is employed for realizing the proposed modulation scheme and getting the driving signal for the MOSFETs.

5.3 Simulation Results

The designed converter has been modelled and simulated in the MATLAB environment to substantiate the theoretical analysis. The simulation results have been compiled for different input voltage and load operating conditions. The simulation plots for the full load and 20% load condition at the maximum input voltage have been given in Figure 5.1 and Figure 5.2, respectively. Figure 5.3 and Figure 5.4 represent the results under the same loading conditions for minimum input voltage. For every plot, Figure (a) shows the v_{ab}, v_{cd}, $i_{Lr1,}$ and v_{cr}. Figure (b) depicts the v_{ab}, v_{oh1}, i_{oh1}, and i_o. The identical v_{ab} and v_{cd} in Figure 5.1(a) verify the ability of the proposed topology to generate two square pulses with the combination of six switches. The same resonant current flows through both the resonant tank; hence the waveform i_{Lr1} depicts the resonant current in the converter. Waveform v_{cr} under all test gives the resonant capacitor voltage, which is nearly sinusoidal. For the changing load condition, only the switching frequency is changed and remains constant for a fixed load for any input voltage values. The phase shift values maintain the constant output voltage in case of changing input voltages regardless of load conditions. From the theoretical analysis, the range of phase shift angle is from 0.33 to 1.34 radian, as can be verified from Figure 4.2. It can be observed that θ becomes large for lower input voltage. However, the suitable duty cycle calculation of the upper (Q_1, Q_2) and lower (Q_5, Q_6) secondary switches according to θ ensure zero circulating current for all the different operating conditions and thereby eliminating the reverse power in the converter, hence increasing the efficiency. However, it is observed that the voltage and current stresses become larger at lower input voltage conditions. The

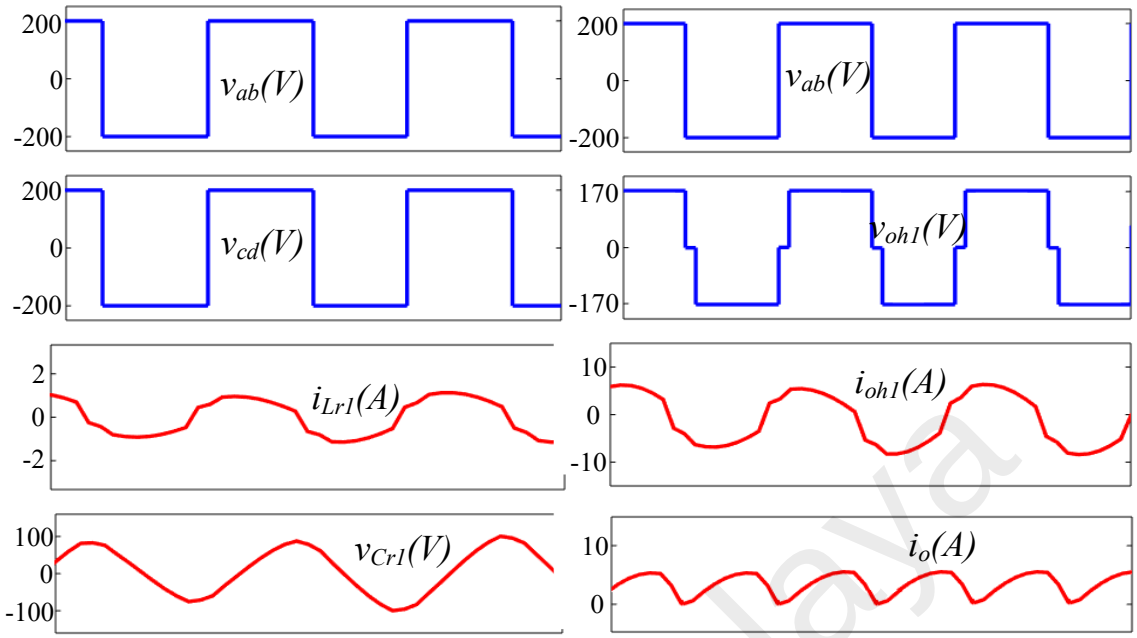

(a) **(b)**

Figure 5.1 Simulation waveforms of the proposed converter for 400-V input, 80-V output at full load

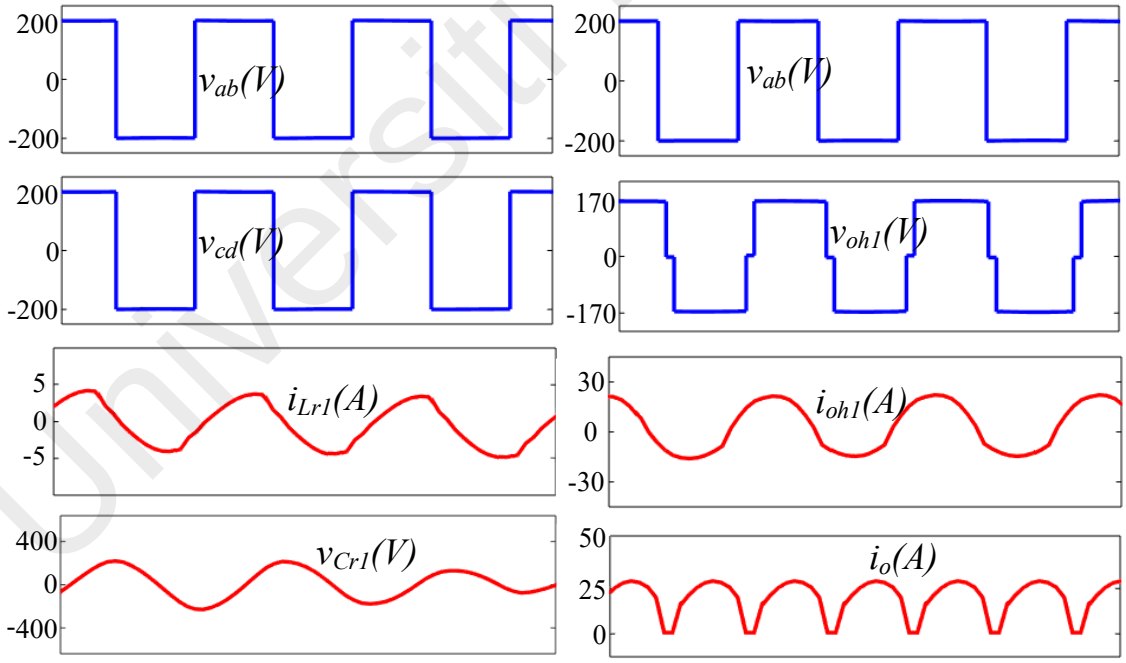

(a) **(b)**

Figure 5.2 Simulation waveforms of the proposed converter for 400-V input, 80-V output at 20% load

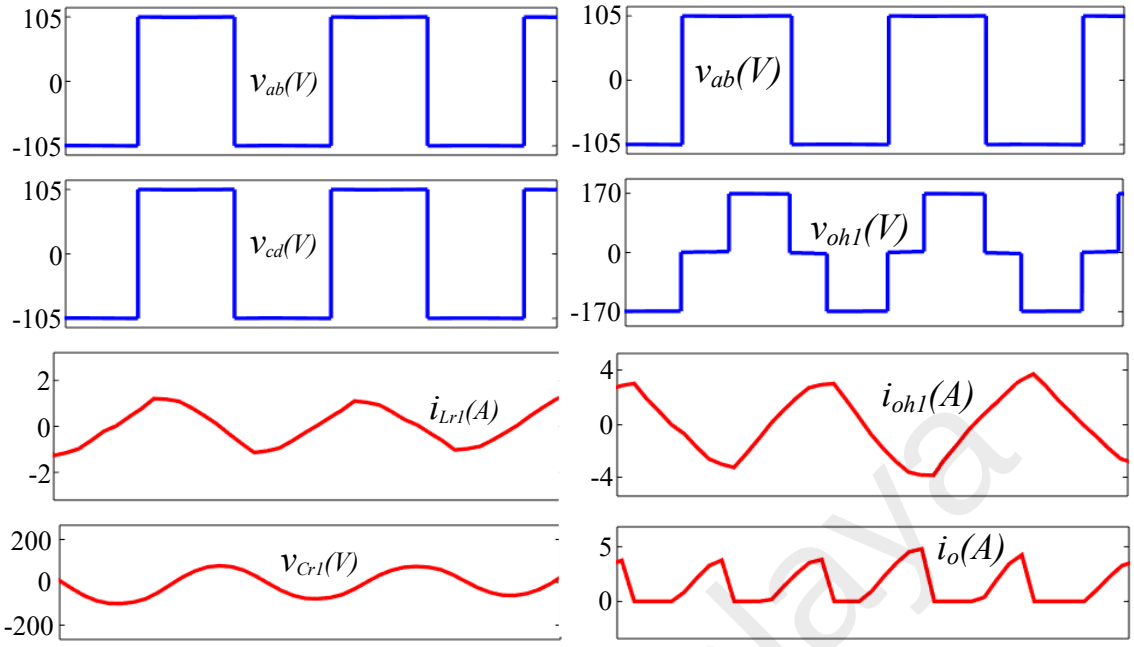

(a) **(b)**

Figure 5.3 Simulation waveforms of the proposed converter for 210-V input, 80-V output at full load

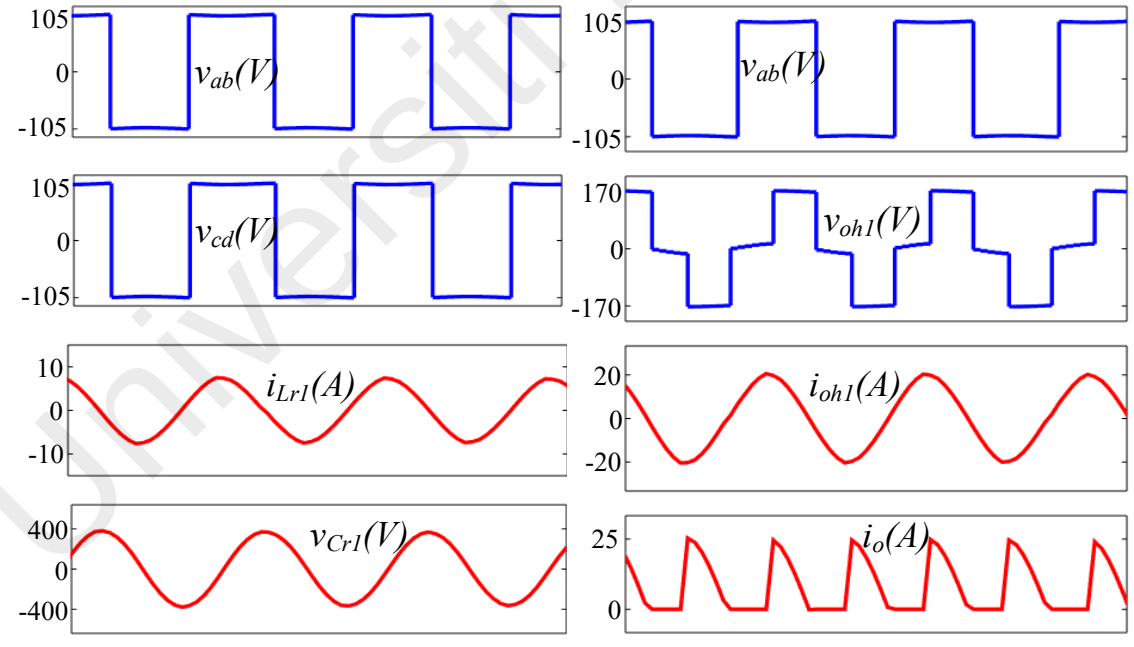

(a) **(b)**

Figure 5.4 Simulation waveforms of the proposed converter for 210-V input, 80-V output at 20% load

simulation ZVS can be verified by analyzing the waveforms of i_{Lr1} and i_{oh1} with respect to v_{ab} and v_{oh1}, respectively.

5.4 Experimental Results

A 1.5kW lab prototype of the proposed dual-phase LLC resonant DC-DC converter with the resistive load was built and effectively tested to verify the theoretical as well as simulation results, which is illustrated in Figure 5.5. The specifications of the prototype converter are as mentioned in Section 5.2.

As discussed earlier, in the proposed converter, the secondary side LV bridge

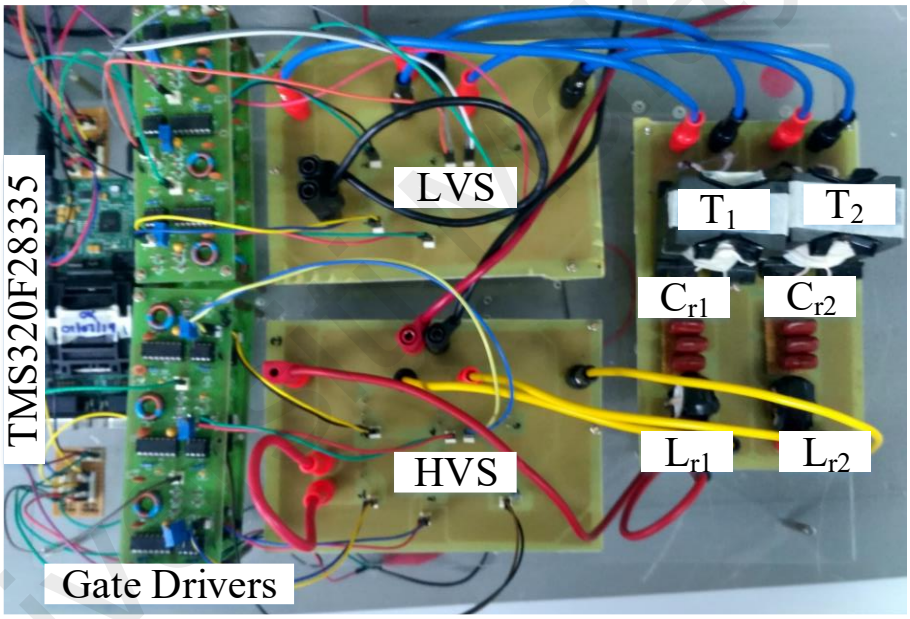

Figure 5.5 A lab-built prototype of the proposed converter

produces a quasi-square voltage as the upper and lower switches are duty cycle controlled and turned off, as shown in Figure 3.2. The primary side HV bridge provides a square voltage waveform as all six switches are conducting. The experimental waveforms for forward power flow operation depicting the similar characteristics as in simulation waveform are presented in Figure 5.6 - Figure 5.9. The operating switching frequency varies with the load only and remains fixed for constant load irrespective of input voltage values. For changing input voltages, ϕ changes to regulate the output voltage constant

regardless of changing loading conditions. It is observed that for low input voltages, the duty ratio of S_3/S_4 reduces largely to compensate for the increased reverse power. Henceforth, for the identical power output, the current i_o shows a larger zero current portion at 210V than 400V, which can be verified in the subsequent results. Figure 5.6 shows the key waveforms in forward power flow operation of the converter at 400 V input voltage under full load condition. Figure 5.6(a) depicts the identical square voltage from the primary LV bridge. The resonant capacitor voltage, v_{cr} is nearly sinusoidal, as can be

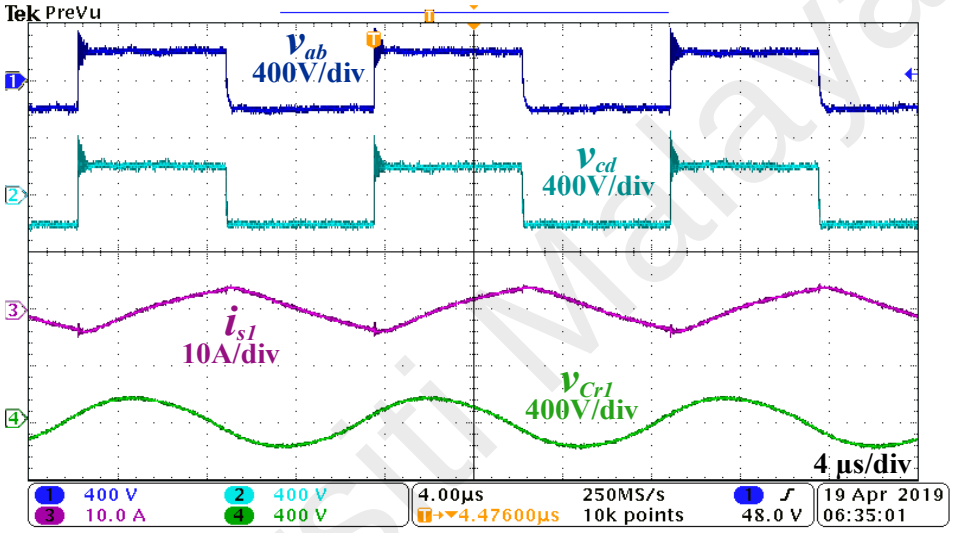

(a)

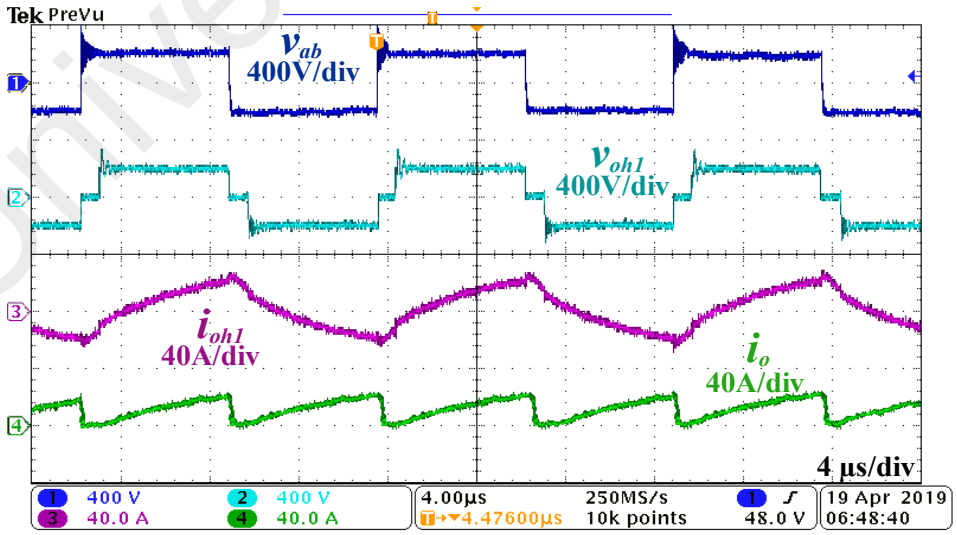

(b)

Figure 5.6 Experimental waveforms of the proposed converter prototype at 400 V input, 80 V output at full load (a) v_{ab} (CH1), v_{cd} (CH2), i_{s1} (CH3), and v_{Cr1} (CH4) (b) v_{ab} (CH1), v_{oh1} (CH2), i_{oh1} (CH3), and i_o (CH4)

seen from the waveform. Figure 5.6(b) shows the experimental waveforms for the square input voltage, quasi-square transformer primary voltage, the secondary current, and the output current. It can be seen in Figure 5.6(b), the circulating current could exist if there is no duty cycle control of the secondary upper and lower leg switches. However, there is no circulating current (eliminated negative current portion) in the output side of the converter. Figure 5.7 shows the key waveforms for the forward power flow operation under a 20% load condition at 400 V input voltage. The larger amount of circulating

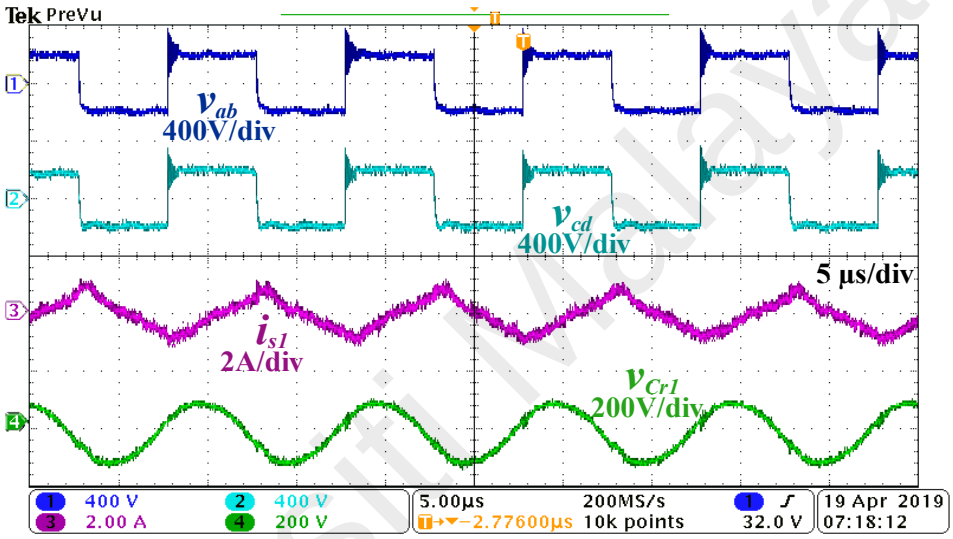

(a)

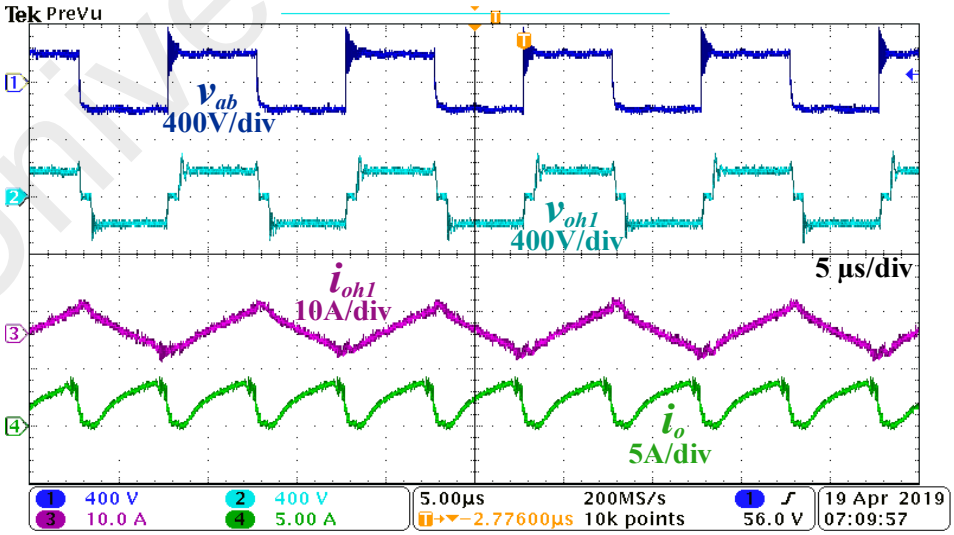

(b)

Figure 5.7 Experimental waveforms of the proposed converter prototype at 400 V input, 80 V output at 20% load (a) v_{ab} (CH1), v_{cd} (CH2), i_{s1} (CH3), and v_{Cr1} (CH4) (b) v_{ab} (CH1), v_{oh1} (CH2), i_{oh1} (CH3), and i_o (CH4)

current under light load condition needs larger duty cycle control, which can be observed in the output side current waveform in Figure 5.7(b), thereby eliminating the circulating current. The primary resonant current waveform is quite similar to theoretical resonant current. Figures 5.8 and 5.9 show the keys waveforms for the forward power flow under 210 V input voltage for full load and 20% load conditions, respectively. The identical v_{ab} and v_{cd} in Figure 5.8(a) verify the ability of the proposed topology to generate two square

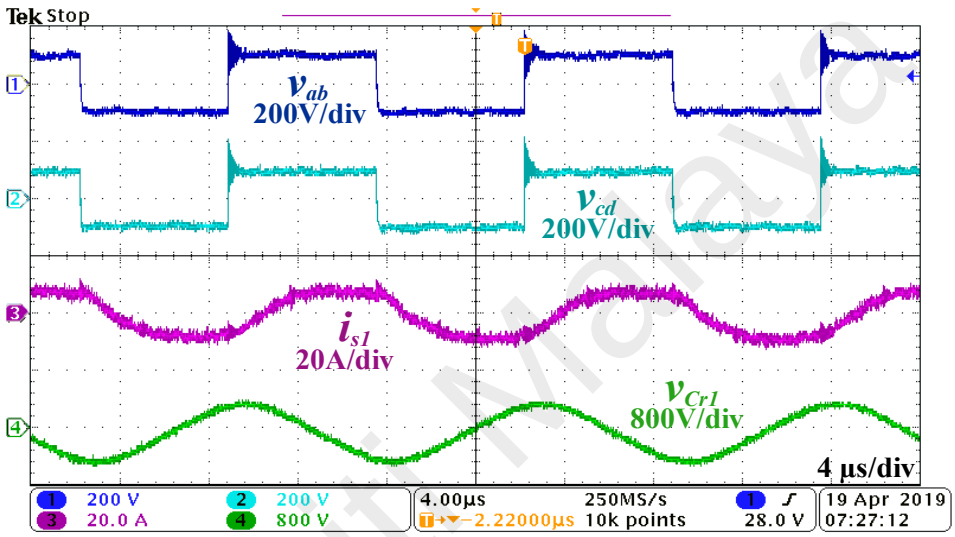

(a)

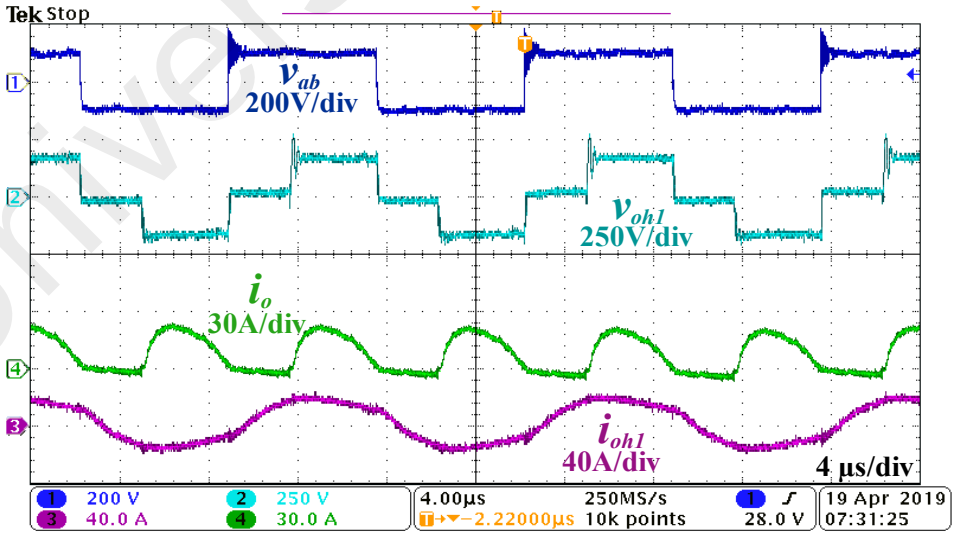

(b)

Figure 5.8 Experimental waveforms of the proposed converter prototype at 210 V input, 80 V output at full load (a) v_{ab} (CH1), v_{cd} (CH2), i_{s1} (CH3), and v_{Cr1} (CH4) (b) v_{ab} (CH1), v_{oh1} (CH2), i_{oh1} (CH3), and i_o (CH4)

pulses with the combination of six switches. Waveform v_{cr} under all test gives the resonant capacitor voltage which is nearly sinusoidal. On the same note, Figure 5.9 depicts the converter performance under minimum input voltage and load conditions. It can be observed that under such conditions, the reactive power flow is large, hence the required duty cycle would me smaller to eliminate any reactive power. Therefore, large part of output current, i_o is zero.

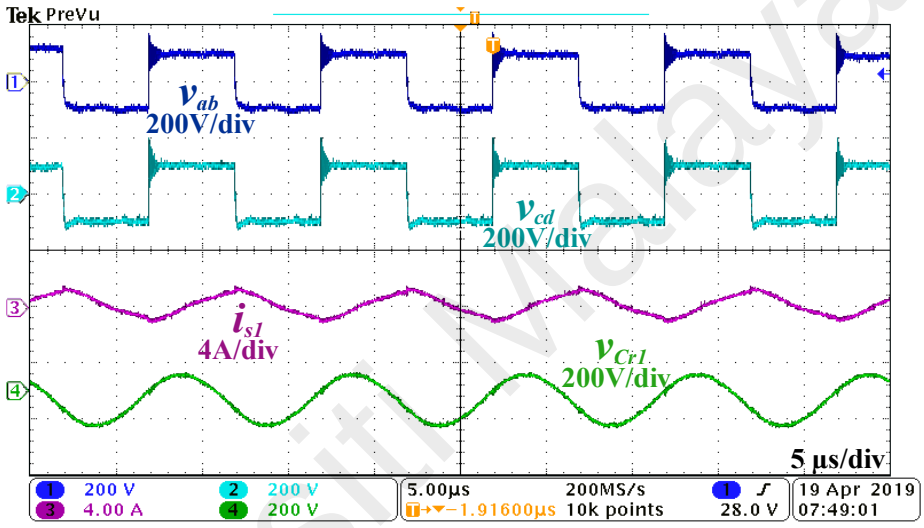

(a)

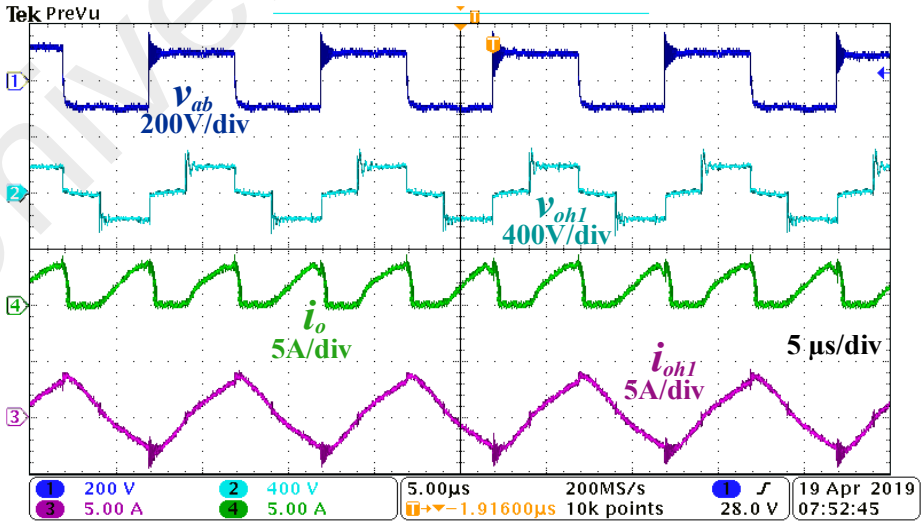

(b)

Figure 5.9 Experimental waveforms of the proposed converter prototype at 210 V input, 80 V output at 20% load (a) v_{ab} (CH1), v_{cd} (CH2), i_{s1} (CH3), and v_{Cr1} (CH4) (b) v_{ab} (CH1), v_{oh1} (CH2), i_{oh1} (CH3), and i_o (CH4)

Figure 5.10 and Figure 5.11 illustrate the ZVS operation of the primary switches under different loading conditions at maximum and minimum input voltage. Figure 5.10 shows the gate signal and drain-source voltage (V_{ds}) waveforms of switches S_1, S_3, and S_5 at maximum input voltage under different load conditions. The V_{ds} goes zero before the gate turn-on of the switch signifies the ZVS operation of the switches. As ZVS is illustrated

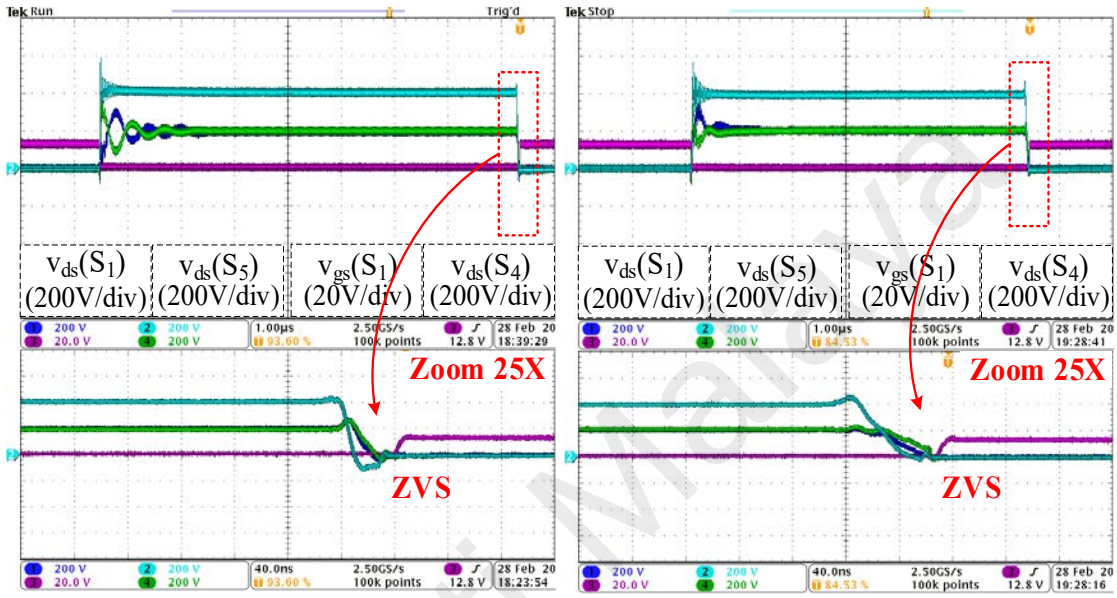

(a) **(b)**

Figure 5.11 Experimental waveforms of the primary MOSFETs for 400-V input (a) Full load (b) 20% load

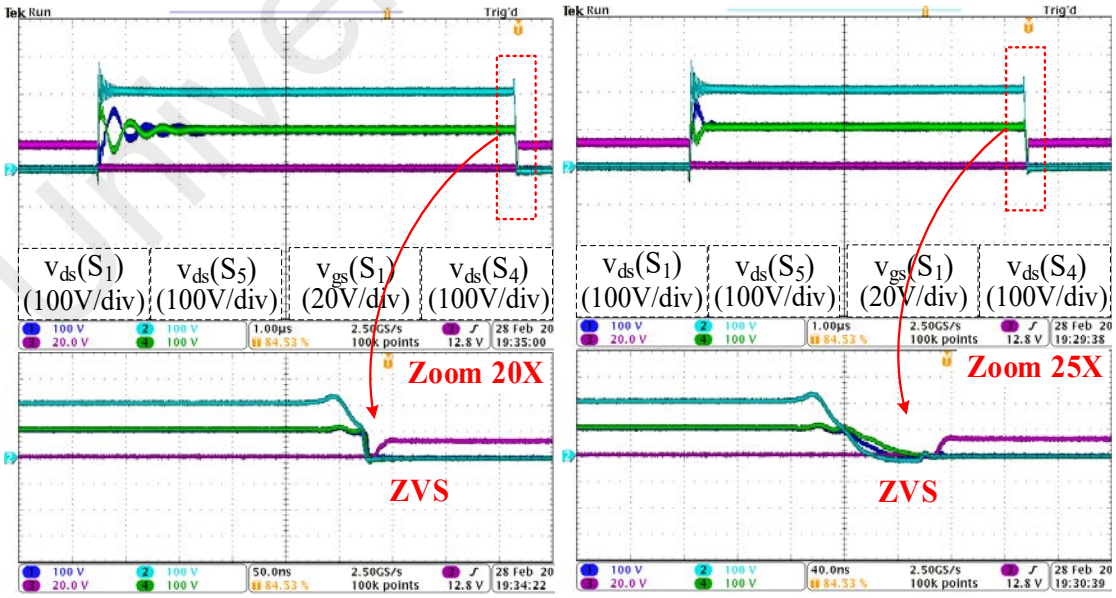

(a) **(b)**

Figure 5.10 Experimental waveforms of the primary MOSFETs for 210-V input (a) Full load (b) 20% load

on both sides during turn-on, the turn-on switching losses become insignificant. Figure 5.11 presents the turn-on of the primary switches S_1, S_4, and S_5. The V_{ds} waveform does not depict any significant voltage spikes across the switch, which implies the ZVS turn-on and switching losses are also decreased. It is noteworthy that there is switching instant drain-source voltage mismatch between the series-connected switches for which external circuitry would be required to balance the voltage for transient as well as steady-state condition.

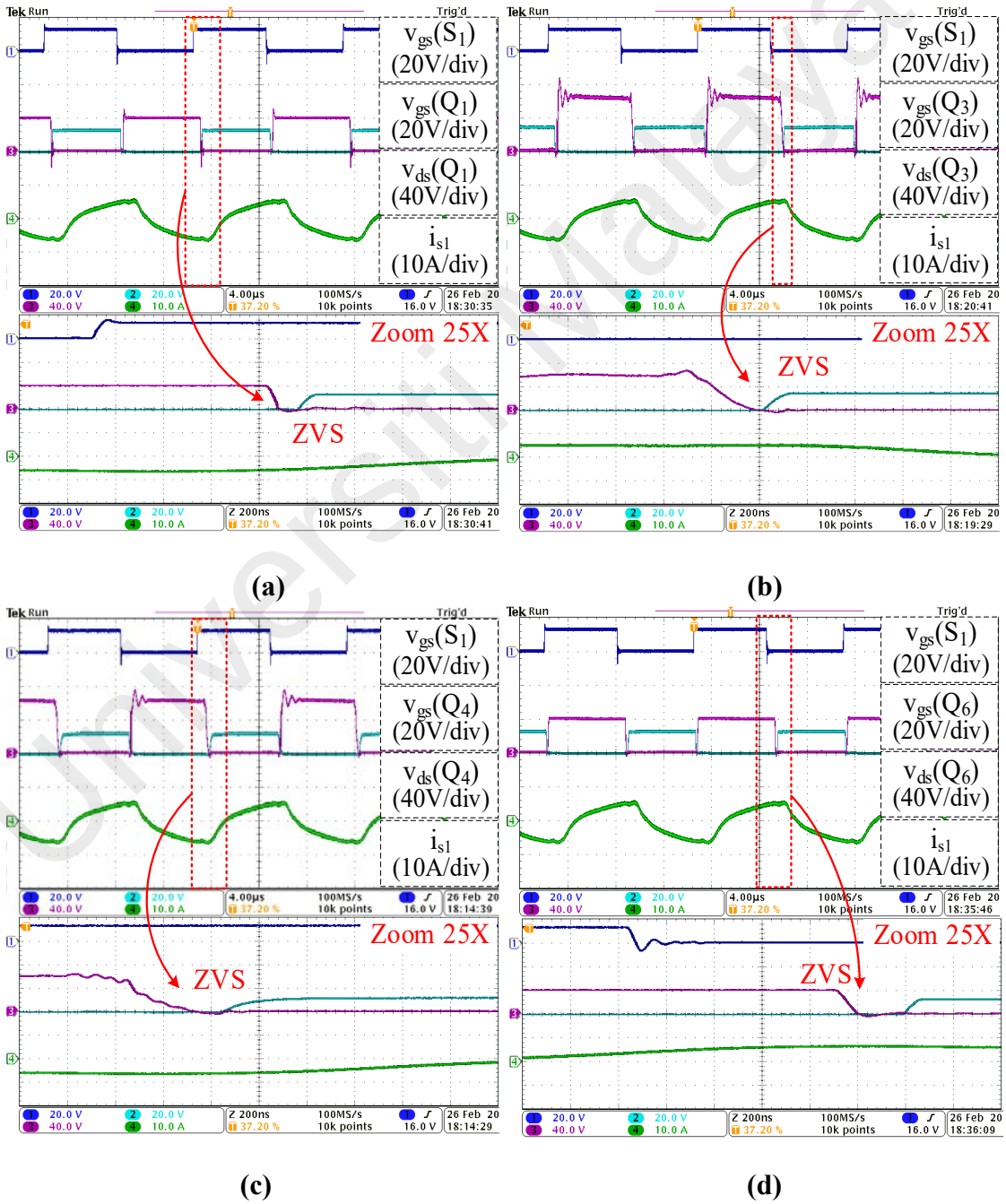

Figure 5.12 Experimental waveforms of the secondary MOSFETs at full load for V_{in} = 400V and V_o = 80V (a) Q_1, (b) Q_3, (c) Q_4, and (d) Q_6

Figure 5.12 and Figure 5.13 presents the ZVS turn-on of the secondary switches for full input voltage for different loading conditions. The V_{ds} waveform does not depict any significant voltage spikes across the switch, which implies the ZVS turn-on operation. The experimental waveforms verify the ZVS operation of the secondary MOSFETs for different load and input conditions.

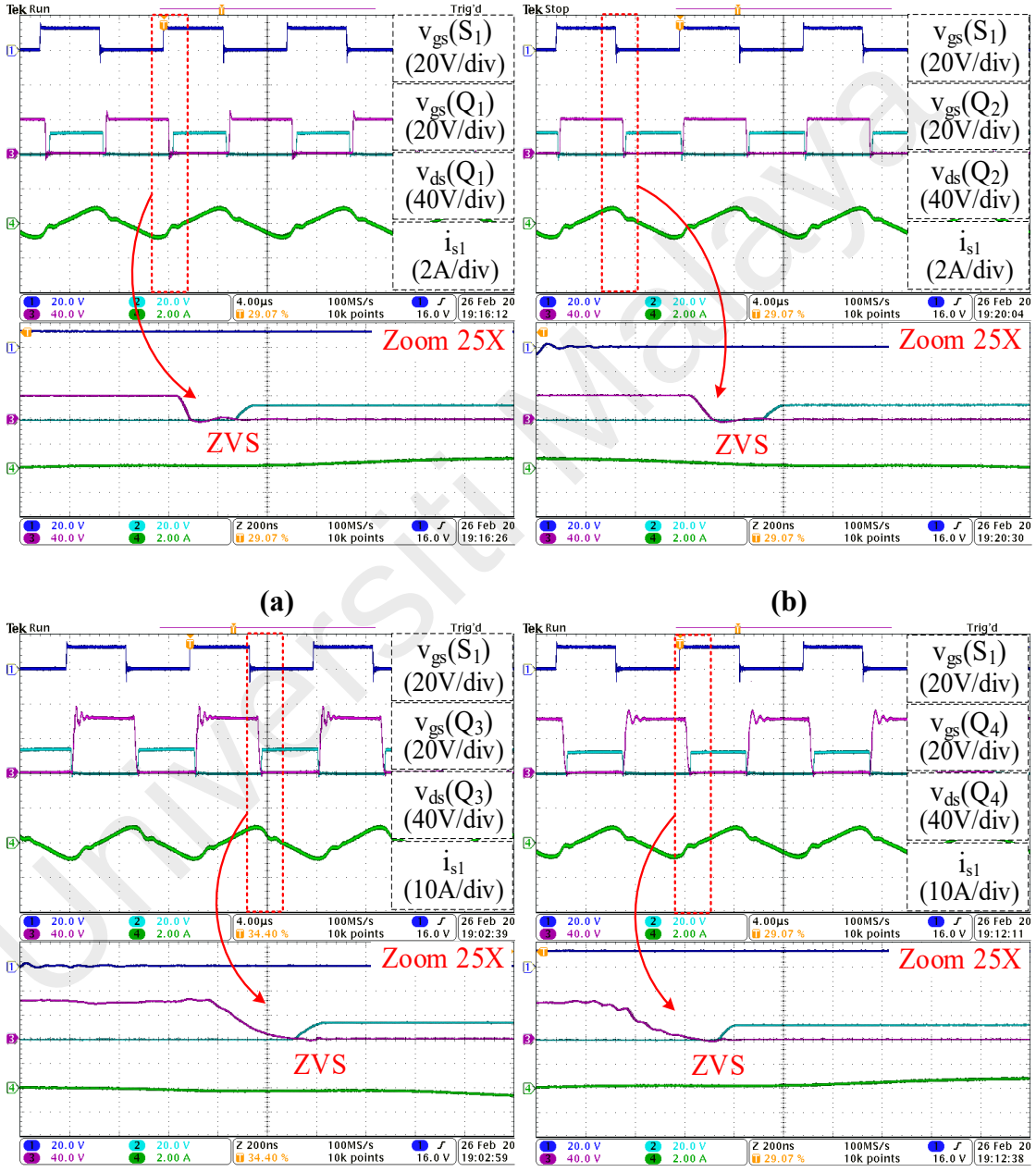

Figure 5.13 Experimental waveforms of the secondary MOSFETs at 20% load for V_{in} = 400V and V_o = 80V (a) Q_1, (b) Q_2, (c) Q_3, and (d) Q_4

5.5 Power Loss Distribution

Using the mathematical formulas based on the loss model, as mentioned in Chapter 4, the power loss distribution of the proposed converter has been explained and compared with the conventional FB LLC resonant converter. The calculated power loss for both the converters for rated voltage and load conditions is drawn in Figure 5.14.

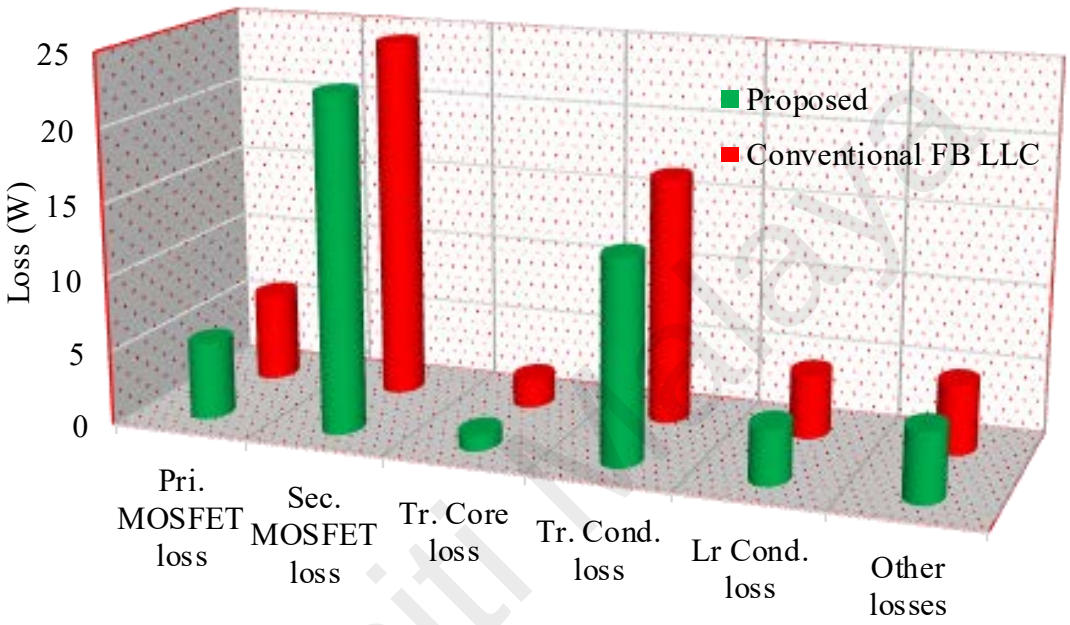

Figure 5.14 Power loss comparison between the proposed converter and the conventional FB LLC converter

A variety of smaller losses such as gate driver circuity loss, ESR loss in the capacitor, wire losses, PCB losses have been clubbed together as other losses. As shown, the loss distribution comprises primary MOSFET losses, secondary MOSFET losses, transformer core loss, transformer conduction loss, inductor conduction loss, and other losses. It can be seen that the conduction losses in primary and secondary are the dominant power losses. The transformer conduction loss also constitutes a major portion of the loss distribution. The primary, as well as secondary MOSFET losses are less than the conventional FB losses owing to ZVS, and the turn-off transition switching losses are reduced to a very small value. The extra losses in conventional FB LLC occur due to non-full ZVS characteristics. The transformer core losses depend upon the volume of the

transformer core. The higher transformer conduction losses occur pertaining to the higher number of winding turns. As it is quite hard to determine the other losses for the conventional FB LLC without a real prototype, the other losses have been considered identical for both the converters. Hence, the power loss of conventional FB LLC is more than the proposed dual-phase LLC resonant converter under rated load conditions.

5.6 Efficiency

Figure 5.15 shows the overall efficiency curve of the proposed dual-phase LLC resonant converter at maximum and minimum input voltage for different load conditions. A higher efficiency is observed over the entire load range for maximum input voltage owing to reduced MOSFET conduction losses and turn-on losses. The efficiency at 210 V input is degraded because of the larger RMS current causing increased conduction losses in the converter. However, as can be observed, the proposed converter is operated at high efficiency for the wide input and load range conditions. Moreover, for the peak input voltage, the efficiency variation is narrow over the entire load range.

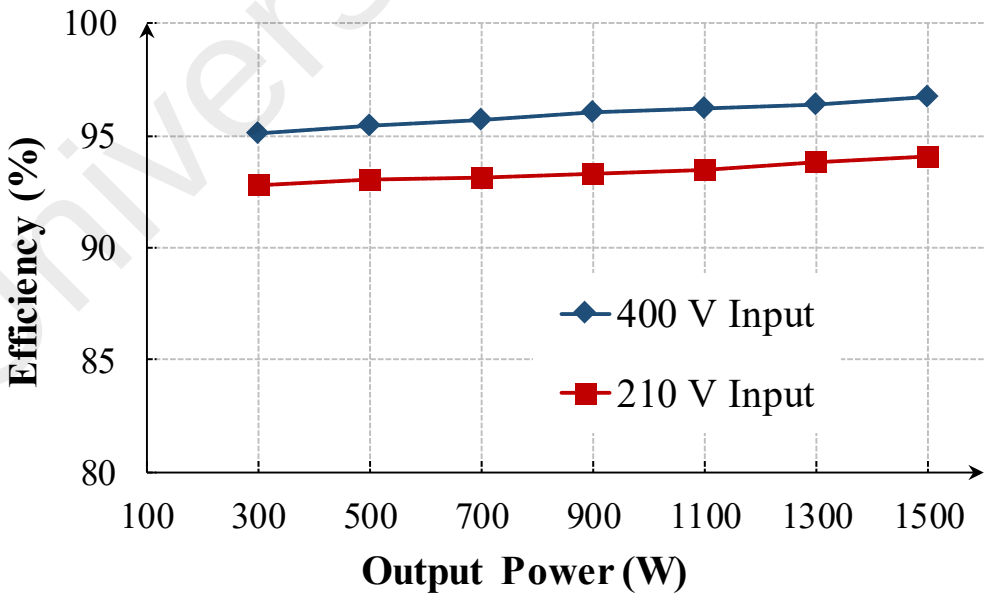

Figure 5.15 Efficiency curve of the proposed LLC converter

5.7 Comparative Discussion

This section discusses a variety of comparisons based on steady-state control parameter values, performance comparison with a dual-phase LLC resonant converter with two parallel FBs, a parameter and components comparison with conventional FB LLC, and an improved FB LLC converter followed a cost comparison based on topology employed.

To validate the steady-state analysis, all the important angles, switching frequency values, and duty ratios for different input and load values have been summarized in Table 5.1.

The double-phase LLC resonant converter has been used for high power applications. The two HBs (G. Yang et al., 2015a) and two FBs have been employed to generate dual-phase. Figure 5.16 represents a dual-phase LLC resonant converter with two parallel FBs. The proposed converter and the converter in Figure 5.16 are more suitable for high power applications with high input voltages. In order to present a fair comparison, both converters are simulated with identical parameters, i.e. V_{in} = 210-400V, V_0 = 80V, L_r =

Table 5.1: Steady-State Parameters for Different Input and Load Conditions

V_{in}	Q	F_s	Φ		θ	D
400V	Full load Q=2.8	F=1.061	Th	18.9˚	5.33	0.47
			Ex	19.8˚	6.36˚	0.465
400V	20% load Q=0.56	F=1.341	Th	18.9˚	8.9˚	0.451
			Ex	19.8˚	9.2˚	0.449
210V	Full load Q=2.8	F= 1.061	Th	77˚	35.52˚	0.303
			Ex	79˚	36.9˚	0.295
210V	20% load Q=0.56	F=1.341	Th	77˚	35.86˚	0.3
			Ex	79˚	37.15˚	0.294

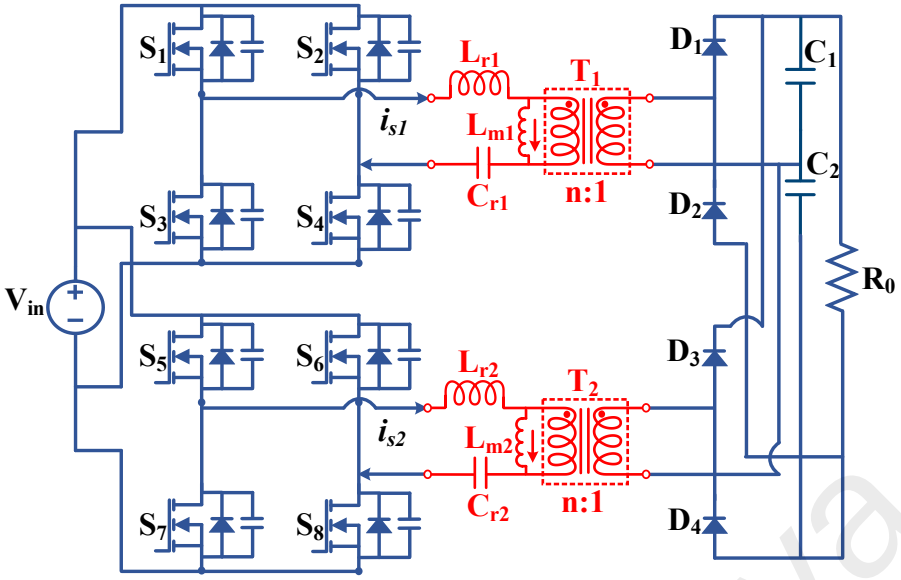

Figure 5.16 Dual-phase LLC resonant converter

362.52µH, C_r = 12.41nF, and f_s = 75kHz. In the proposed converter, the turn ratio is 21:5, however for the desired operation, the dual-phase LLC converter has a transformer turn ratio of 21:4. The topology arrangement in the proposed converter along with improved modulation benefits in voltage gain range and ZVS range. Hence, the magnetizing inductance is 423.5µH. For dual-phase, the magnetizing inductance is 250µH.

The two converters have identical power semiconductor device counts. However, in dual-phase LLC, all the primary switches are stressed to the full input voltage, whereas, in the proposed work, only two switches are full input voltage stressed. The simulation results have been summarized in Table 5.2 for both the converters at different input voltage conditions.

As seen, the desired voltage gain range in dual-phase LLC converter results in the frequency range of 40-80 kHz for the changing input voltage conditions. However, the proposed converter employs phase shift, and frequency remains constant for any input voltage change. Moreover, the switching frequency range is 80-100 kHz for selected load values. The transformer design concerns with flux density change (ΔB), and it should be

Table 5.2 Performance Comparison

	Dual Phase LLC(1.5 kW)		Proposed Converter(1.5 kW)	
V_{in} (V)	210	400	210	400
f_s (kHz)	40	80.5	80	80
$V_{ds,peak}$ (V)	210	400	105	200
ΔB (T)	0.4	0.2	0.2	0.2
$I_{s1,\,rms}$ (A)	4.1	2.56	4.8	3.3
$S_{1\text{-}6}$ turn off current (A)	4.8	3.0	3.1	3.3

small to avoid core saturation. The dual-phase LLC exhibits a large change in ΔB and to limit ΔB, and it could result in an increased number of primary turns (n_p) or core cross-sectional area (A_e) for a particular volt-second value (λ). Hence, the transformer size increases to mitigate the flux change in the dual-phase LLC converter. The comparison of $I_{s1,RMS}$ at different input voltage value signifies that the dual-phase LLC converter suffers from higher conduction losses compared to the proposed converter. Moreover, the turn-off current of S_1-S_4 (S_5-S_8) in a dual-phase LLC converter largely depends on input voltage and load conditions. This could result in ZVS loss for the switches when f_s and f_r deviate under light load and minimum input condition. Nonetheless, the proposed modulation results in voltage gain independent of load conditions. Hence, the turn-off current in the proposed converter does not vary large and provides better ZVS performance than the dual-phase LLC converter.

As discussed earlier in the literature review, a number of topologies and their control have been proposed to enhance the LLC resonant converter performance. An overview performance assessment on the basis of switch counts, the number of transformers, gain range, ZVS range, etc. have been done of some topologies with the proposed converter. A detailed feature analysis is summarized in Table 5.3. The work in (G. Yang et al., 2015b) proposed a dual-phase parallel arrangement of LLC resonant tank employing synchronous rectification on the secondary side. An interleaved boost-integrated LLC

converter has been proposed in (X. Sun et al., 2015). The converter gain range is very wide, which employs fixed-frequency PWM control. Nevertheless, the converter has limited ZVS capability pertaining to boost the operation of phase-shifted primary switches. In (Wu, Zhan, et al., 2017), the conventional LLC converter is controlled with a proposed Asymmetric PWM (APWM) for hold-up time operation. The converter has a wide voltage gain range; however, the modulation causes a large DC current through magnetic inductance. This inhibits the ZVS achievement for one of the primary MOSFET. An integration of HB LLC and FB LLC has been proposed in (X. Sun et al., 2017) utilizing an auxiliary bidirectional switch. The converter is PWM controlled, resulting in varied time duration of HB or FB operation in any switching cycle. With an increase in HB pulse width, the magnetizing current decreases causing the ZVS capability

Table 5.3 An Overview Comparison of the Proposed Converter with Other Recent Topologies

Topologies	**G. Yang et al., 2015**	**C. Li et al., 2020**	**Karthikeyan et al., 2018**	**Jiang et al., 2016**	**Shakib & Mekhilef, 2017**	**Proposed**
MOSFETs	8	5	10	12	6	**12**
Diodes	0	4	0	0	0	**0**
Transformer	2	2	1	1	1	**2**
Filter capacitors	1	3	1	4	3	**1**
Modulation	PWM	PFM	DPS	PWAM	FAPSM	**VF-PSM**
Gain range (with load)	Medium dependent	Wide	Narrow/ dependent	Wide	Wide independent	**Wide independent**
ZVS performance	Good	Excellent	Good	Medium	Excellent	**Excellent**
Reverse power flow control	No	No	No	No	Yes	**Yes**
Input	330-410V	390V	60V	240-480V	200-400V	**210-400V**
Output	14 V 2.5 kW	80-450 V 1 kW	13.5 V 350 W	30-60V 1kW	48V 1 kW	**80 V 1.5 kW**
Peak efficiency	95%	97.01%	96.3%	96.5%	96.4%	**96.7%**

of the converter to medium range. A three-level LLC resonant converter with pulse width and amplitude modulation (PWAM) has been discussed in (Jiang et al., 2016). The converter exhibits an extremely wide voltage gain range. The ZVS capability of the converter is limited to medium range with the proposed modulation scheme. In (Shakib & Mekhilef, 2017), a stacked HB LLC converter is proposed with a novel frequency adaptive phase shift modulation. The converter has a wide gain range with excellent ZVS capability of the primary as well as secondary switches. However, the limitation of reactive power needs a larger magnetizing inductance, which in turn limits the ZVS range of secondary switches. The work in (W. Sun et al., 2018) proposes a modified LLC resonant converter resulting in two resonant tanks with a hybrid phase-shift control. The voltage gain range is wide with good ZVS capability in primary switches. However, the transition between medium and high gain range requires excellent control, which is complex and dependent on system parameters. The detailed features of the proposed converter are mentioned in the last column of Table 5.3. The voltage stress of the primary switches is clamped to half of the input voltage. The converter achieves a wide voltage gain range, which is independent of load. However, the reactive power (circulating power flow) on the output side is zero making the converter operation efficient at light-load conditions. Hence, the proposed work can be suitable for high-power, wide input-voltage range applications.

Moreover, the parameter and component comparison of the proposed topology has been made with conventional FB LLC (Dos Santos et al., 2011) and an improved FB LLC (W. Sun et al., 2017) in Table 5.4. The detailed parameters of the three converters have been summarized in the table following the design procedure, as discussed in (X. Li, 2014). As seen, the resonant capacitor in the proposed topology is larger than the others; however its peak voltage as calculated for same values of resonant current is much smaller. This results in smaller volume of resonant capacitor. Secondly, although the

Table 5.4 Components and Parameters comparison of the proposed converters

Parameters or Components	Conventional FB *LLC* (Dos Santos et al., 2011)	Improved FB *LLC* (W. Sun et al., 2017)	Proposed Dual phase LLC
Turn-ratio n_e, n_1, n_2	4.2, -, -	4.2, 3, 1.2	**4.2, 2.1, 2.1**
Inductance ratio k	0.586	0.323 (L_r/L_m), 0.465 (L_r/L_{m1})	**0.428**
Resonant Inductance L_r, L_{r1}, L_{r2}	827.49 µH, n/a, n/a	710.6 µH, n/a, n/a	**362.52µH, 181.26µH, 181.26 µH**
Magnetizing Inductance L_m, L_{m1}, L_{m2}	1.41 mH, n/a, n/a	2.2 mH, 1.53 mH, 670 µH	**847 µH, 423.5 423.5 µH**
Peak magnetizing current at $f_s=f_r$	0.46A	0.22A	**0.38A**
Core of transformers T, T_1, T_2	PC95PQ50/50*2pc (Ap=13cm^4), n/a, n/a	n/a, PC95EE42/15 (Ap=9.7cm^4), PC95PQ40/40(Ap=6.6cm^4)	**n/a, PC95PQ40/40(Ap=6.6cm^4), PC95PQ40/40 (Ap=6.6cm^4)**
Resonant Capacitor C_r ,C_{r1},C_{r2}	5.45 nF, n/a, n/a	6.34nF, n/a, n/a	**12.41nF, 24.82nF, 24.82nF**
Peak voltage of C_r	1050V	880V	**450 V**
Primary switch	SPW35N60C3* 4pcs	SPW35N60C3* 4pcs+ IPP600N25N3G*2 pcs	**IPP600N25N3G *4pcs+ SPW35N60C3*2pcs**
Secondary diode/switch	IPP200N15N3G *4pcs	STPS61150C *8pcs	**IPP200N15N3G *6pcs**
Device Count	Least	Most	**Less**
Power density	High	Low	**Medium**

primary bridge has been modified, the ZVS range of conventional LLC DAB is well preserved and extended using the improved modulation scheme. For transformer sizing, the comparison of area product and volume can be done for the three converters. Moreover, the component counts of the proposed converter is more than conventional FB LLC and lesser than the improved FB LLC. However, the voltage stress comparison on

Table 5.5 Cost comparison of the proposed converter with the other converters for topology configuration

Component	Part Number	Rating	Unit Price ($)	Conventional FB LLC (Dos Santos et al., 2011)	Improved FB LLC (W. Sun et al., 2017)	**Proposed**
MOSFET*	Primary SPW35N60C3 IPP600N25N3G	650V, 35A 250V, 25A	9.53 2.68	4 -	4 2	**2** **4**
	Secondary IPP200N15N3G	150V, 50A	2.75	4	-	**6**
Diode*	STPS61150C	150V, 60A	4.11	-	8	**-**
Total cost ($)				49.12	76.36	**46.28**

*digikey.com

the switches of the three topologies results in cost comparison based on topology configuration.

To further highlight the merits of the proposed topology, a cost comparison has been considered and presented in Table 5.5. For the cost comparison, identical voltage parameters have been used for all topologies. From the resultant cost given in Table 5.5, the proposed topology gives the minimum cost as compared to all other topologies.

5.8 Summary

This chapter presents the validation of theoretical analysis through the simulation and experimental results. The designed dual-phase LLC resonant converter with the improved modulation scheme has provided worthy improvement in the efficiency of the converter as a result of reduced switching and conduction losses. Although the component counts are higher than the conventional FB resonant converter, the eliminated reactive power flow from the proposed converter gives higher efficiency.

CHAPTER 6: CONCLUSION AND FUTURE WORK

6.1 Conclusion

A novel dual phase LLC resonant converter employing an improved variable frequency zero circulating current phase shift modulation is presented in this study. The operation principle and detailed analysis are presented. The proposed six switch H-bridge on the inverter side generates two square voltage waveform for the dual LLC resonant tank. In the proposed topology, the peak voltage stress equal to the input voltage is only limited to two switches, whereas the other four switches are stressed to half of the input voltage. Hence, the bridge configuration enables the converter to be operated at higher power ratings. The half–input voltage stress enables the usage of the low voltage rating of power MOSFETs (low $R_{ds\text{-}on}$), which reduces the conduction losses in the converter. The improved modulation scheme overcomes the narrow gain limitation of the conventional FB LLC resonant converter. The converter gain becomes independent of load and inductor ratio values because of the two independent control variables (f_s and ϕ). The limited switching frequency range minimizes the complexity of parameter design. The chosen value of magnetizing inductance increases the ZVS range. Furthermore, the elimination of circulating current at all conditions, especially at light load conditions, results in improved performance of the converter as compared to the conventional FB LLC converter. The performance of the proposed converter with the modulation scheme has been verified by a designed 210-400V input, 80V, and 1.5 kW output prototype. The experimental results validate the theoretical and simulation findings. The converter achieves ZVS for the wide input and load range, thereby reducing the switching losses and providing an efficient prototype converter. The efficiency of the proposed converter at the rated load condition is 96.7 % and 94.1 % for maximum and minimum input voltage, respectively. These attractive features make the proposed converter a suitable choice for a wide input voltage range in medium/high power applications.

6.2 Future Work

Though this proposed DC / DC converter meets the research objectives, further study is needed on several issues. Some recommendations are outlined below for future studies:

- For the proposed topology, the series-connected MOSFETs result in unequal voltage stress distribution and would require individual voltage balancing circuits to achieve equal voltage stress among the switches. This could be further explored with added auxiliary circuits to achieve static as well as dynamic voltage balance among the switches.
- For high power converters such as single-phase DAB and three-phase DAB LLC resonant converters, which tend to be more desirable and efficient due to their low current stress in power semiconductor switches, resulting in low power losses, the proposed control scheme could be implemented. It could also be incorporated into bi-directional converters for multiport DB LLC.
- In order to increase the power density and efficiency further, resonant DC-DC power converters with new material-based ultra-high-frequency switching devices such as GaN-HEMT and SiC could be effectively implemented.
- It is possible to investigate further the voltage / current stresses on the converter components and their relationships with control variables and resonant tank parameters. In order to improve performance, the reverse energy and component stresses will, therefore, be reduced in the high gain mode.
- In the resonance current, especially under the light load state, all parasitic LC components of the converter circuit elements such as the HF transformer could be modelled to minimize the high-frequency ripple. Throughout the study, the model with all parasitic LC components could be used to achieve smoother operations that will offer greater precision and better performance.

REFERENCES

Bhat, A K S. (1993). Analysis and design of a series-parallel resonant converter. *IEEE Transactions on Power Electronics*, *8*(1), 1–11.

Bhat, Ashoka K.S. (1994). Analysis and Design of LCL-Type Series Resonant Converter. *IEEE Transactions on Industrial Electronics*, *41*(1), 118–124.

Bose, B. K. (2013). Global Energy Scenario and Impact of Power Electronics in 21st Century. *IEEE Transactions on Industrial Electronics*, *60*(7), 2638–2651.

Caricchi, F., Crescimbini, F., Noia, G., & Pirolo, D. (1994). Experimental study of a bidirectional dc-dc converter for the dc link voltage control and the regenerative braking in PM motor drives devoted to electrical vehicles. *Conference Proceedings - IEEE Applied Power Electronics Conference and Exposition - APEC*, *1*, 381–386.

Chen, W., Rong, P., & Lu, Z. (2010). Snubberless Bidirectional DC–DC Converter With New CLLC Resonant Tank Featuring Minimized Switching Loss. *IEEE Transactions on Industrial Electronics*, *57*(9), 3075–3086.

Choi, H. (2007). Analysis and design of LLC resonant converter with integrated transformer. *Conference Proceedings - IEEE Applied Power Electronics Conference and Exposition - APEC*, 1630–1635.

Chub, A., Vinnikov, D., Kosenko, R., Liivik, E., & Galkin, I. (2020). Bidirectional DC–DC Converter for Modular Residential Battery Energy Storage Systems. *IEEE Transactions on Industrial Electronics*, *67*(3), 1944–1955.

Chung, H. S., Ioinovici, A., & Cheung, W.-L. (2003). Generalized structure of Bi-directional switched-capacitor DC/DC converters. *IEEE Transactions on Circuits and Systems I: Fundamental Theory and Applications*, *50*(6), 743–753.

Cuk, S. (1983). A new zero-ripple switching DC-to-DC converter and integrated magnetics. *IEEE Transactions on Magnetics*, *19*(2), 57–75.

Das, P., Mousavi, S. A., & Moschopoulos, G. (2010). Analysis and design of a nonisolated bidirectional ZVS-PWM DC-DC converter with coupled inductors. *IEEE Transactions on Power Electronics*, *25*(10), 2630–2641.

De Doncker, R. W. A. A., Divan, D. M., & Kheraluwala, M. H. (1991). A three-phase soft-switched high-power-density DC/DC converter for high-power applications. *IEEE Transactions on Industry Applications*, *27*(1), 63–73.

De Souza, E. V., & Barbi, I. (2011). Bidirectional current-fed flyback-push-pull DC-DC converter. *COBEP 2011 - 11th Brazilian Power Electronics Conference*, 8–13.

Delshad, M., & Farzanehfard, H. (2010). A new isolated bidirectional buck-boost PWM converter. *PEDSTC 2010 - 1st Power Electronics and Drive Systems and Technologies Conference*, 41–45.

Dos Santos, W. M., Ortmann, M. S., Schweitzer, R., Mussa, S. A., & Martins, D. C.

(2011). Design and conception of a DAB converter (Dual Active Bridge) using the gyrators theory. *COBEP 2011 - 11th Brazilian Power Electronics Conference*, 359–364.

Engel, S. P., Soltau, N., Stagge, H., & De Doncker, R. W. (2013). Dynamic and balanced control of three-phase high-power dual-active bridge DC-DC converters in DC-grid applications. *IEEE Transactions on Power Electronics*, *28*(4), 1880–1889.

Fang, X., Hu, H., Shen, Z. J., & Batarseh, I. (2012). Operation mode analysis and peak gain approximation of the LLC resonant converter. *IEEE Transactions on Power Electronics*, *27*(4), 1985–1995.

Gorji, S. A., Ektesabi, M., & Zheng, J. (2017). Isolated switched-boost push–pull DC–DC converter for step-up applications. *Electronics Letters*, *53*(3), 177–179.

Guarnieri, M., Liserre, M., Sauter, T., & Hung, J. Y. (2010). Future energy systems: Integrating renewable energy sources into the smart power grid through industrial electronics. *IEEE Industrial Electronics Magazine*, *4*(1), 18–37.

Harrould-Kolieb, E. R. (2019). (Re)Framing ocean acidification in the context of the United Nations Framework Convention on climate change (UNFCCC) and Paris Agreement. *Climate Policy*, 1–14.

Harrye, Y. A., Ahmed, K. . H., Adam, G. . P., & Aboushady, A. . A. (2014). Comprehensive steady state analysis of bidirectional dual active bridge DC/DC converter using triple phase shift control. *IEEE International Symposium on Industrial Electronics*, 437–442.

He, P., & Khaligh, A. (2017). Comprehensive Analyses and Comparison of 1 kW Isolated DC–DC Converters for Bidirectional EV Charging Systems. *IEEE Transactions on Transportation Electrification*, *3*(1), 147–156.

Hu, K. W., & Liaw, C. M. (2016). Incorporated operation control of DC microgrid and electric vehicle. *IEEE Transactions on Industrial Electronics*, *63*(1), 202–215.

Hua Bai, & Mi, C. (2008). Eliminate Reactive Power and Increase System Efficiency of Isolated Bidirectional Dual-Active-Bridge DC–DC Converters Using Novel Dual-Phase-Shift Control. *IEEE Transactions on Power Electronics*, *23*(6), 2905–2914.

Huang, A. Q., Crow, M. L., Heydt, G. T., Zheng, J. P., & Dale, S. J. (2011). The future renewable electric energy delivery and management (FREEDM) system: The energy internet. *Proceedings of the IEEE*, *99*(1), 133–148.

Jiang, T., Zhang, J., Wu, X., Sheng, K., & Wang, Y. (2016). A bidirectional three-level LLC resonant converter with PWAM control. *IEEE Transactions on Power Electronics*, *31*(3), 2213–2225.

Jin, C., Wang, P., Xiao, J., Tang, Y., & Choo, F. H. (2014). Implementation of hierarchical control in DC microgrids. *IEEE Transactions on Industrial Electronics*, *61*(8), 4032–4042.

Jin, K., Ruan, X., Yang, M., & Xu, M. (2009). A hybrid fuel cell power system. *IEEE*

Transactions on Industrial Electronics, *56*(4), 1212–1222.

Jung, J.-H. H., Kim, H.-S. S., Ryu, M.-H. H., & Baek, J.-W. W. (2013). Design methodology of bidirectional CLLC resonant converter for high-frequency isolation of DC distribution systems. *IEEE Transactions on Power Electronics*, *28*(4), 1741–1755.

Kakigano, H., Miura, Y., Ise, T., & Uchida, R. (2007). DC voltage control of the dc micro-grid for super high quality distribution. *Fourth Power Conversion Conference-NAGOYA, PCC-NAGOYA 2007 - Conference Proceedings*, 518–525.

Karthikeyan, V., & Gupta, R. (2016). *Zero circulating current modulation for isolated bidirectional dual-active-bridge DC – DC converter*. 1553–1561.

Karthikeyan, V., & Gupta, R. (2018). FRS-DAB Converter for Elimination of Circulation Power Flow at Input and Output Ends. *IEEE Transactions on Industrial Electronics*, *65*(3), 2135–2144.

Khalil-Abaker, M., Shi, J., & Kalam, A. (2016). Design of a 100W bi-directional LCC series-parallel resonant DC-DC converter. In *2016 Australasian Universities Power Engineering Conference (AUPEC)*. IEEE, 1-5.

Kheraluwala, M. N., Gascoigne, R. W., Divan, D. M., & Baumann, E. D. (1992). Performance characterization of a high-power dual active bridge DC-to-DC converter. *IEEE Transactions on Industry Applications*, *28*(6), 1294–1301.

Khodabakhshian, M., Adib, E., & Farzanehfard, H. (2016). Forward-type resonant bidirectional DC–DC converter. *IET Power Electronics*, *9*(8), 1753–1760.

Krismer, F, & Kolar, J. W. (2010). Accurate Power Loss Model Derivation of a High-Current Dual Active Bridge Converter for an Automotive Application. *IEEE Transactions on Industrial Electronics*, *57*(3), 881–891.

Krismer, Florian, & Kolar, J. W. (2012). Efficiency-optimized high-current dual active bridge converter for automotive applications. *IEEE Transactions on Industrial Electronics*, *59*(7), 2745–2760.

Kwon, M., Park, J., & Choi, S. (2016). A Bidirectional Three-Phase Push–Pull Converter With Dual Asymmetrical PWM Method. *IEEE Transactions on Power Electronics*, *31*(3), 1887–1895.

Lee, H.-S., & Yun, J.-J. (2019). High-Efficiency Bidirectional Buck–Boost Converter for Photovoltaic and Energy Storage Systems in a Smart Grid. *IEEE Transactions on Power Electronics*, *34*(5), 4316–4328.

Li, H., Peng, F. Z., & Lawler, J. S. (2003). A natural ZVS medium-power bidirectional DC-DC converter with minimum number of devices. *IEEE Transactions on Industry Applications*, *39*(2), 525–535.

Li, X. (2014b). A LLC-Type Dual-Bridge Resonant Converter: Analysis, Design, Simulation, and Experimental Results. *IEEE Transactions on Power Electronics*, *29*(8), 4313–4321.

Li, X., & Bhat, A. K. S. (2010). Analysis and Design of High-Frequency Isolated Dual-Bridge Series Resonant DC/DC Converter. *IEEE Transactions on Power Electronics*, *25*(4), 850–862.

Li, Y., Sun, Q., Dong, T., & Zhang, Z. (2018). Energy management strategy of AC/DC hybrid microgrid based on power electronic transformer. *Proceedings of the 13th IEEE Conference on Industrial Electronics and Applications, ICIEA 2018*, 2677–2682.

Li, Z., Xue, B., & Wang, H. (2020). An Interleaved Secondary-Side Modulated LLC Resonant Converter for Wide Output Range Applications. *IEEE Transactions on Industrial Electronics*, *67*(2), 1124–1135.

Liang, Y., Liu, W., Lu, B., & Van Wyk, J. D. (2005). Design of integrated passive component for a 1MHz 1kW half-bridge LLC resonant converter. *Conference Record - IAS Annual Meeting (IEEE Industry Applications Society)*, *3*, 2223–2228.

Lin, B. R., Chen, J. J., Lee, Y. E., & Chiang, H. K. (2008). Analysis and implementation of a bidirectional ZVS DC-DC converter with active clamp. *2008 3rd IEEE Conference on Industrial Electronics and Applications, ICIEA 2008*, 382–387.

Lin, C. C., Yang, L. S., & Wu, G. W. (2013). Study of a non-isolated bidirectional DC-DC converter. *IET Power Electronics*, *6*(1), 30–37.

Madawala, U. K., & Thrimawithana, D. J. (2011). A bidirectional inductive power interface for electric vehicles in V2G systems. *IEEE Transactions on Industrial Electronics*, *58*(10), 4789–4796.

Majo, J., Martinez, L., Poveda, A., de Vicuna, L. G., Guinjoan, F., Sanchez, A. F., Valentin, M., & Marpinard, J. C. (1992). Large-signal feedback control of a bidirectional coupled-inductor Cuk converter. *IEEE Transactions on Industrial Electronics*, *39*(5), 429–436.

Matsuo, H., & Kurokawa, F. (1984). New Solar Cell Power Supply System Using a Boost Type Bidirectional DC-DC Converter. *IEEE Transactions on Industrial Electronics*, *IE-31*(1), 51–55.

Mi, C., Bai, H., Wang, C., Gargies, S., Bai, C. M. H., Gargies, C. W. S., Mi, C., Bai, H., Wang, C., & Gargies, S. (2008). Operation, design and control of dual H-bridge-based isolated bidirectional DC – DC converter. *IET Power Electronics*, *1*(4), 507–517.

Middlebrook, R. D., Cuk, S., & Behen, W. (1978). A new battery charger/discharger converter. *PESC Record - IEEE Annual Power Electronics Specialists Conference*, *1978-January*, 251–255.

Monteiro, V., Pinto, J. G., & Afonso, J. L. (2016). Operation Modes for the Electric Vehicle in Smart Grids and Smart Homes: Present and Proposed Modes. *IEEE Transactions on Vehicular Technology*, *65*(3), 1007–1020.

Morrison, R., & Egan, M. G. (2000). A new power-factor-corrected single-transformer UPS design. *IEEE Transactions on Industry Applications*, *36*(1), 171–179.

Nymand, M., & Andersen, M. A. E. (2010). High-Efficiency Isolated Boost DC–DC Converter for High-Power Low-Voltage Fuel-Cell Applications. *IEEE Transactions on Industrial Electronics*, *57*(2), 505–514.

Outeiro, M. T., Buja, G., & Czarkowski, D. (2016). Resonant Power Converters: An Overview with Multiple Elements in the Resonant Tank Network. *IEEE Industrial Electronics Magazine*, *10*(2), 21–45.

Park, H. P., Kim, M., & Jung, J. H. (2019). Investigation of Zero Voltage Switching Capability for Bidirectional Series Resonant Converter Using Phase-Shift Modulation. *IEEE Transactions on Power Electronics*, *34*(9), 8842–8858.

Park, S., & Song, Y. (2011). An interleaved half-bridge bidirectional dc-dc converter for energy storage system applications. *8th International Conference on Power Electronics - ECCE Asia: "Green World with Power Electronics", ICPE 2011-ECCE Asia*, 2029–2034.

Peng, F. Z., Zhang, F., & Qian, Z. (2002). A magnetic-less dc-dc converter for dual voltage automotive systems. In *Conference Record - IAS Annual Meeting (IEEE Industry Applications Society)* (Vol. 2, pp. 1303–1310). IEEE.

Peng, F. Z., Li, H., Su, G. J., & Lawler, J. S. (2004). A new ZVS bidirectional DC-DC converter for fuel cell and battery application. *IEEE Transactions on Power Electronics*, *19*(1), 54–65.

Phattanasak, M., Gavagsaz-Ghoachani, R., Martin, J.-P., Nahid-Mobarakeh, B., Pierfederici, S., & Davat, B. (2015). Control of a Hybrid Energy Source Comprising a Fuel Cell and Two Storage Devices Using Isolated Three-Port Bidirectional DC–DC Converters. *IEEE Transactions on Industry Applications*, *51*(1), 491–497.

Pistollato, S., Caldognetto, T., Mattavelli, P., & Magnone, P. (2019). Triple-Phase Shift Modulation for Dual Active Bridge based on Simplified Switching Loss Model. In *2019 AEIT International Annual Conference (AEIT)*. IEEE. 1-6.

Rathore, A. K., Patil, D. R., & Srinivasan, D. (2016). Non-isolated Bidirectional Soft-Switching Current-Fed LCL Resonant DC/DC Converter to Interface Energy Storage in DC Microgrid. *IEEE Transactions on Industry Applications*, *52*(2), 1711–1722.

Ruseler, A., & Barbi, I. (2013). Isolated Zeta-SEPIC bidirectional dc-dc converter with active-clamping. In *2013 Brazilian Power Electronics Conference*. IEEE. 123-128.

Sands, P. (1992). The United Nations Framework Convention on Climate Change. *Review of European Community & International Environmental Law*, *1*(3), 270–277.

Sha, D., You, F., & Wang, X. (2016). A High-Efficiency Current-Fed Semi-Dual-Active Bridge DC-DC Converter for Low Input Voltage Applications. *IEEE Transactions on Industrial Electronics*.

Shakib, S. M. S. I., & Mekhilef, S. (2017). A Frequency Adaptive Phase Shift Modulation Control Based LLC Series Resonant Converter for Wide Input Voltage Applications.

IEEE Transactions on Power Electronics, *32*(11), 8360–8370.

Steigerwald, R. L. (1988). A comparison of half-bridge resonant converter topologies. *IEEE Transactions on Power Electronics*, *3*(2), 174–182.

Sun, W., Xing, Y., Wu, H., & Ding, J. (2018). Modified High-Efficiency LLC Converters With Two Split Resonant Branches for Wide Input-Voltage Range Applications. *IEEE Transactions on Power Electronics*, *33*(9), 7867–7879.

Sun, W., Xing, Y., Wu, H., Ding, J., Member, S., Xing, Y., Wu, H., & Ding, J. (2017). Modified High-efficiency LLC Converters with Two Split Resonant Branches for Wide Input-Voltage Range Applications. *IEEE Transactions on Power Electronics*, *8993*(c), 7867–7879.

Sun, X., Li, X., Shen, Y., Wang, B., & Guo, X. (2017). Dual-Bridge LLC Resonant Converter With Fixed-Frequency PWM Control for Wide Input Applications. *IEEE Transactions on Power Electronics*, *32*(1), 69–80.

Sun, X., Shen, Y., Zhu, Y., & Guo, X. (2015). Interleaved Boost-Integrated LLC Resonant Converter With Fixed-Frequency PWM Control for Renewable Energy Generation Applications. *IEEE Transactions on Power Electronics*, *30*(8), 4312–4326.

Tao, H., Kotsopoulos, A., Duarte, J. L., & Hendrix, M. A. M. (2006). Family of multiport bidirectional DC–DC converters. *IEE Proceedings - Electric Power Applications*, *153*(3), 451.

Wang, C.-S., Zhang, S., Wang, Y., Chen, B., & Liu, J. (2019). A 5-kW Isolated High Voltage Conversion Ratio Bidirectional CLTC Resonant DC–DC Converter With Wide Gain Range and High Efficiency. *IEEE Transactions on Power Electronics*, *34*(1), 340–355.

Wang, L., Wang, Z., & Li, H. (2012). Asymmetrical Duty Cycle Control and Decoupled Power Flow Design of a Three-port Bidirectional DC-DC Converter for Fuel Cell Vehicle Application. *IEEE Transactions on Power Electronics*, *27*(2), 891–904.

Wen, H., & Xiao, W. (2013). Bidirectional dual-active-bridge DC-DC converter with triple-phase-shift control. In *Conference Proceedings - IEEE Applied Power Electronics Conference and Exposition - APEC* (pp. 1972–1978). IEEE.

Wilson, J. R., & Burgh, G. (2007). Energizing Our Future: Rational Choices for the 21st Century. In *Energizing Our Future: Rational Choices for the 21st Century*. John Wiley and Sons. 1-390.

Wu, H., Sun, K., Li, Y., & Xing, Y. (2017). Fixed-Frequency PWM-Controlled Bidirectional Current-Fed Soft-Switching Series-Resonant Converter for Energy Storage Applications. *IEEE Transactions on Industrial Electronics*, *64*(8), 6190–6201.

Wu, H., Zhan, X., & Xing, Y. (2017). Interleaved LLC Resonant Converter With Hybrid Rectifier and Variable-Frequency Plus Phase-Shift Control for Wide Output Voltage Range Applications. *IEEE Transactions on Power Electronics*, *32*(6), 4246–4257.

Xiangli, K., Li, S., & Smedley, K. M. (2018). Decoupled PWM Plus Phase-Shift Control for a Dual-Half-Bridge Bidirectional DC–DC Converter. *IEEE Transactions on Power Electronics*, *33*(8), 7203–7213.

Xiao, H., & Xie, S. (2008). A ZVS Bidirectional DC–DC Converter With Phase-Shift Plus PWM Control Scheme. *IEEE Transactions on Power Electronics*, *23*(2), 813–823.

Xiaodong Li, & Bhat, A. K. S. (2010). Analysis and Design of High-Frequency Isolated Dual-Bridge Series Resonant DC/DC Converter. *IEEE Transactions on Power Electronics*, *25*(4), 850–862.

Xu, D., Zhao, C., & Fan, H. (2004). A PWM Plus Phase-Shift Control Bidirectional DC–DC Converter. *IEEE Transactions on Power Electronics*, *19*(3), 666–675.

Xu, X., Khambadkone, A. M., & Oruganti, R. (2007). A soft-switched back-to-back bi-directional DC/DC converter with a FPGA based digital control for automotive applications. In *IECON Proceedings (Industrial Electronics Conference)* (pp. 262–267). IEEE.

Yang, B., Chen, R., & Lee, F. C. (2002). Integrated magnetic for LLC resonant converter. In *Conference Proceedings - IEEE Applied Power Electronics Conference and Exposition - APEC* (Vol. 1, pp. 346–351). IEEE.

Yang, G., Dubus, P., & Sadarnac, D. (2015a). Double-Phase High-Efficiency, Wide Load Range High- Voltage/Low-Voltage DC/DC Converter for Electric/Hybrid Vehicles. *IEEE Transactions on Power Electronics*, *30*(4), 1876–1886.

Yang, G., Dubus, P., & Sadarnac, D. (2015b). Double-Phase High-Efficiency, Wide Load Range High- Voltage/Low-Voltage LLC DC/DC Converter for Electric/Hybrid Vehicles. *IEEE Transactions on Power Electronics*, *30*(4), 1876–1886.

Yang, R., Ding, H., Xu, Y., Yao, L., & Xiang, Y. (2014). An Analytical Steady-State Model of LCC type Series–Parallel Resonant Converter With Capacitive Output Filter. *IEEE Transactions on Power Electronics*, *29*(1), 328–338.

Yaqoob, M., Loo, K. H., & Lai, Y. M. (2017). Extension of Soft-Switching Region of Dual-Active-Bridge Converter by a Tunable Resonant Tank. *IEEE Transactions on Power Electronics*, *32*(12), 9093–9104.

Yaqoob, Muhammad, Loo, K. H., & Lai, Y. M. (2019). A Four-Degrees-of-Freedom Modulation Strategy for Dual-Active-Bridge Series-Resonant Converter Designed for Total Loss Minimization. *IEEE Transactions on Power Electronics*, *34*(2), 1065–1081.

Zhang, F., & Yan, Y. (2009). Novel Forward–Flyback Hybrid Bidirectional DC–DC Converter. *IEEE Transactions on Industrial Electronics*, *56*(5), 1578–1584.

Zhang, J., Lai, J.-S., Kim, R.-Y., & Yu, W. (2007). High-Power Density Design of a Soft-Switching High-Power Bidirectional dc–dc Converter. *IEEE Transactions on Power Electronics*, *22*(4), 1145–1153.

Zhang, Z., Thomsen, O. C., & Andersen, M. A. E. (2012). Optimal Design of a Push-Pull-Forward Half-Bridge (PPFHB) Bidirectional DC–DC Converter With Variable Input Voltage. *IEEE Transactions on Industrial Electronics*, *59*(7), 2761–2771.

Zhang, Z., Thomsen, O. C., Andersen, M. A. E. E., Schmidt, J. D., & Nielsen, H. R. (2009). Analysis and design of bi-directional DC-DC converter in extended run time DC UPS system based on fuel cell and supercapacitor. *Conference Proceedings - IEEE Applied Power Electronics Conference and Exposition - APEC*, 714–719.

Zhao, B., Song, Q., & Liu, W. (2013). Efficiency characterization and optimization of isolated bidirectional DC-DC converter based on dual-phase-shift control for DC distribution application. *IEEE Transactions on Power Electronics*, *28*(4), 1711–1727.

Zhao, B., Song, Q., Liu, W., Liu, G., & Zhao, Y. (2015). Universal High-Frequency-Link Characterization and Practical Fundamental-Optimal Strategy for Dual-Active-Bridge DC-DC Converter under PWM Plus Phase-Shift Control. *IEEE Transactions on Power Electronics*, *30*(12), 6488–6494.

Zhao, B., Song, Q., Liu, W., & Sun, W. (2013). Current-Stress-Optimized Switching Strategy of Isolated Bidirectional DC–DC Converter With Dual-Phase-Shift Control. *IEEE Transactions on Industrial Electronics*, *60*(10), 4458–4467.

Zhao, B., Song, Q., Liu, W., & Sun, Y. (2014). Overview of Dual-Active-Bridge Isolated Bidirectional DC–DC Converter for High-Frequency-Link Power-Conversion System. *IEEE Transactions on Power Electronics*, *29*(8), 4091–4106.

Zhao, B., Yu, Q., & Sun, W. (2012). Extended-phase-shift control of isolated bidirectional DC-DC converter for power distribution in microgrid. *IEEE Transactions on Power Electronics*, *27*(11), 4667–4680.

Zhao, C., Round, S. D., & Kolar, J. W. (2008). An Isolated Three-Port Bidirectional DC-DC Converter With Decoupled Power Flow Management. *IEEE Transactions on Power Electronics*, *23*(5), 2443–2453.

LIST OF PUBLICATIONS AND PAPERS PRESENTED

Journal Article

1. Asif Mustafa and Saad Mekhilef, *"Dual Phase LLC Resonant Converter with Variable Frequency Zero Circulating Current Phase-Shift Modulation for Wide Input Voltage Range Applications"*, IEEE Transactions on Power Electronics, **(Accepted; I.F. 6.373)**
2. Asif Mustafa and Saad Mekhilef, *"A Reconfigurable H6-type LLC Resonant Converter with Symmetrical Resonant Tanks for Wide Gain Range Applications"*, IEEE Transactions on Circuit and Systems II: Express Briefs, **(to be submitted)**
3. Asif Mustafa and Saad Mekhilef, *"A Minimum Switch Hybrid LLC Resonant Converter for Wide Output Voltage Range Applications"*, IEEE Journal of Selected and Emerging Topics in Industrial Electronics, **(to be submitted)**